BOSTON UNIVERSITY

COLLEGE OF ENGINEERING

Dissertation

FABRICATION AND CHARACTERIZATION OF SEMICONDUCTOR CORE OPTICAL FIBERS FOR MID-INFRARED TRANSMISSION

by

MUSTAFA ORDU

B.S., Istanbul Technical University, 2011
M.S., Tohoku University, 2013

Submitted in partial fulfillment of the

requirements for the degree of

Doctor of Philosophy

2017

© 2017 by
MUSTAFA ORDU
All rights reserved

Approved by

First Reader

Soumendra N. Basu, PhD
Professor of Mechanical Engineering
Professor of Materials Science and Engineering

Second Reader

Siddharth Ramachandran, PhD
Professor of Electrical and Computer Engineering
Professor of Materials Science and Engineering

Third Reader

Shyamsunder Erramilli, PhD
Professor of Physics
Professor in Biomedical Engineering

Fourth Reader

Srikanth Gopalan, PhD
Associate Professor of Mechanical Engineering
Associate Professor of Materials Science and Engineering

Turk lords, nation, hear! Bilge Kagan

Acknowledgments

I would like to express my sincere gratitude to my advisor Professor Soumendra Nath Basu for giving me the opportunity to become a novice in his group. His guidance and intellectual support during my study in Boston University was the privilege to me. Many times he sit down with me and taught how to approach scientific problems and find the best solutions. He calmed me whenever I was frustrated and he supported me all the way to the end. I can not express my respect to him.

I would like to thank Prof Siddharth Ramachandran for his guidance on the project through and even after the project. He taught me the importance of the photonics to the science, and always the useful criticism to my study. His unique research topics have widened my knowledge. I would also like to thank Prof Shyamsunder Erramilli for his help and mentorship on the project. His informal lectures on photonics, quantum science and even on life thought me a lot.I would like to acknowledge Prof Srikanth Gopalan as for being a part of my dissertation committee. I would like to thank Prof James Bird for his help on the initial part of the research and infrared imaging.

I would like to thank my collegue Jicheng Guo as being a good partner in the project. I would like to thank my collegue in Ramachandran's Group, Boyin Tai. Their help to shape this project is important. I would like to acknowledge the lab members of Basu's Group: Zhihao, Yanchen and Yashanshu, Ramachandran's Group: Dr. Patrick Gregg, Dr. Lu, Dr Demas, Dr Lars, Gautam Prambakar and Erramilli's group: Greg and Parth. I would like to thank my colleagues Farrukh Mateen, Ahmet Akosman, Vural Kara, Deniz Cetin, Habibe Durmaz and Ahmet Serdar Yilmaz for their help and encouragement along the PhD. I will always have good memories of our time in Boston University.

Most importantly, I would like to thank my dear parents Abdullah and Ayse for

being my idols and the continuous support throughout my life. I would like to thank my dear sister, Beyza for always being with me. You were always on the other side of the phone and the world being ready to support me. Whatever I have achieved so far is the reflection of them. Thank you for everything.

FABRICATION AND CHARACTERIZATION OF SEMICONDUCTOR CORE OPTICAL FIBERS FOR MID-INFRARED TRANSMISSION

MUSTAFA ORDU

Boston University, College of Engineering, 2017

Major Professor: Soumendra N. Basu, PhD
Professor of Mechanical Engineering
Professor of Materials Science and Engineering

ABSTRACT

Transmission in the mid-infrared (2-15 μm) spectrum has many applications, including biomedical surgery, chemical detection, and countermeasures in defense systems, among others. This highlights the necessity of a suitable fiber for the mid-infrared (mid-IR) spectral range. Although fluoride and chalcogenide glasses have shown promise of relatively low transmission losses, they are prone to devitrificaion at room temperature leading to performance degradation. Semiconductors, such as germanium and silicon have low theoretical losses in the mid-IR spectral range, and are stable at room temperature, making semiconductor-core fibers worthy of exploration for mid-IR transmission.

In this study, germanium-core, borosilicate glass-cladded, silicon-core silica-cladded and silicon-germanium-core silica-cladded fibers were drawn in laboratory-made mini draw towers and rod in tube method at a relatively low temperature of 1000°C for borosilicate glass drawing and 1760°C for silica drawing. 3 mm outer diameter core drilled germanium rods were placed in borosilicate glass tubes as preforms of ger-

manium fibers, 3 mm outer diameter core drilled silicon rods were placed in silica tubes as preforms of silicon fibers, and 1.9 mm outer diameter core drilled germanium rods and 2 mm inner diameter, 3 mm outer diameter core drilled silicon tubes were placed concentrically in silica tubes as preforms of silicon-germanium alloy fibers. The core/cladding area ratio was controlled by adding concentric borosilicate/silica tubes to increase the preform diameter. Depending on the drawing speed and initial core/cladding diameter ratio, fibers with core diameters of 10-200 μm with cladding diameters of 130-500 μm, as well as canes with core diameters of 300-350 μm and cladding diameters of 1.3-1.4 mm were drawn.

The drawn fibers were characterization by scanning/transmission electron microscopy (S/TEM), energy dispersive x-ray spectroscopy (EDX), x-ray diffraction (XRD) and electron backscatter diffraction (EBSD). It was found that there was minimal diffusion of oxygen and silicon from the cladding to the core in the Ge-core fibers. In the Si-core and Si-Ge alloy-core fibers, around 3 at % oxygen were found in the core, presumably due to enhanced diffusion at the higher drawing temperature of the silica-clad fibers. Optical characterization of the Ge canes, carried out using Fourier transform infrared spectroscopy (FTIR) in the 1.3-16 μm wavelength range, showed similar transmission characteristics, albeit with increased losses, over the entire wavelength range as the core drilled unprocessed germanium rod, even though the germanium core had undergone melting and re-solidification during the fabrication process. The transmission losses in the fibers were measured using two quantum cascade lasers, and were found to average 5.1 dB/cm for Ge-core fibers and 12 dB/cm for Si-core fibers in the 5.75-6.30 μm range. Transmission loss of Si-Ge alloy fibers was found to be 28 dB/cm at 6.1 μm. The higher losses of Si-Ge fibers can be attributed to compositional fluctuation in the core, due to the rapid cooling rate during fiber drawing. High temperature annealing of the fibers following by slow

cooling homogenized the fiber core, but also introduced cracks, which did not reduce the transmission losses. Non-linear properties of Ge-core fibers and canes were investigated using femtosecond pump-probe spectroscopy. Unprocessed 3 mm diameter rods exhibited the same detuning oscillations as 770 and 358 μm Ge-core canes and a 132 μm Ge-core fiber, indicating that the non-liner properties of the semiconductor cores were preserved during processing.

Contents

1 Introduction **1**

1.1 Fibers for Optical Communication 1

1.2 Mid-Infrared Technology 3

1.3 Fiber Transmission 4

1.4 Fiber Loss Mechanisms 7

1.4.1 Intrinsic Losses 7

1.4.2 Extrinsic Losses 8

1.5 Mid-IR Fibers 9

1.5.1 Heavy Metal Oxides 9

1.5.2 Halide Crystals 10

1.5.3 Fluoride Glasses 10

1.5.4 Chalcogenide Glasses 11

1.5.5 Semiconductor Fibers 12

1.5.6 Nonlinear Properties of Semiconductor Fibers 15

1.6 Objective 15

2 Experimental Details **17**

2.1 Fiber Fabrication 17

2.1.1 Preform Preparation for Ge Fibers 17

2.1.2 Preform Preparation for Si Fibers 18

2.1.3 Preform Preparation for SiGe Fibers 19

2.1.4 Fiber Drawing 19

2.1.5 Polishing . . . 22
2.2 Fiber Characterization . . . 23
2.2.1 Transmission Electron Microscopy . . . 23
2.2.2 X-ray Diffraction Spectroscopy . . . 25
2.2.3 Electron Backscatter Diffraction Spectroscopy . . . 27
2.2.4 Fourier Transform Infrared Spectroscopy . . . 27
2.2.5 Quantum Cascade Laser . . . 28
2.2.6 Femtosecond Mid-IR Pump-probe Spectroscopy . . . 31

3 Germanium Fibers **35**
3.1 Simulation of Neck Formation and Core Melting . . . 35
3.2 Fiber Drawing . . . 39
3.3 TEM Results . . . 39
3.4 XRD Results . . . 40
3.5 EBSD Results . . . 42
3.6 FTIR Results . . . 42
3.7 QCL Results . . . 44
3.8 Significance of Results . . . 48

4 Silicon Fibers **50**
4.1 Simulation of Core Melting and Neck Formation . . . 50
4.2 Fiber Drawing . . . 51
4.3 EDX Results . . . 52
4.4 XRD Results . . . 54
4.5 Transmission Loss Measurements . . . 55

5 Silicon-Germanium Alloy Fibers **58**
5.1 Graded-Index Fibers . . . 58
5.2 Fiber Drawing . . . 59

5.3 EDX Results 59
5.4 Transmission Loss Measurement 60
5.4.1 Non-equilibrium Solidification 61
5.5 Post-drawing Fiber Annealing 62
5.5.1 Annealing with Rapid Cooling Rates 64
5.5.2 Annealing with Slow Cooling Rates 65
5.5.3 Annealing with Multi-step Cooling Rates 69
5.5.4 Physical Limitations for GRIN Fiber Drawing 69
5.5.5 Transmission Loss Measurement of the Homogeneous SiGe Fiber 70
5.5.6 Devitrification of Silica 71
5.6 Comparison of the Losses 71
5.7 Discussion on the Cladding Material 73

6 Femtosecond Mid-IR Pump-Probe Spectroscopy on Semiconductor Fibers 76

6.1 Detunning Oscillation 76
6.2 SEM-EDX Results 81
6.3 XRD Results 81
6.4 Pump-Probe Spectroscopy on Ge samples 83

7 Conclusions 89

A Identifying the Source of Losses 92

References 95

Curriculum Vitae 101

List of Tables

2.1 Chemical composition of borosilicate glass tubes that were used in fiber drawing [Schott, 2014]. 18

5.1 Heating recipe 1 for annealing with rapid cooling rate. 65

5.2 Heating recipe 2 for annealing with rapid cooling rate. 65

5.3 Heating recipe for annealing with slow cooling rate. 67

5.4 Heating recipe for annealing with multi-step cooling rates. 69

5.5 Comparison of the Losses. 72

List of Figures

1·1 Mesured transmission of silica fibers and theoretical limitations [Teich and Saleh, 1991] 2

1·2 Absorption spectra of various gases in the mid-infrared region [Willer et al., 2006] 4

1·3 Schematic representation of an optical fiber. 5

1·4 3D structure of a typical optical fiber with core, cladding and buffer. Buffer layer protects the core and cladding from physical damages. Radius of core is represented with 'a' 6

1·5 Losses of various materials in near-IR mid-IR regions [Harrington, 2004]. 9

1·6 Fluoride and chalcogenide based fibers [Bei et al., 2013]. Cross-sections of (a)fluoro-indate fiber, and (b) single mode chalcogenide fiber [Mossadegh et al., 1998]. 11

1·7 (a) Germanium-core borosilicate glass-cladded fiber by rod-in-tube method [Ballato et al., 2009], (b) Silicon-core silica-cladded fiber by HP-CVD [Lagonigro et al., 2010]. Scale bar is 40 μm 12

1·8 Transmission losses of various reported semiconductor-core glass-cladded fibers with the lengths and core diameters of the measured fibers. Each color represents the research group/collaboration where the fibers were fabricated and were measured. Dark green symbols are for the collaboration between Pennsylvania State University and Optoelectronics Research Center at University of Southampton [Lagonigro et al., 2010, Mehta et al., 2010b, Sparks et al., 2011]. Light green symbols are for Pennsylvania State University [Ji et al., 2017, Ji et al., 2016]. Magenta symbols are for Clemson University [Ballato et al., 2008, Ballato et al., 2011]. Blue triangle symbol is for Norwegian University of Science and Technology [Nordstrand et al., 2013]. Blue Diamond symbol is the collaboration between various universities and institutions led by Norwegian University of Science and Technology (Full list can be found in the paper [Coucheron et al., 2016]). Red square symbol is for Boston University [Ordu et al., 2017]. Dashed red rectangle shows the range of the measurement where as the solid red square shows the center wavelength. The transmission windows of the bulk Si, Ge and ZnSe are shown as dashed rectangles on the lower part of the figure. . 14

2·1 Schematic of a preform. The semiconductor rod is placed in the glass tube and is sealed with glass rods. 18

2·2 Laboratory fabricated mini draw towers for (a) Ge-core borosilicate glass-clad fibers (b) Si-core and SiGe-core silica-clad fibers. 20

2·3 FEI Quanta 3D FEG transmission electron microscope. 24

2·4 a) Schematic image of TEM sample preparation. b) The TEM sample produced by FIB-based lift-off technique. 24

2·5 Bruker D8 Discover x-ray diffraction system with 2D detector. 25

2·6 Schematic representation of XRD and 2D detector. Constructively interfered x-rays reflect from the sample and are collected by 2D detector. 26
2·7 Photograph of the FTIR setup, with a bench type Bruker Vertex 70v on the left and a Bruker Hyperion microscope on the right. 28
2·8 QCL output power versus current. 29
2·9 Schematic representation of QCL experimental setup. 30
2·10 Schematic representation of QCL experimental setup for imaging. . . 31
2·11 2D Schematic representation of Pump-Probe experimental setup. IR beam from DFG is split into pump and probe beam by a BaF_2 wedge. Two beams hit on the same spot of the sample by using parabolic mirror. At the output end, another parabolic mirror collects the pump and probe lights. Pump light is blocked whereas probe light is collected by the monochromator. 33
2·12 3D Schematic representation of Pump-Probe experimental setup. . . . 34

3·1 Schematic of furnace setup in simulation. Furnace has Gaussian temperature profile. 36
3·2 Simulation results. (a) Before deformation, (b) the beginning of deformation and (c) neck formation. Colors from blue to red represents the coefficient of viscosity where red is the highest and blue is the lowest. 38
3·3 Optical micrograph of a polished cross-section of a Ge-core fiber. . . . 39
3·4 (a) TEM bright-field micrograph of the fiber cross-section at the core/cladding interface. (b) Ge, (c) O, and (d) Si EDX dot-maps. (e) EDX line scans across the core/cladding interface of the fiber showing the composition profile of Si, Ge, O, B, K, N and Al. Diffusion of oxygen from the cladding to the core is minimal. 40

3·5 HRTEM micrograph of core-cladding interface of the Ge-core fiber, showing the single crystalline nature of the core. 41
3·6 Reciprocal space mapping of the Ge core with 1 mm x-ray beam and a 2-D detector, showing a single (111) peak 41
3·7 EBSD of Ge fiber. (a) SEM micrograph of fiber polished along length to expose the core. (b) Orientation map of grains obtained by EBSD. (c) Orientation key used for map. 42
3·8 Results of wavelength dependent optical transmission characterization using FTIR spectroscopy. (a) Transmission spectra of glass rod and hardened epoxy (b) Transmission spectrum of germanium rod. 44
3·9 Comparsion of an unprocessed Ge rod and a drawn Ge-core cane in FTIR. 45
3·10 Vertical and Horizontal scans of fiber with QCL. 45
3·11 Transmission characteristics in the QCL range of Ge fibers of three different lengths of 8.63 mm, 8.25 mm, and 7.91 mm, as well as the laser output signal with no sample in the path of the QCL. The sharp dips are due to atmospheric absorption peaks. 46
3·12 Best fit of a 4^{th} order polynomial to the transmission spectrum of the 8.63 mm fiber, using a reduced dataset of points away from the atmospheric absorption peaks. 47
3·13 Transmission losses of Ge-core fiber. 47

4·2 (a)SEM micrograph of the fiber. Elemental dot maps of (b) Si and (c) O. 52
4·1 SEM micrograph of Si-core silica-cladded fiber in cross-section. 52

4·3 EDX line scan across the fiber core and cladding identifies the composition profile of Si and O. The oxygen content of the core due to diffusion from the cladding is ∼3at%. 53
4·4 $\theta/2\theta$ XRD scan of a Si-core fiber with 1-D detector showing that the fiber core is polycrystalline. 54
4·5 Un-normalized output intensity from a Si fiber polished down to different lengths. 55
4·6 4th order polynomial fits on the data points away from the absorption peaks. 56
4·7 Transmission losses of the Si-core fiber. Average loss is 12.45 dB/cm. 57

5·1 Refractive index profile of (a) a step-index fiber and (b) a graded-index fibers with respect to fiber cross-section. 58
5·2 SEM image of SiGe alloy-core fiber. Brighter parts of the image are Ge-rich, darker parts are Si-rich regions. 60
5·3 (a) SEM micrograph of the core region. EDX elemental dot mapping of fiber elements; (b) O, (c) Ge and (d) Si. 61
5·4 Un-normalized output intensity of SiGe alloy-core fiber with 4.78 mm length. 62
5·5 Non-equilibrium solidification of Cu-Ni alloy [Askeland and Phulé, 2006]. 63
5·6 Annealed fiber with heating recipe 1 for annealing with rapid cooling rate. Random segregation can be seen across the core region. 66
5·7 Annealed fiber with heating recipe 2 for annealing with rapid cooling rate. Improvement on the elemental distribution is apparent. 66
5·8 Scanning electron micrograph of the fiber cross-section annealed with slow cooling rate. 67

5·9 (a) SEM Image of the annealed fiber core and SEM-EDX elemental dot maps of (b) O, (c) Ge and (d) Si. Improved elemental distribution can be seen. 68

5·10 (a) Electron micrograph of the fiber core annealed with multi-step cooling rates. Elemental dot mapping of (b) O, (c) Ge and (d) Si show the homogeneity of the alloy-core. 70

5·11 Cracks on the glass cladding of the annealed fiber. Devitrification has detrimental effect to the fiber. 72

5·12 Viscosity of three different glasses. Softening line shows the softening point of glasses ($10^{6.6}$Pa.s). Viscosity of working range differs between $10^4 - 10^{5.5}$Pa.s. 75

6·1 Time delay between the pump and the probe pulses. 77

6·2 Optical micrograph of a finely polished Ge-fiber that is used for Pump-Probe Spectroscopy measurement. 82

6·3 (a) Electron micrograph of the Ge-core fibers that was used for the Pump-Probe spectroscopy. EDX Elemental dot mapping of fiber (b) Ge, (c) Si and (d) is O. (e) show EDX line scan through the fiber cross-section that are show in the inset. 82

6·4 2D scan of Ge-core fiber. Fiber has the (220) single crystal orientation. 83

6·5 Simulation of detunning oscillation. 84

6·6 Experimental results on four different samples: unprocessed Ge rod with 3 mm diameter, Ge cane with 770 μm-core diameter, Ge cane with 358 μm-core diameter and Ge fiber with 132 μm-core diameter. (a), (b), (c) and (d) are contour plots of samples with respect to delay time (ps) and wavenumber (cm^{-1}). Each figures are individual from each other but have the same color code. Red indicates maximum normalized intensity whereas blue represents minimum normalized intensity. 85

6·7 Population decay of each sample with respect to delay time and optical delay difference at 2214 cm^{-1}. 86

6·8 Oscillation period of four different samples at selected detuning frequencies. 87

A·1 Calculated coupling efficiency for the first 25 0m modes versus distance from the focal plane of the input lens of the QCL at 1640 $cm^{-}1$. . . . 94

List of Abbreviations

CTE	.....	Coefficient of Thermal Expansion
DFG	.....	Difference Frequency Generator
EDX	.....	Energy Dispersive X-ray spectroscopy
FIB	.....	Focusing Ion Beam
FTIR	.....	Fourier Transform Infrared Spectroscopy
FWHM	.....	Full Width at Half-Maximum
HMO	.....	Heavy Metal Oxides
HP-CVD	.....	High Pressure-Chemical Vapor Deposition
HRTEM	.....	High Resolution Transmission Electron Microscopy
IR	.....	Infrared
MBE	.....	Molecular Beam Epitaxy
MCT	.....	Mercury Cadmium Telluride
MOCVD	.....	Metal-Organic Chemical Vapor Deposition
NA	.....	Numerical Aperture
ND	.....	Neutral Density
OPA	.....	Optical Parametric Amplifier
QCL	.....	Quantum Cascade Laser
RWA	.....	Rotating Wave Approximation
RSM	.....	Reciprocal Space Mapping
SOI	.....	Silicon-on-Insulator
S/TEM	.....	Scanning/Transmission Electron Microscopy
TIR	.....	Total Internal Reflection
UV	.....	Ultra Violet
XRD	.....	X-ray Diffraction Spectroscopy

Chapter 1

Introduction

1.1 Fibers for Optical Communication

The use of light to transmit data gained widespread acceptance in the 1970s, with the invention of the continuous operating GaAs laser at the room temperature as the source and germanium doped silica fibers as the delivery medium [Hayashi et al., 1970, Kapron et al., 1970, Teich and Saleh, 1991]. These inventions allowed optical fibers to become the major player in the communication field.

Today, reliable, low-loss optical fibers are ubiquitous, with commercially available silica-based fibers exhibiting transmission losses as low as 0.2 dB/km at 1.55 μm [Miya et al., 1979]. Figure 1·1 shows the loss characteristic of silica fibers in the region of 0.6-1.8 μm. At wavelengths below 1.65 μm, transmission is limited by Rayleigh scattering, with losses increasing with the decreasing wavelengths. At wavelengths above 1.65 μm, transmission is limited by infrared absorption, with losses increasing with increasing wavelengths.

Although silica fibers are the best solution for communication using the 1.3 μm and 1.5 μm transmission windows due to their low loss values, their applicability in the infrared spectrum is severely limited due to the rapid increase in infrared adsorption losses at wavelengths above 1.65 μm.

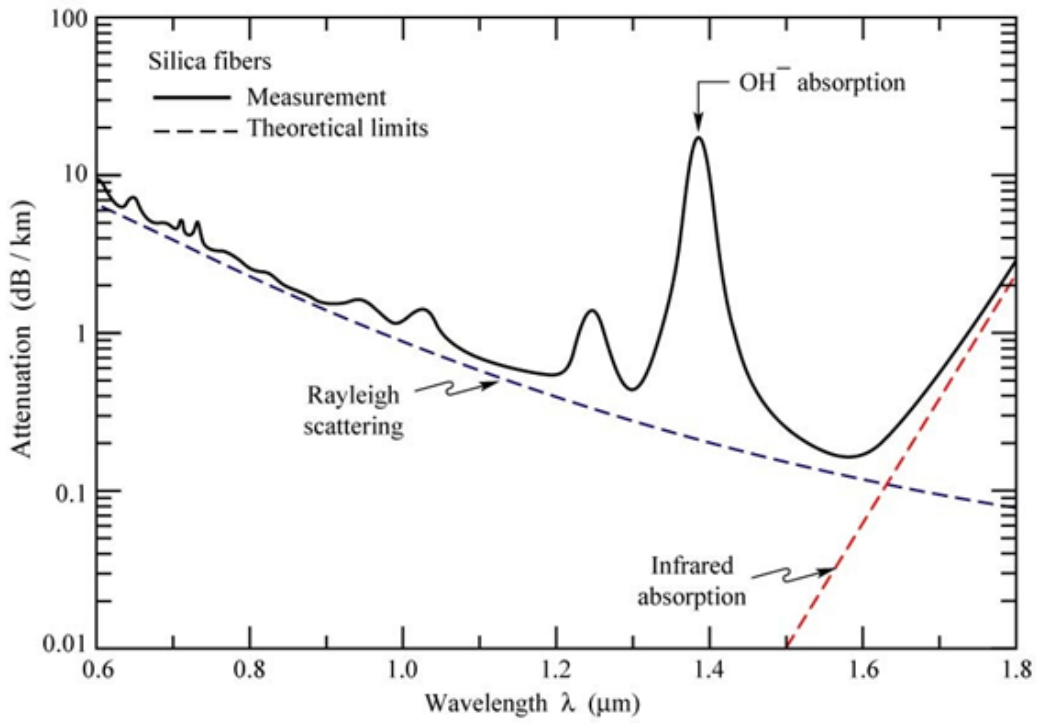

Figure 1·1: Mesured transmission of silica fibers and theoretical limitations [Teich and Saleh, 1991]

1.2 Mid-Infrared Technology

Infrared (IR) wavelengths start after the visible red (700 nm) and end at 1 mm where the microwave region begins. The IR spectrum is further subdivided into wavelength groups, which surprisingly differ for different application areas. For optical fibers, the IR region can be divided into three categories:

- Near-infrared (near-IR): 0.7-2 μm
- Mid-infrared (mid-IR): 2-15 μm
- Far-infrared (far-IR): 15-1000 μm

On this scale, silica fibers cover most of near-IR region as a low loss material. However, due to high losses in the mid-IR region, alternate fiber materials are needed.

There has been increasing interest in transmitting in the mid-IR region for many potential applications. For instance, the absorption spectrum of a variety gases lie in mid-IR region (Fig. 1·2). Mid-IR fibers can be used for detection of environmentally hazardous greenhouse gases and bio-terror agents [Willer et al., 2006]. Some mid-IR fibers are already being developed for this purpose [Sanghera et al., 2000].

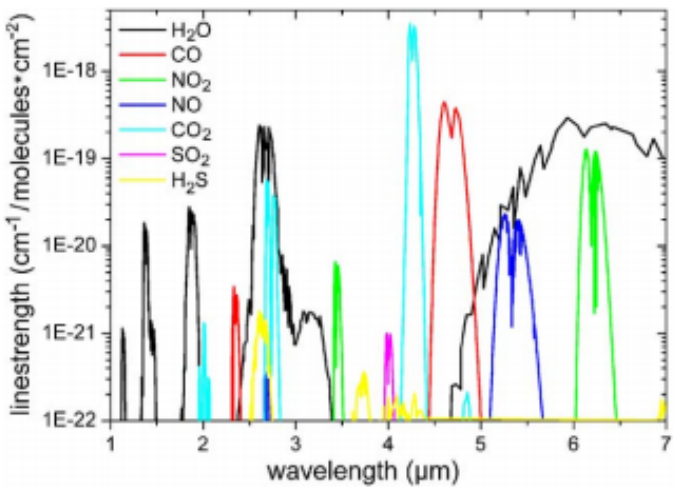

Figure 1·2: Absorption spectra of various gases in the mid-infrared region [Willer et al., 2006]

In biomedical surgery, use of mid-IR lasers cause minimal thermal damage to tissue and muscle contraction [Lin, 2001]. Moreover, by improving mid-IR fibers, it will be possible to remotely deliver light from a laser room to multiple surgical locations. In defense technologies, mid-IR fibers can be used in countermeasure applications such as detecting and avoiding heat seeking missiles [Fetterly, 2008].

1.3 Fiber Transmission

Optical fibers have of two main parts: core and cladding. The core is the inner part of fiber where light is confined. The cladding is the outer part that surrounds the core, creating a refractive index difference. Light confinement in the core occurs by total internal reflection (TIR), which occurs only when the refractive index of core, n_1, is greater than the refractive index of cladding, n_0, and the light strikes the interface between core and cladding at an angle greater than the critical angle with respect to the interface normal. The critical angle, θ_c, can be expressed as

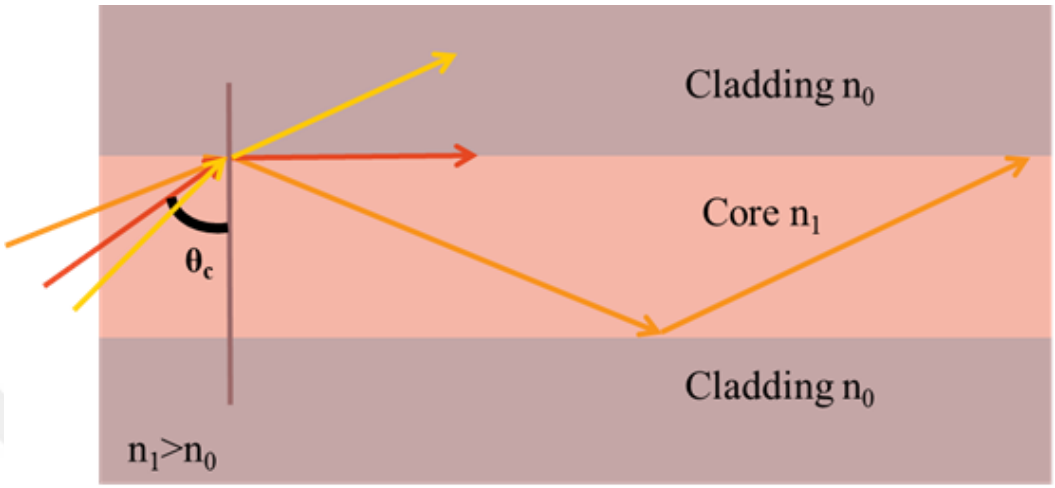

Figure 1·3: Schematic representation of an optical fiber.

$$sin(\theta_c) = \frac{n_0}{n_1} \tag{1.1}$$

Figure 1·3 shows a schematic representation of the basic fiber structure. If a ray of light strikes the interface with an angle smaller than the critical angle (yellow arrows), refraction occurs. The input light loses a portion of its power at each reflection and eventually vanishes. When the light strikes the interface at the critical angle (red arrows) it theoretically travels through the core/cladding interface. If it strikes with an angle larger than the critical angle (orange arrows) the light is reflected back (TIR) and is confined in the core.

There are some important parameters that define the characteristics of optical fibers. The numerical aperture (NA) is one of the most important fiber parameters that is related to the critical angle. NA describes the range of angles within which light that is incident on the fiber will be transmitted along it, and is defined as

$$NA = \sqrt{n_1^2 - n_0^2} \tag{1.2}$$

The V number is an important parameter that defines the guiding properties of

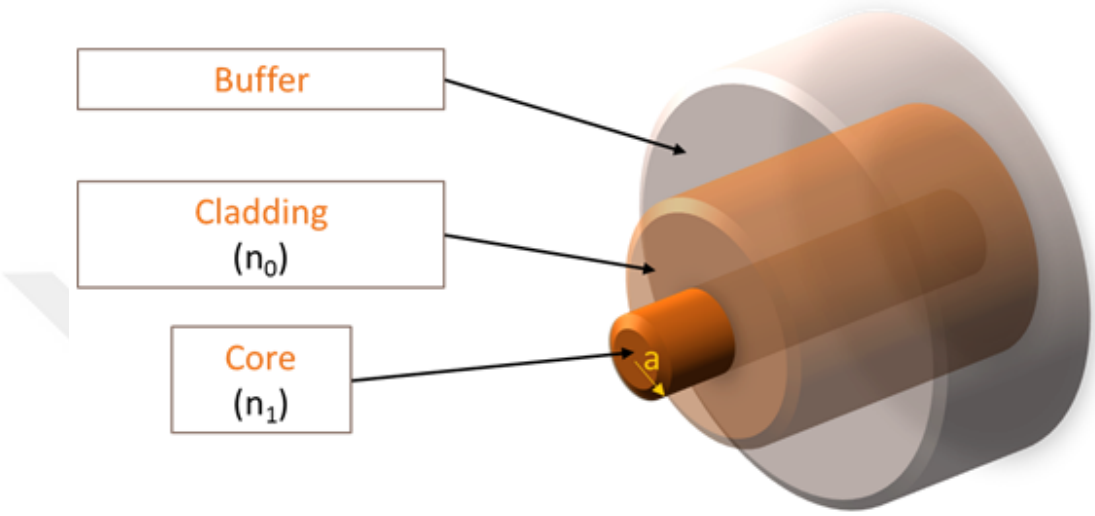

Figure 1·4: 3D structure of a typical optical fiber with core, cladding and buffer. Buffer layer protects the core and cladding from physical damages. Radius of core is represented with 'a'

the fiber. In the ray-optic approach, light is expressed as 2D ray and is limited by NA and TIR. In a more realistic case, light propagates as a wave rather than as a ray. This approach naturally opens up the concept of the modes of a fiber. The modal characteristic of a fiber can be calculated with its V number, and is given as:

$$V = \frac{2\pi}{\lambda} a \sqrt{n_1^2 - n_0^2} \tag{1.3}$$

where λ is the wavelength of light, and a is the fiber radius (Fig. 1·4). The V number defines the number of modes that can propagate through a certain fiber. For instance, single mode fibers that only guide the lowest order mode (fundamental mode) have V numbers less than or equal to 2.405. The number of modes, M, is related to the V number as

$$M \approx \frac{4V^2}{\pi^2} \tag{1.4}$$

1.4 Fiber Loss Mechanisms

Attenuation or transmission loss of optical fibers is one of its most important parameters. The losses in optical fibers is characterized by its absorption coefficient, α, in the logarithmic unit of decibel, given as:

$$\alpha = -\frac{10}{L} log_{10}\Big(\frac{P_0}{P_i}\Big) \tag{1.5}$$

where L is the fiber length, P_i is the input power, P_o is the output power. The unit of α is dB/length, where the length can be expressed in terms of km, m, or cm. The fiber losses can be divided into two parts; intrinsic and extrinsic, giving:

$$\alpha = \alpha_{int} + \alpha_{ext} \tag{1.6}$$

Intrinsic losses are related to inherent material absorption and these losses cannot be lowered below the fundamental materials values. On the other hand, extrinsic losses are attributable to impurities and defects, and can be lowered by improved fiber processing and design.

1.4.1 Intrinsic Losses

There are three major types of intrinsic loss mechanisms; ultraviolet (UV) absorption, Rayleigh and Brillouin scattering, and multi-phonon absorption. These losses can be expressed as:

$$\alpha_{int} = Ae^{a/\lambda} + B\lambda^{-4} + Ce^{-c/\lambda} \tag{1.7}$$

The first term on the right represents the losses related to UV absorption that occurs in the short wavelength region. For IR fibers, this type of loss approaches

zero in the infrared region. The second term on the right describes scattering losses due to Rayleigh (elastic) scattering that dominates in glassy materials and Brillouin (inelastic) scattering that dominates in crystalline materials. In glassy materials, the density or compositional fluctuations causes non-uniform refractive index through the medium that results in Rayleigh losses. In contrast, the ordered structures of crystalline materials do not cause any Rayleigh scattering. This results in very low losses in single crystal materials. The third term on the right represents infrared absorption or multi-phonon absorption losses. In this loss mechanism, light is coupled to lattice vibrations (phonons) and transformed to thermal energy.

1.4.2 Extrinsic Losses

Extrinsic losses are due to the imperfections in the material. They occur as a result of impurities and extrinsic scattering. Although these losses can be eliminated in principle, in practice it is almost impossible to do so. In many cases, extrinsic losses can be the dominant loss mechanism in IR fibers. Impurities such as water (OH^-, H_2O), transition metals (Cu, Fe, Ni), and oxygen can strongly absorb light at different wavelengths. Moreover, material defects such as dislocations, vacancies, interstitials, grain boundaries, interfacial cracks due to core/cladding coefficient of thermal expansion (CTE) mismatches, bubbles, etc. can all contribute to extrinsic losses.

For a given absorption coefficient, α, the transmission loss factor, $\mathcal{L}$, can be defined as

$$\mathcal{L} = exp(-\alpha L) \tag{1.8}$$

where L is the length of the fiber. Extrinsic losses increase exponentially with the length of the fiber.

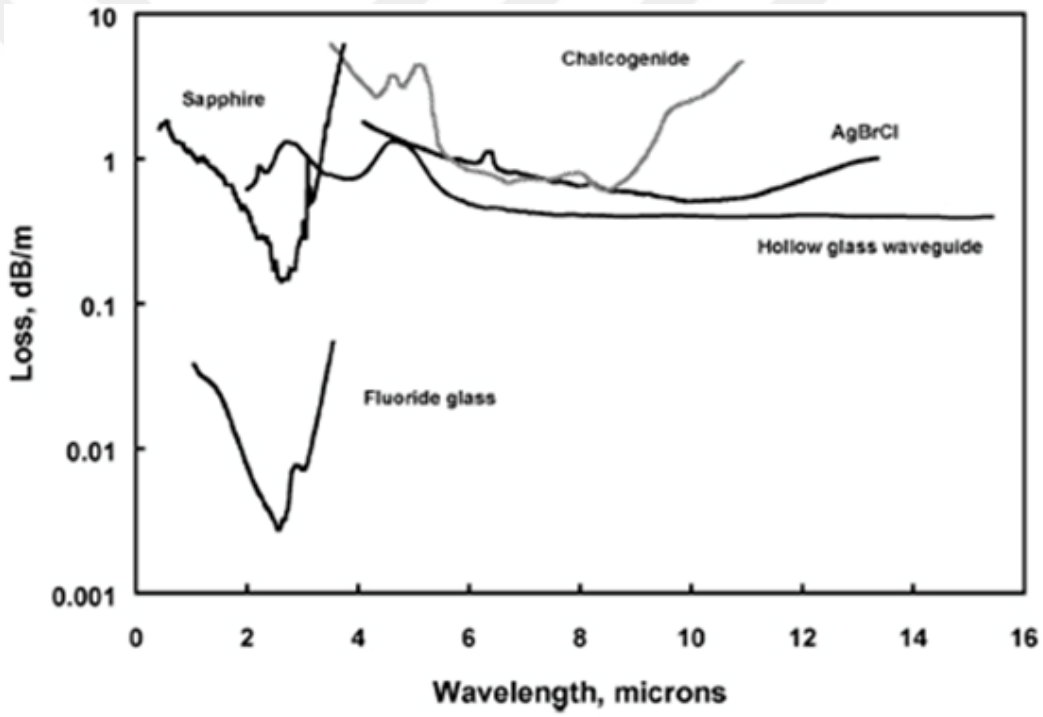

Figure 1·5: Losses of various materials in near-IR mid-IR regions [Harrington, 2004].

1.5 Mid-IR Fibers

Due to the poor performance of silica fibers in mid-IR region, several alternative materials systems have been explored [Tao et al., 2015]. Figure 1·5 shows the wavelength dependent loss of some of these materials. These materials systems are described in more detail below.

1.5.1 Heavy Metal Oxides

As an alternative materials system, heavy metal oxides (HMO) are based on $TeO_2 - PbCl_2$ and $TeO_2 - ZnO$ combinations [Lezal et al., 1998]. Sometimes they are doped with lanthanides such as Nd^{+3} and Er^{+3}. The solubility of lanthanides depends on the purity level of HMO. They mostly contain impurities and hydroxyls that are difficult to remove [Morgan et al., 1997, Hector et al., 1997]. HMOs have transmission spectrum in the range of 2-6 μm. These glasses contain scattering centers that are caused by hydroxyl groups and absorbing defects that are impurity related which limit HMOs from practical use.

1.5.2 Halide Crystals

Halide crystals have been explored as alternatives to glass fibers for infrared transmission. Unlike glasses that are vitreous (short range ordered materials with covalent bonds and no long range order), crystals have long-range order with ionic bonds. The crystals do not have a glass transition temperature above which the material becomes soft enough to be drawn. Thus, unlike glasses, crystalline materials cannot be drawn in their solid state. Alternative techniques such as high temperature extrusion is needed for solid state fabrication of halide crystals making them difficult to fabricate [Harrington, 2004].

The most promising crystalline halide fibers fabricated are composed of silver

halide (AgBrCl), which have 0.2 dB/m losses [Sa'Ar et al., 1987,Simhony et al., 1988]. These fibers are fabricated by applying high pressure to force the halide through a die at elevated temperatures that is below the melting temperature. Since silver halide is a very ductile material, fiber drawing has been successful, albeit challenging.

1.5.3 Fluoride Glasses

Fluoride glasses are another materials system explored for mid-IR transmission in of the 0.5-4 μm range. Their low refractive index values ($\sim$ 1.5) gives them an advantage compared to other mid-IR materials that usually have refractive indices of 2 and above. Fluoro-zirconates and fluoro-aluminates are the most popular fluoride glasses. One example of fluoride glasses is ZBLAN ($ZrF_4-BaF_2-LaF_3-AlF_3-NaF$) which has loss value of 0.45 dB/km at 2.35 μm [Szebesta et al., 1993], making ZBLAN as one of the lowest loss mid-IR fibers. Fluoro-zirconate glass fibers have been used for Er:YAG lasers for dentistry and ophthalmology [Romano et al., 1994,Bei et al., 2013]. Figure 1·6(a) shows a fluoro-indate fiber cross section. However, durability of fluoride glasses is much lower compared to silica fibers. Due to their low glass transition temperatures, fluoride glasses suffer from structural instabilities and performance degradation, even at the room temperature.

1.5.4 Chalcogenide Glasses

Chalcogenide glasses are normally composed of two or more chalcogens such as As, Ge, Sb, P, Te, Se and S [Harrington, 2004]. Mixture of chalcogens in an oxygen-free environment at elevated temperatures forms stable glasses such as As_2S_3, As_2Se_3, and $GeSe_2$. As_2S_3 was used in the first chalcogenide IR fibers in the 1960s by N.S. Kapany [Sing-Kapany, 1967]. After the breakthrough discovery, many different chalcogenide materials have been investigated for IR fibers [Sanghera and Aggarwal, 1999, Kanamori et al., 1984].

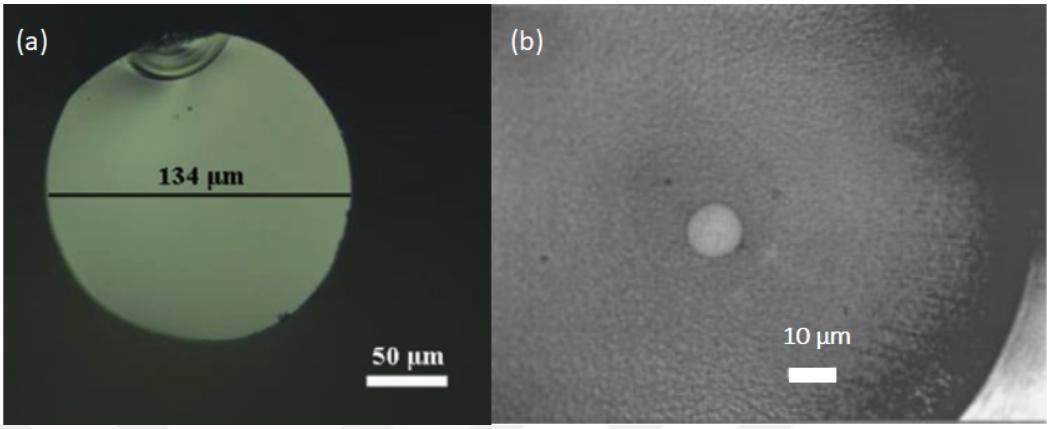

Figure 1·6: Fluoride and chalcogenide based fibers [Bei et al., 2013]. Cross-sections of (a)fluoro-indate fiber, and (b) single mode chalcogenide fiber [Mossadegh et al., 1998].

Chalcogenide fibers mainly fall under three categories: sulfide, selenide and telluride. Within these categories, the most suitable glasses for fiber fabrication are binary or ternary systems. Although chalcogenide fibers generally do not transmit visible wavelengths, Ge-S based binary glasses doped with phosphorus were found to transmit in the visible range. Loss values of chalcogenide fibers can be as low as 1 dB/m at 2.7 μm [Mossadegh et al., 1998]. Figure 1·6(b) shows a single mode chalcogenide fiber.

Today, although chalcogenide fibers are commercially available, they still suffer problems of brittleness, toxicity, and especially room temperature performance losses over time due to devitrification.

1.5.5 Semiconductor Fibers

In the last decade, semiconductors have emerged as alternative materials for mid-IR fiber cores. Due to their low theoretical losses, materials such as silicon, germanium and gallium arsenide are promising candidate materials for mid-IR delivery [Harrington, 2004]. Unlike glasses, these materials have crystalline structures and do not exhibit a glass transition temperature, making them mechanically and chemically

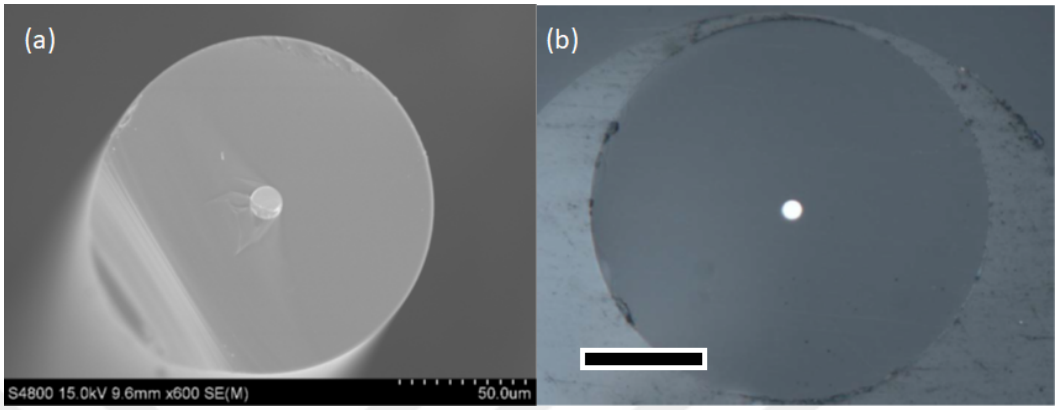

Figure 1·7: (a) Germanium-core borosilicate glass-cladded fiber by rod-in-tube method [Ballato et al., 2009], (b) Silicon-core silica-cladded fiber by HP-CVD [Lagonigro et al., 2010]. Scale bar is 40 μm
.

stable. There are two main techniques that have been utilized for successful fabrication of semiconductor-core fibers; rod-in-tube, [Ballato and Snitzer, 1995] and high-pressure chemical vapor deposition (HP-CVD) [Sazio et al., 2006]. A powder-in-tube method has also been explored, but significant oxidation of the semiconductor powders prevented light transmission [Scott et al., 2009].

Silicon-core silica cladded fibers have been fabricated by both rod-in-tube and HP-CVD techniques. Fibers fabricated by the rod-in-tube method exhibited a loss of 4.3 dB/m and fibers fabricated by the HP-CVD method exhibited a loss of 8 dB/cm [Ballato et al., 2008, Lagonigro et al., 2010]. Recently, laser crystallization was applied to Si-core fibers fabricated by the HP-CVD method in order to improve the crystallinity of te core (which is typically amorphous or fine grained after the HP-CVD deposition). This improvement in crystallinity (and increase in grain size) improved the transmission and the losses decreased to 1 dB/cm [Ji et al., 2016]. However, there is a limitation on the fiber length over which HP-CVD can be used to deposit a core.

Binary III-V compounds such as crystalline GaAs core fibers have also been fab-

ricated by the rod-in-tube method, although mid-IR transmission could not be measured in these fibers [Ballato et al., 2010]. Furthermore, germanium-core fibers with different glass claddings such as silica [Ballato et al., 2011,Mehta et al., 2010b,Ji et al., 2017] and borosilicate [Ballato et al., 2009] glasses have been fabricated. Borosilicate glass and germanium have a good CTE match and the working temperature of borosilicate glass is not significantly higher than the melting temperature of germanium, making this system ideal for drawing. However, previous efforts to draw germanium core borosilicate cladded fibers did not transmit mid-IR wavelengths. On the other hand, silica-cladded germanium-core fibers transmitted mid-IR wavelengths with losses between 0.7-10 dB/cm [Lagonigro et al., 2010,Ballato et al., 2011,Ji et al., 2017]. However, due to the CTE mismatch between the core and cladding, these fibers exhibited significant cracking. Figure 1·7 shows examples of silicon and germanium core fibers.

SiGe alloy-core fibers have great potential for infrared transmission due to their advantageous properties over elemental-core fibers. The refractive index of an alloy fiber can be tailored by changing the composition of the alloy, leading to tunable properties of fibers, such as the transmission window and bandgap [Coucheron et al., 2016]. Also, by controlling the solidification during the drawing or post-annealing process, it may be possible to form graded-index structures in semiconductor alloy cores. Graded-index structures have been shown to improve the transmission properties of silica-based fibers [Teich and Saleh, 1991]. Recent efforts have focused on creating SiGe alloy fiber cores of with different compositions [Coucheron et al., 2016, Chaudhuri et al., 2017]. Post-drawing processes such as laser re-crystallization and annealing were applied to improve the compositional homogeneity and/or increase the grain size of the fiber cores. All these efforts are aimed creating homogeneous step index fibers.

Figure 1·8 summarizes the up-to-date transmission losses of semiconductor-core

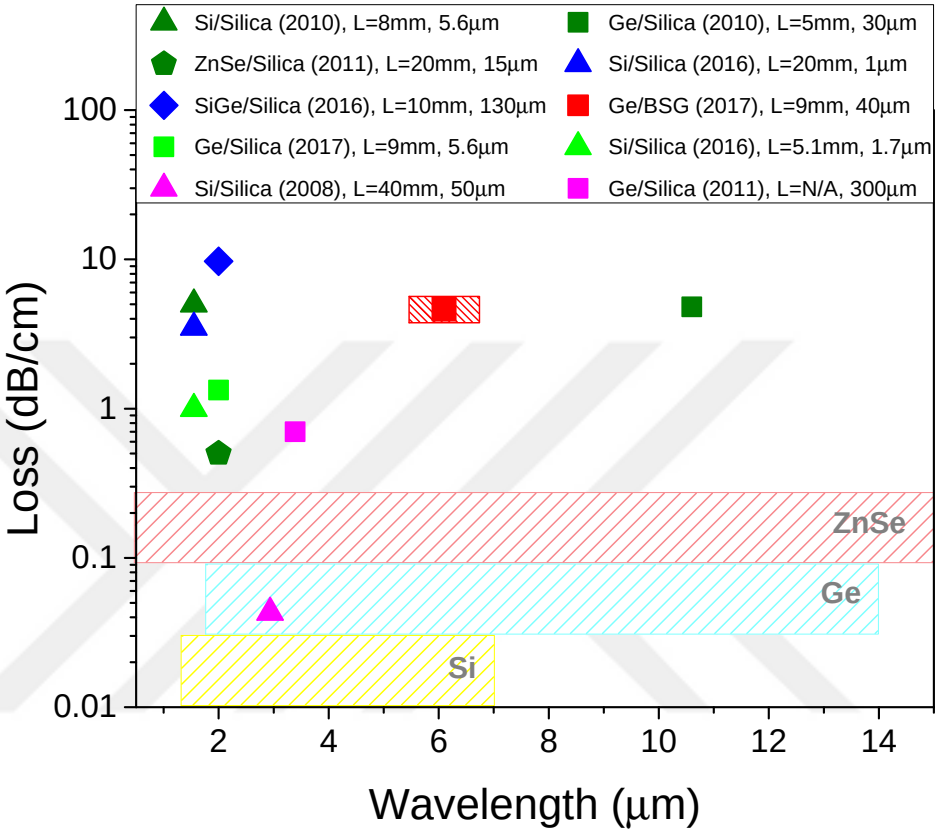

Figure 1·8: Transmission losses of various reported semiconductor-core glass-cladded fibers with the lengths and core diameters of the measured fibers. Each color represents the research group/collaboration where the fibers were fabricated and were measured. Dark green symbols are for the collaboration between Pennsylvania State University and Optoelectronics Research Center at University of Southampton [Lagonigro et al., 2010, Mehta et al., 2010b, Sparks et al., 2011]. Light green symbols are for Pennsylvania State University [Ji et al., 2017, Ji et al., 2016]. Magenta symbols are for Clemson University [Ballato et al., 2008, Ballato et al., 2011]. Blue triangle symbol is for Norwegian University of Science and Technology [Nordstrand et al., 2013]. Blue Diamond symbol is the collaboration between various universities and institutions led by Norwegian University of Science and Technology (Full list can be found in the paper [Coucheron et al., 2016]). Red square symbol is for Boston University [Ordu et al., 2017]. Dashed red rectangle shows the range of the measurement where as the solid red square shows the center wavelength. The transmission windows of the bulk Si, Ge and ZnSe are shown as dashed rectangles on the lower part of the figure.

glass-cladded fibers from different research groups and/or collaborations, based on an earlier review [Morris et al., 2012b]. The length of the fiber, the fiber core diameter, and the publication year of each study is noted in the plot below. The figure shows that to date, Si-core fibers have the lowest loss values among the semiconductor-core fibers.

1.5.6 Nonlinear Properties of Semiconductor Fibers

Semiconductors have promising nonlinear properties that can be exploited for possible applications [Mashanovich et al., 2017, Peacock and Healy, 2016]. Photolithographically processed semiconductor waveguides on single crystalline silicon-on-insulator (SOI) wafers, have shown different nonlinear properties. This suggests that nonlinear effects in semiconductor-core fibers can be similarly exploited. To date, nonlinear two-photon absorption and nonlinear refractive index were measured in silicon-core optical fibers. [Suhailin et al., 2016, Mehta et al., 2010a]. On the other hand, nonlinear properties of germanium were only investigated on waveguide structures [Zhang et al., 2014, Carletti et al., 2015] making nonlinear properties of the Ge-core fibers as an hereto unexplored realm of study.

1.6 Objective

As previously stated, materials such as halide crystals, heavy metal oxide glasses, fluoride glasses and chalcogenide glasses have been proposed as suitable materials for mid-IR transmission. Although some of these materials have low transmission losses in the targeted wavelength spectra, they have other material-related problems such as devitrification at room temperature, water absorption, difficulties in fabrication and mechanical instabilities. At this point, semiconductor-core based fibers are expected to overcome such problems due to their superior properties related to the issues mentioned. Moreover their transmission windows cover almost the entire mid-IR

spectrum, allowing for a wider range of applications.

In this study, the fabrication, and microstructural and optical characterization of germanium-core borosilicate glass-cladded optical fibers, silicon-core silica-cladded optical fibers and SiGe alloy-core silica-cladded fibers were carried out. Borosilicate glass was selected as cladding material of Ge-core fibers due to its better CTE match with Ge and its lower working temperature. Although borosilicate glass has also good CTE match with silicon, melting temperature of silicon is much higher than the working temperature range of borosilicate glass. Therefore silica was the choice of glass for silicon-core fibers. SiGe alloy-core fibers were also fabricated with silica due to the silicon content. The rod-in-tube method was utilized to draw all three types of the fibers in two different laboratory-made mini draw towers; lower temperature system for drawing fibers with borosilicate cladding and a higher temperature system drawing fibers with silica cladding.

The composition profiles of the fibers were characterized at nano-scale resolution using transmission electron microscopy and electron dispersive x-ray spectroscopy. The crystalline quality of the fibers was investigated by x-ray diffraction spectroscopy and electron backscatter diffraction spectroscopy. The wavelength-dependent optical transmission of the fibers was characterized using Fourier transform infrared spectroscopy and quantum cascade lasers. The transmission losses in the fibers were investigated. Post drawing heat treatments of SiGe fibers were explored to improve the core microstructure and lower transmission losses. Finally, nonlinear optical properties of the Ge-fibers were studied by femtosecond pump-probe spectroscopy.

Chapter 2

Experimental Details

2.1 Fiber Fabrication

As discussed in the previous section, germanium-core borosilicate-clad fibers, silicon-core silica-clad fibers and germanium-silicon-core silica-clad fibers were drawn using the rod-in-tube method [Wang et al., 1994, Ballato and Snitzer, 1995] in this study. This section describes the details of fiber fabrication, and is divided into three sections; preform preparation, fiber drawing and fiber polishing. The preform includes the semiconductor core as well as glass cladding used in the drawing step. The polishing of the ends of portions of the drawn fibers is needed to improve the facet quality for optical transmission measurements.

2.1.1 Preform Preparation for Ge Fibers

A preform is a combination of the core material in the form of a rod and the cladding material in the form of a tube, and is prepared prior to the drawing process. The core material in the preform was in the form of, 3 mm outer diameter (OD), 10 mm long germanium rods that were core-drilled from 99.999% pure single crystal n-type 10x10x50 mm^3 germanium blocks (Lattice Materials, Montana). The Ge rods were placed in a 3 mm inner diameter (ID) and 9 mm OD borosilicate glass tube (DURAN tubes, Schott AG, Germany). Additional borosilicate glass tubes were placed concentrically to increase outer cladding diameter up to 32 mm, depending on the desired core/cladding ratio.

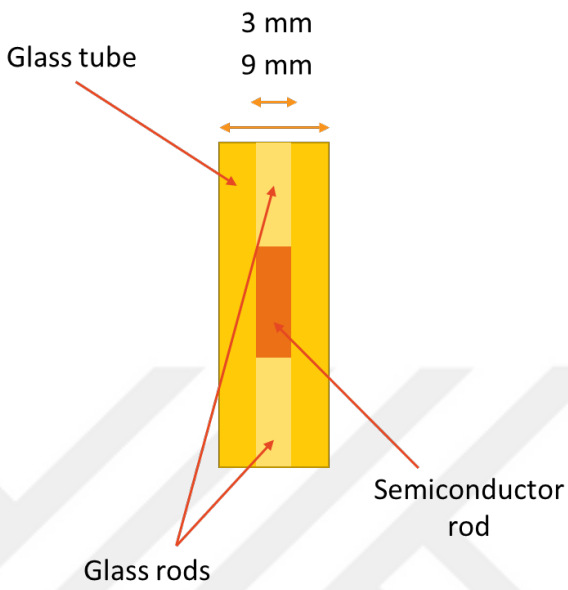

Figure 2·1: Schematic of a preform. The semiconductor rod is placed in the glass tube and is sealed with glass rods.

Table 2.1: Chemical composition of borosilicate glass tubes that were used in fiber drawing [Schott, 2014].

Component(s)	SiO_2	B_2O_3	$Na_2O + K_2O$	Al_2O_3
Weight%	81	13	4	2

Borosilicate glass is the choice of cladding due to its low working temperature where the germanium core is fully molten (melting temperature of germanium is 938°C). In order to prevent oxidation of Ge rod during the drawing, 3 mm OD borosilicate rods are placed above and below the Ge rod in the tube. Figure 2·1 shows the schematic representation of the preform. Although the borosilicate rods and the borosilicate tubes are represented by different shades of yellow in the figure, their compositions are identical. Table 2.1 shows the composition of the borosilicate glass.

2.1.2 Preform Preparation for Si Fibers

Similar to Ge fiber preforms, silicon rods with the same dimensions were core-drilled from 99.999% pure single crystal blocks of n-type silicon (Lattice Materials, Montana). The melting temperature of the Si (1414°C) is much higher than the working temperature range of the borosilicate glass, making borosilicate glass unsuitable as a cladding material for a Si core. Therefore silica was chosen as the cladding material. The Si rods were placed in a 3 mm ID 8 mm OD fused silica tubes (Technical Glass Product, Ohio). Additional silica tube was placed concentrically to increase the OD of cladding up to 15 mm. 3 mm OD silica rods with the same composition of the cladding tubes were used to prevent oxidation of the core.

2.1.3 Preform Preparation for SiGe Fibers

Since Si-Ge alloy fibers contain Si, borosilicate glass is not suitable as a cladding material and silica was used as the cladding glass. Si-Ge alloys for the cores were prepared in-house from pure Ge and Si blocks. The geometry of the core consisted of Ge rods inserted into one end closed Si tubes, to keep the molten Ge away from the glass cladding as long as possible. It is expected that on melting during fiber drawing, the alloy composition became homogeneous before the necking process began. 1.7 mm OD, 10 mm long Ge rods were core-drilled from the bulk Ge blocks. To make the Si tubes, 2 mm diameter holes were drilled to a depth of 9 mm into 10 mm thick Si blocks. 3 mm OD cores were then core drilled to a depth of 10 mm concentrically around the drilled holes to give Si tubes with a 0.5 mm cylindrical wall thickness and a 1 mm bottom base thickness. Oxidation was prevented by sealing the core with silica rods, as mentioned previously.

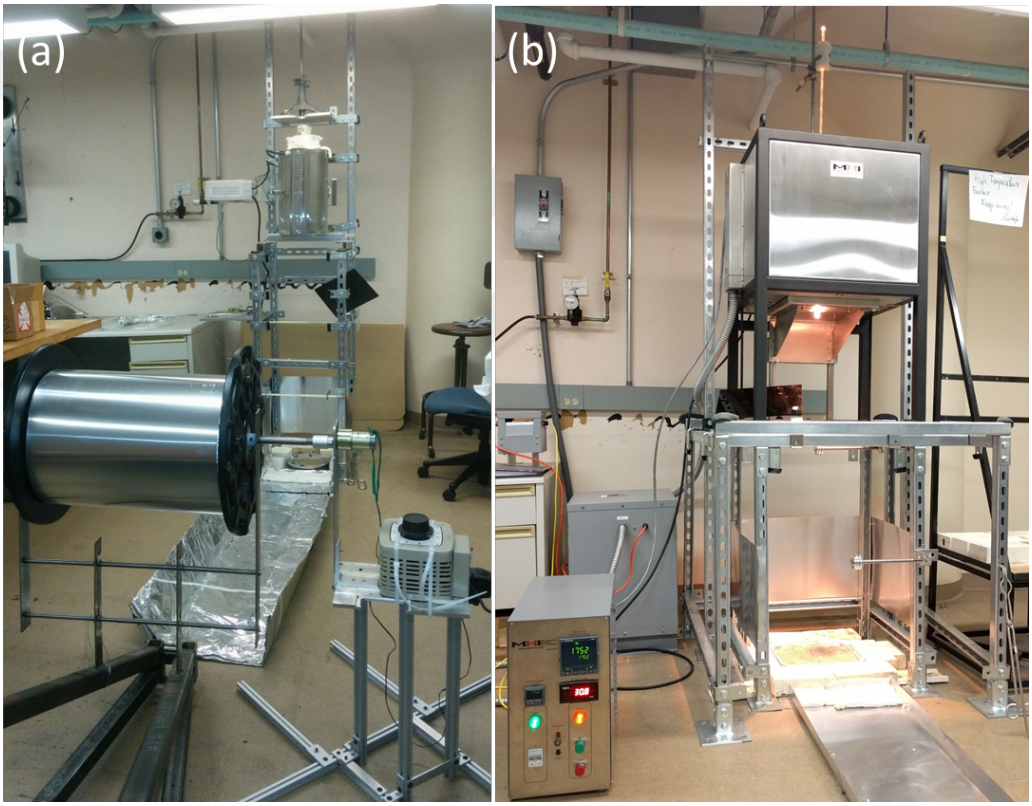

Figure 2·2: Laboratory fabricated mini draw towers for (a) Ge-core borosilicate glass-clad fibers (b) Si-core and SiGe-core silica-clad fibers.

2.1.4 Fiber Drawing

The previously prepared preforms were placed into the appropriate vertically positioned furnace where it heated up to the working temperature of the cladding glass at which semiconductor was is molten. Necking occurs due to the local deformation of the glass cladding due to the changing balance of viscosity and stresses as the temperature is increased.

Fibers were drawn using two types of laboratory fabricated mini draw towers in Department of Mechanical Engineering at Boston University, shown in Fig. 2·2. The setup used for Ge-core borosilicate glass-clad fibers drawing (Fig. 2·2(a)) has a vertical split tube furnace (Mellen Company Inc., New Hampshire) that can go up to 1250^{o}C, as well as a fiber spool with rotational speed control. The fibers were drawn at 1000^{o}C, which is above the melting temperature of Ge. As described in more detail in the next chapter, simulations of the time for the Ge core to melt as well as the start of the neck formation were carried out to estimate how long the molten fiber core is in contact with the borosilicate. It was concluded that placing a cold preform into a hot furnace minimized the interaction time between the molten core and cladding, than placing the preform into a cold furnace and heating up the furnace, due to the limitations on the heating rates of the furnaces. For the case of the Ge-core, borosilicate-clad fibers, the cold preforms were placed into the furnace pre-heated to 1000°C with the location of the Ge-rod right above the expected location of the neck formation. This will be discussed in more detail in the next section.

For the Si-core/SiGe-core, silica-cladded fibers were drawn in the setup shown in Fig. 2·2(b) consisting of a modified glass melting furnace (MHI Inc, Ohio) that can reach 1760^{o}C, a temperature at which drawing of silica fiber cladding is possible. The glass transition temperature of silica ($T_{g,silica}$) is 1683^{o}C. The drawing temperature of 1760^{o}C meant that the furnace was running almost to the limit of its capability,

including using close to the maximum allowable current to maintain the furnace at temperature. It was found that if a cold preform was inserted into the furnace at temperature, the furnace cooled slightly, and the current spike dictated by the controller to bring the temperature back up almost always tripped the furnace. Hence, for the silica cladded fibers, the preform was inserted into the cold furnace and the furnace was then heated to the drawing temperature at a rate of 15°C/min till 800°C, 8°C/min till 1000°C, 4°C/min till 1200°C, 2°C/min to 1600°C and 1°C/min thereafter to the drawing temperature.

According to conservation of mass, the relationship between the fiber and preform is described as

$$L_{preform} \times D_{preform}^2 = l_{fiber} \times d_{fiber}^2 \tag{2.1}$$

where $L_{preform}$, $D_{preform}$, l_{fiber} and d_{fiber} are preform length, preform diameter, fiber length, and fiber diameter, respectively. For instance, a 20 mm diameter, 400 mm preform can be drawn into a 16 km long fiber with 100 μm diameter. Equation 2.1 states that the product of cross-sectional area and length is preserved after a fiber is drawn from a preform. This also implies that in drawn fibers, the area ratio of core and cladding are preserved as in the preform. Depending on the drawing speed and initial core/cladding diameters, fibers with core diameters of 10-200 μm and cladding diameters of 130-500 μm were drawn.

In some cases, canes, which have significantly larger diameters than fibers, were also drawn. Canes are formed during the initial part of neck formation, when the rod in the preform is placed very close to the necking location. When the preform starts to neck, the initial deformation occurs at slower speeds due to the relatively large cross-sectional area of the neck, leading to cane formation. The core diameters of drawn canes ranged between 300-770 μm with the cladding diameters in the range

of 1.3-1.4 mm.

2.1.5 Polishing

After fiber drawing, fibers were prepared for microstructural and optical characterization. In order to improve optical transmission, a fine surface finish is essential for the fiber ends. Portions of the fibers were embedded into epoxy that was hardened overnight. The fiber ends were subsequently polished with an automated polishing machine (Buehler, Illinois). The polishing consisted of sequentially to finer and finer surface finish, starting with 120 grit to 600 grit SiC paper, followed by 9 μm to 1 μm polycrystalline diamond solutions. Lastly, a suspension with 0.05 μm alumina particles was used to finalize the surface finish.

2.2 Fiber Characterization

The composition and the optical properties of the drawn fibers were characterized. Electron microscopy was used for chemical characterization to determine the chemical interaction between the core and the cladding. Optical characterization of fibers was carried out using three different mid-IR light sources. The details of the microstructure and optical property characterization techniques are discussed below.

2.2.1 Transmission Electron Microscopy

Scanning/transmission electron microscopy (S/TEM) combined with energy dispersive x-ray (EDX) spectroscopy provides compositional analysis with a nano-scale spatial resolution. Figure 2·3 shows the FEI Tecnai Osiris 200kV S/TEM used for the chemical characterization in this study. Both dot- and line-mapping techniques were used to investigate the region around the cladding/core interface to determine

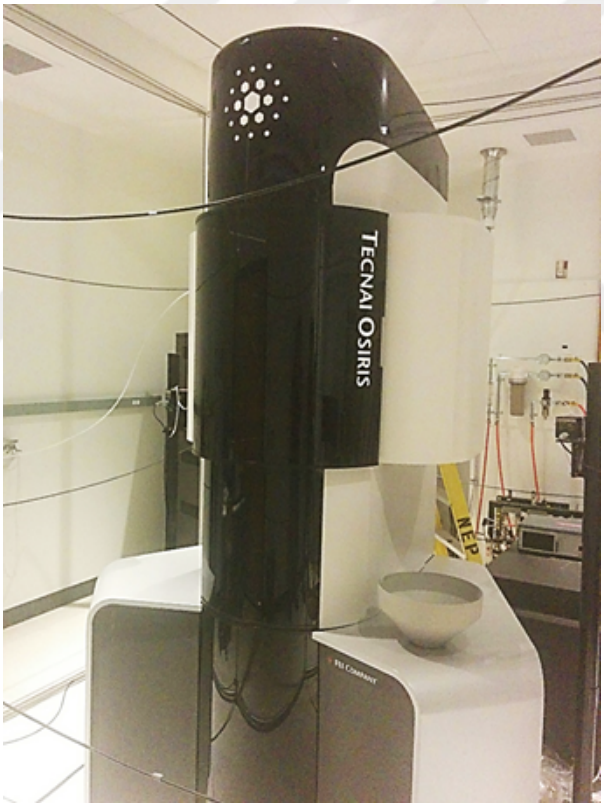

Figure 2·3: FEI Quanta 3D FEG transmission electron microscope.

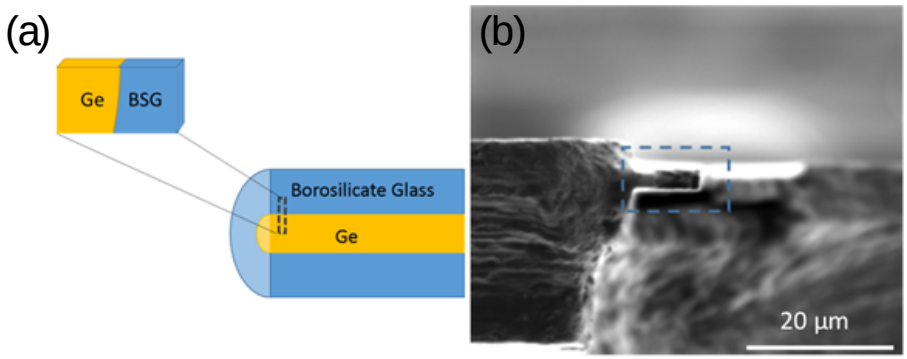

Figure 2·4: a) Schematic image of TEM sample preparation. b) The TEM sample produced by FIB-based lift-off technique.

if there was any significant interdiffusion between the constituents of the core and cladding.

Fibers were polished longitudinally to reveal core/cladding interface. A focused ion beam (FIB, FEI Quanta 3D FEG) based lift-off technique was used to make 100 nm thick electron transparent samples of the core/cladding interface for S/TEM observations. Figure 2·4 shows the schematic of the FIB-based TEM sample preparation.

2.2.2 X-ray Diffraction Spectroscopy

X-ray diffraction spectroscopy (XRD) (Fig. 2·5) is a tool designed to study the crystalline structure of materials (Bruker Discover D8, Wisconsin). In this device, a copper tube is used as an x-ray source. By heating a filament, electrons are produced and are accelerated to the copper tube by a high bias voltage (40 kV). The electron bombardment excites inner shell electrons of the copper atoms to higher energy levels in the outer shells, which is an unstable state. In order to return the stable state, the outer shell electrons move back to their original location in the inner shells, and emit x-rays with energy that is the precisely the energy difference between the two energy levels. The most intense radiation (Cu Kα with a wavelength of 1.5418 Å)

Figure 2·5: Bruker D8 Discover x-ray diffraction system with 2D detector.

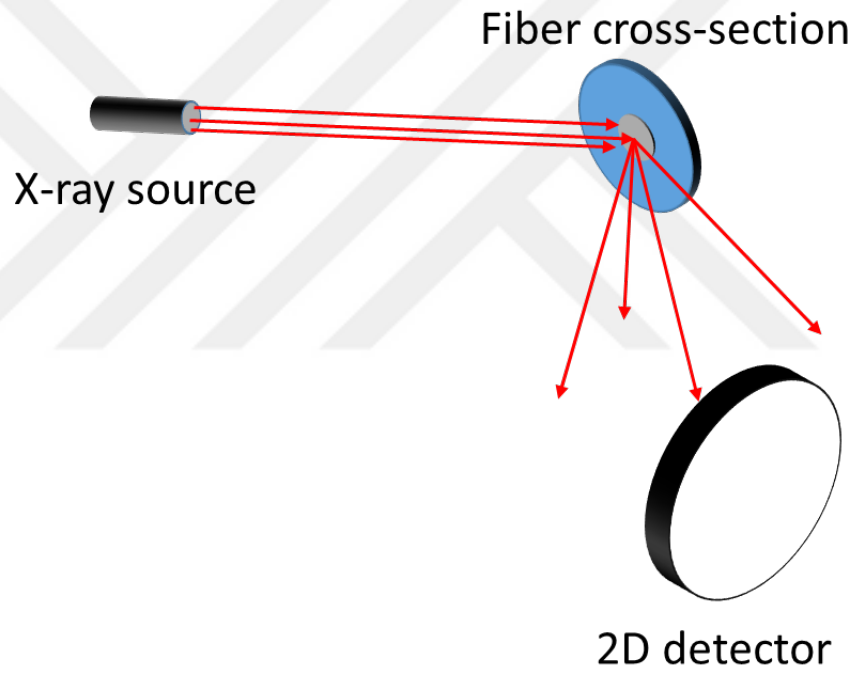

Figure 2·6: Schematic representation of XRD and 2D detector. Constructively interfered x-rays reflect from the sample and are collected by 2D detector.

is used as an input beam to study the crystalline structure of a sample. Apertures are used to eliminate the diverging x-ray, leaving only collimated x-rays in the beam. Constructively interfered x-rays reflect from the sample and are detected by a 2-D detector (Vantec 500, Bruker, Wisconsin) as shown in Fig. 2·6. Single and polycrystalline materials can be differentiated by spot versus ring diffraction patterns on the 2D detector respectively.

2.2.3 Electron Backscatter Diffraction Spectroscopy

Electron backscatter diffraction spectroscopy (EBSD) is a microstructural and crystallographic analysis technique that can be incorporated into an SEM. The method characterizes crystal orientation and grain morphology, thereby allowing the study of grain size and the nature of grain boundaries in the sample being examined. Electrons from the SEM are diffracted by the top atomic layers of individual grains of crystalline materials to form electron backscatter patterns called "Kikuchi bands". The crystalline structure and crystallographic orientation of these individual grains can be obtained by matching these patterns with a comprehensive database. An Oxford Instrument (the UK) EBSD detector is used for crystallographic characterization in this study.

2.2.4 Fourier Transform Infrared Spectroscopy

Fourier transform infrared spectroscopy (FTIR) was used to characterize the optical properties of the drawn canes. Figure 2·7 shows the FTIR device used in this study (Bruker Optics Inc., Massachusetts). A Globar blackbody radiation source emits mid-IR wavelengths by heating an U-shaped silicon carbide target. A beam splitter inside the FTIR splits the incoming light into individual wavelengths in a working range of 7500 cm^{-1} (1.33 μm) to 370 cm^{-1} (27.03 μm) and guides them to the interferometer. Each wavelength undergoes constructive interference at the

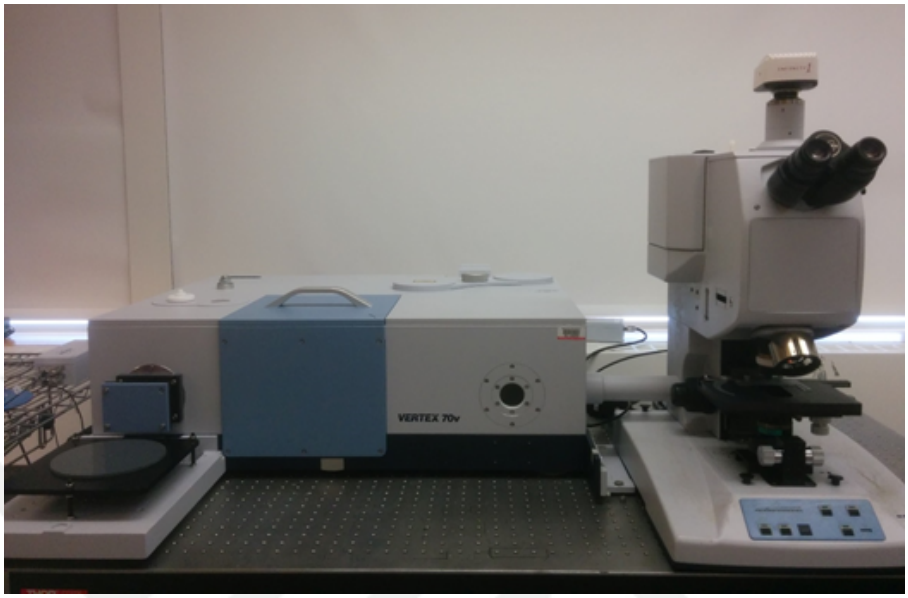

Figure 2·7: Photograph of the FTIR setup, with a bench type Bruker Vertex 70v on the left and a Bruker Hyperion microscope on the right.

interferometer and is sent to the sample. On the other side of the sample, a mercury cadmium telluride (MCT) detector collects the output light that goes through the sample, and defines the transmission characteristic of the sample. The detector operates in the range of 12000 cm^{-1} (0.83 μm) to 600 cm^{-1} (16.67 μm). Thus, the FTIR has a working range of 1.33-16.67 μm, which covers the mid-IR range of interest for the optical fibers being examined.

2.2.5 Quantum Cascade Laser

Quantum cascade lasers (QCL) are powerful mid-IR light sources that can range from 2.75 μm to 161 μm [30-32]. In contrast to diode lasers, the lasing transition in a QCL occurs between states within a given quantum well rather than between the conduction band and valance band of the semiconductor material. The quantum well is a thin layer of semiconductor material, deposited by molecular beam epitaxy (MBE) or metal-organic chemical vapor deposition (MOCVD), which confines electrons or

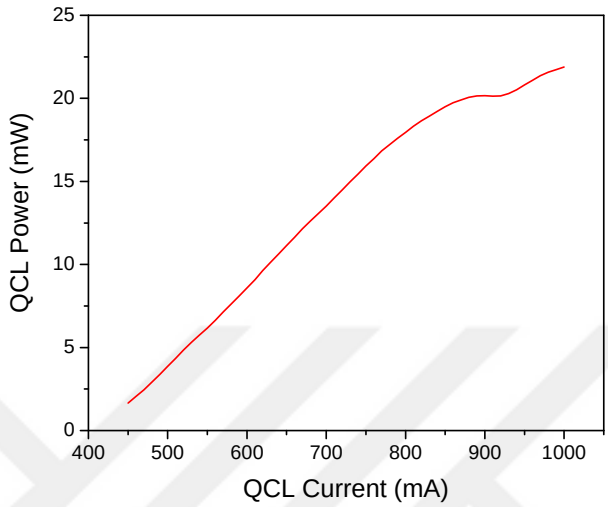

Figure 2·8: QCL output power versus current.

holes only in the dimension perpendicular to the layer surface. Thus, the operating wavelength depends on quantum well depth.

In this study, two types of QCLs were used for characterization purposes. A QCL (Daylight Solutions Inc., California) with 1580 cm^{-1} (6.33 μm) to 1740 cm^{-1} (5.75 μm) spectral range was utilized for measuring transmission through the fibers. The output power was adjusted by controlling the current in a range of 450 mA to 1000 mA. Figure 2·8 shows a plot of the current versus power.

Figure 2·9 shows the experimental setup for the QCL measurements. The output light from the QCL is guided by gold mirrors and focused on the fiber surface using a ZnSe lens with a focal length of 6 mm. On the output end of fiber, two other ZnSe lenses with the focal lengths of 25.4 mm (1 inch) collect and transmit output light to a MCT detector (Electron-Optical Systems Inc., Pennsylvania).

The second QCL (Lasertune, Block Engineering, Massachusetts) with 770 cm^{-1} (13.0 μm) to 1870 cm^{-1} (5.35 μm) spectral range was used for transmission loss measurement and output light imaging. The experimental setup for this laser is

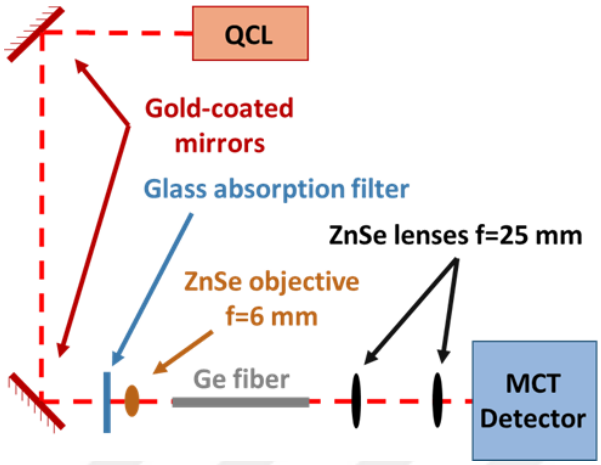

Figure 2·9: Schematic representation of QCL experimental setup.

similar to the setup of the first QCL, with an additional path containing two flip mirrors and one stationary mirror added as a reference path for loss measurements. The glass absorption filter was replaced with a 0.3 neutral density (ND) IR filter to lower the absorption. An electro-optic type detector was placed in sequence with the QCL in order to measure the transmission (i.e. sample/reference signal intensity ratio). Although this QCL had a wider transmission window, its average power was lower. Also, this QCL did not have the ability to adjust the output power using current control.

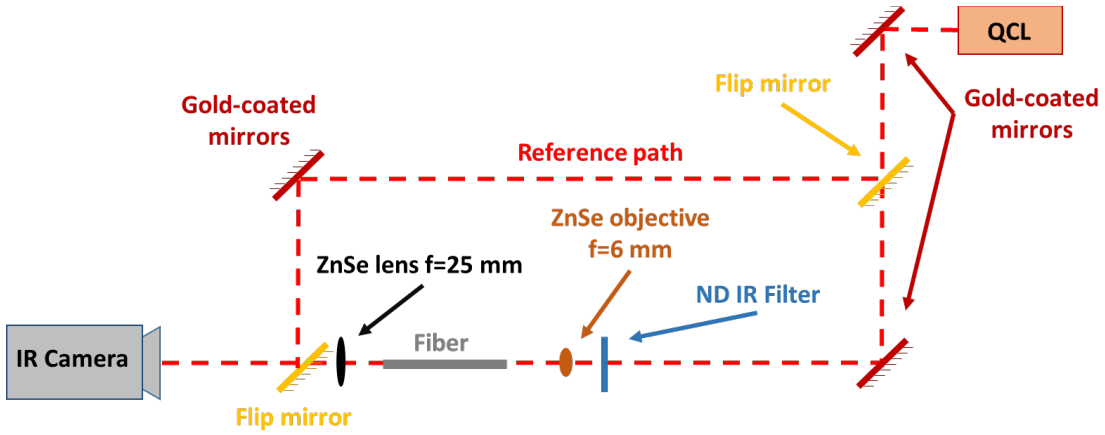

Figure 2·10: Schematic representation of QCL experimental setup for imaging.

A modified setup with an IR camera was built in order to image the output light of the fibers. Figure 2·10 shows the experimental setup for imaging. The MCT detector and one of the output lenses were removed and an IR camera (FLIR, Sweden) was inserted to the setup. The camera had an uncooled microbolometer detector with the detection range of 7.5-14 μm. A Ge lens with 25.4 mm focal length was mounted on the camera to adjust the focus. The camera was able to capture high resolution images due to its 640 $\times$ 480 pixel resolution and 50 Hz frame rate.

2.2.6 Femtosecond Mid-IR Pump-probe Spectroscopy

Pump-probe experiments were performed on a 2DIR femtosecond system shown schematically in Fig. 2·11. Mid-infrared femtosecond pulses were derived from a regeneratively amplified 800 nm 35 fs laser capable of operation at 7.5 mJ/pulse. Approximately 50% of this beam was sent to an optical parametric amplifier (OPA) used to generate a signal and idler pulses in the near-infrared region. A home-built difference frequency generator (DFG) was used to produce $\sim$10 μJ tunable mid-IR pulses. For this experiment, the carrier wave was tuned to 2170 cm^{-1}, and the bandwidth was $\sim$300 cm^{-1} associated with a pulse width of $\sim$90 fs full-width-at-half-maximum (FWHM) operating at about 1.4$\times$ the transform limit. The spatial mode of the beam was Gaussian. The infrared beam was split into pump and probe pulses. A third beam for 2D IR studies was not used in the experiments reported here. The delay between pump and probe pulses was set by translating retroreflectors mounted on stepper motor controlled linear translation precision stages with 1 μm repeatability. The zero-crossings of the interference pattern resulting from co-propagating HeNe beams (632.8 nm) were used to determine the stage position and associated delay between pump and probe beams focused onto the input end of the Ge fiber sample using an off-axis paraboloid mirror. The generated third-order signal beam was collected from the output end using another off-axis paraboloid, dispersed by

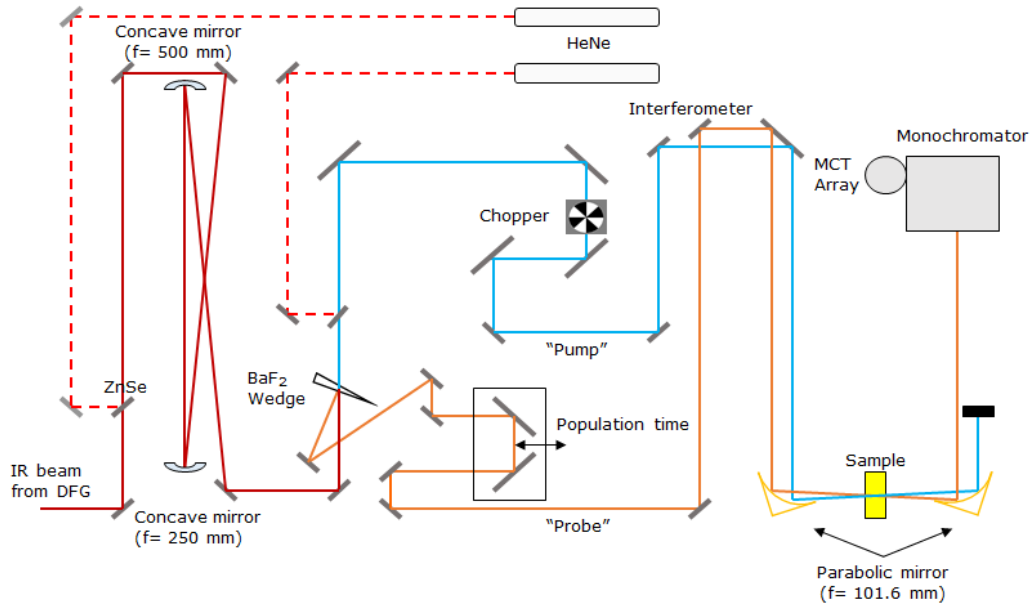

Figure 2·11: 2D Schematic representation of Pump-Probe experimental setup. IR beam from DFG is split into pump and probe beam by a BaF_2 wedge. Two beams hit on the same spot of the sample by using parabolic mirror. At the output end, another parabolic mirror collects the pump and probe lights. Pump light is blocked whereas probe light is collected by the monochromator.

a monochromator and detected using a liquid-nitrogen cooled MCT linear detector array. Polarization control allowed for the detection of either the dichroism signal or the birefringence signal. As stated before, the probe pulse served as its own local oscillator with measurements of both amplitude and phase available in heterodyne detection. A 3D schematic representation of the same setup is shown in Fig. 2·12 for better visualization.

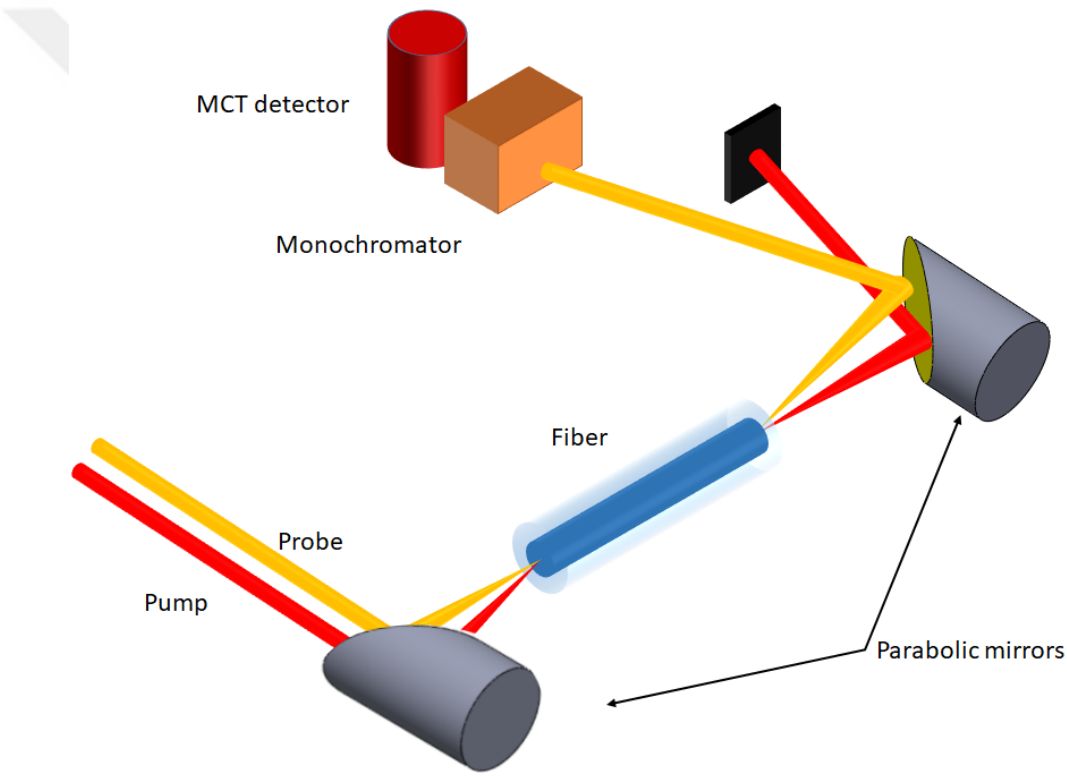

Figure 2·12: 3D Schematic representation of Pump-Probe experimental setup.

Chapter 3

Germanium Fibers

3.1 Simulation of Neck Formation and Core Melting

The presence of impurities like oxygen in the core region can lead to relatively high transmission losses. The drawing process takes place at 1000°C where Ge core is molten. Since the rate of mass transport in liquids is high, any impurity diffusing out of the cladding to the core will quickly be distributed across the core cross-section. Thus the amount of impurity in the core is likely affected by its concentration in the cladding, the rate of diffusion in the cladding, the solubility limit in the core, and the time the core remains in the molten state before it is drawn and solidified rapidly. This suggests that reducing the time the core remains molten before it gets drawn into a fiber is important. Also, since the solubility limit typically follows an Arrhenius dependence on temperature, reducing the drawing temperature while maintaining the core as liquid, is also important.

To minimize the time the Ge remains molten, it is essential to know the initial location of neck formation in order to place the germanium core at the correct location. If the Ge rod is below the necking location, it will not participate in the fiber drawing process. If it is in the location of the neck formation, a significant portion will be lost due to initial cane formation. If it is significantly above the location of neck formation, the molten Ge will be in contact with the cladding material at temperature for a long time, before the deformation reaches the Ge core. Ideally it should be slightly above the location of neck formation so that as the drawing process reaches a steady state,

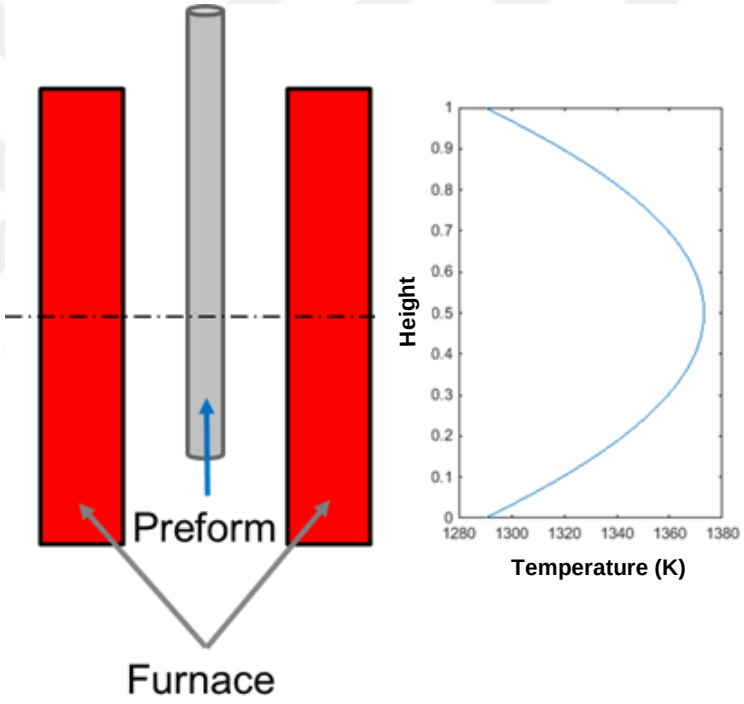

Figure 3·1: Schematic of furnace setup in simulation. Furnace has Gaussian temperature profile.

the molten Ge becomes a part of the deformation.

In order to locate the position where necking starts, simulations of the preform deformation was carried out. The temperature dependent viscosity of the borosilicate glass was used in the simulation, and a Gaussian temperature profile was assumed for the furnace (Fig. 3·1), based on the measured temperature profile of the furnace. Intuitively, the location of the hottest temperature in the furnace corresponds to the softest glass. However, the stresses at the top of the preform is the highest, since it has the most weight of the preform below it pulling down due to gravitational forces. Thus, the likely location of necking initiation is expected to be somewhere in between the location of maximum temperature and maximum stress, i.e., at a point above the location of maximum temperature in the furnace. Figure 3·2 shows the result of one such simulation at three different times; i.e., before any significant deformation has occurred, start of the deformation, and a clear formation of a neck. The simulation results show that if the location of the hottest temperature in the furnace does not change, for a fixed location of the preform with respect to the furnace, the necking point is independent of preform size and furnace temperature setting as long as it is above the softening point of borosilicate glass. This will allow us to place the Ge rod relative to the location of neck formation in a repeatable and consistent fashion.

Furthermore, two options were considered; inserting the preform into a cold furnace, and letting it heat up to the drawing temperature of the furnace, and inserting a cold preform into a furnace already at the drawing temperature. In the former case, since the furnace cannot be heated up rapidly, the time the molten core remain in contact with the cladding before drawing starts is the time the furnace to heat up from the melting temperature of Ge and (938°C) to the drawing temperature (1000°C). Assuming that the furnace can be heated as quickly as 15°C/min (although, in reality, the heating rate needs to be slowed down significantly near the drawing temperature

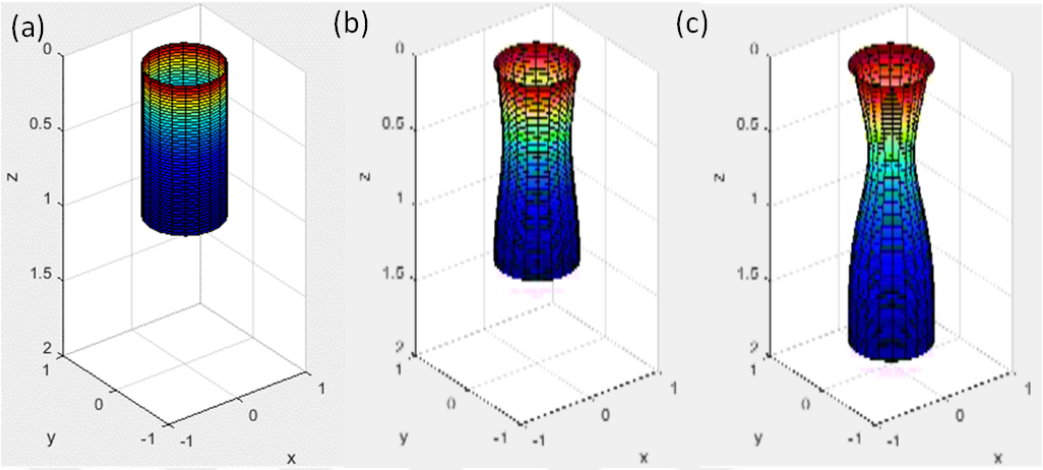

Figure 3·2: Simulation results. (a) Before deformation, (b) the beginning of deformation and (c) neck formation. Colors from blue to red represents the coefficient of viscosity where red is the highest and blue is the lowest.

to reduce the temperature oscillations as the controllers bring the final temperature to the set-point), the molten Ge will be contact with the cladding for ∼250 seconds before the preform reaches the drawing temperature. Experimentally, the necking time of a 9 mm OD borosilicate clad fiber was found to be 94 seconds, implying that the total time the molten Ge core would be in contact with the cladding before drawing starts would be 344 seconds.

To estimate the length of time the Ge core will be molted before necking, if a cold fiber was inserted into a furnace already at the drawing temperature, the heating of the preform was simulated. It was found that the 3mm Ge rod in a 9mm OD borosilicate cladding was completely molten in 12 seconds when exposed to 1000°C. Given the experimental necking time of 94 seconds, implies that in this case, the Ge rod stays in contact with the borosilicate glass cladding for only 82 seconds before drawing starts. Thus insertion of a cold preform into a hot furnace was chosen as processing path to limit impurity diffusion from the cladding to the core.

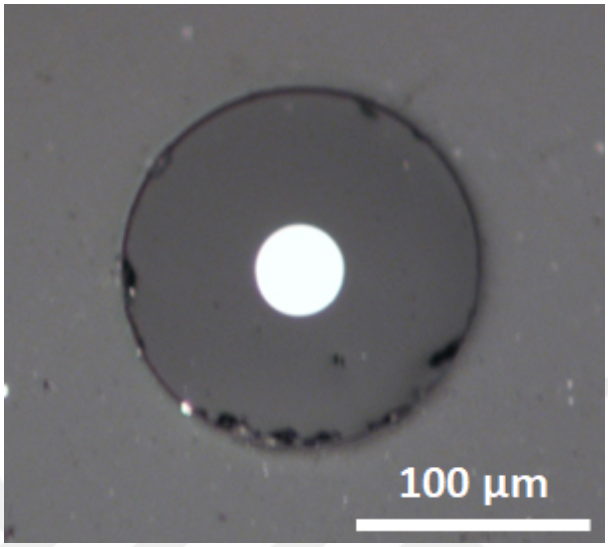

Figure 3·3: Optical micrograph of a polished cross-section of a Ge-core fiber.

3.2 Fiber Drawing

The fiber results reported in this section is based on fibers drawn from a 9 mm OD preform. The drawn fibers had a 40 μm Ge-core diameter and a 177 μm borosilicate glass cladding diameter. The polished cross section of a fiber, imaged by optical microscopy (Nikon Eclipse LV150, Japan), is shown in Figure 3·3.

3.3 TEM Results

The microstructure of the fibers was characterized by S/TEM and S/TEM-based EDX. Figure 3·4 shows a TEM cross-sectional bright-field micrograph of the interface between Ge core and borosilicate cladding with EDX mapping, and an EDX line scan across the core/cladding interface. Both the dot-mapping and line scan data clearly shows that the diffusion of cladding components (Si, O, B, K, Na and Al) from the cladding to the core is minimal, with diffusion distances of the order of 10s of nm. This low level of oxygen diffusion is likely due to the relatively low drawing temperature,

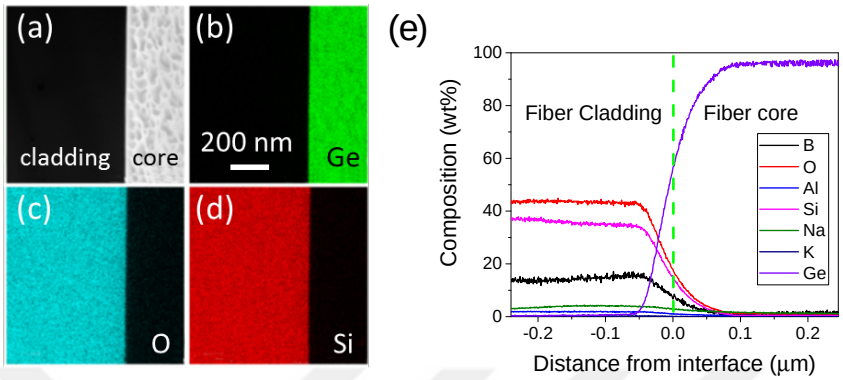

Figure 3·4: (a) TEM bright-field micrograph of the fiber cross-section at the core/cladding interface. (b) Ge, (c) O, and (d) Si EDX dot-maps. (e) EDX line scans across the core/cladding interface of the fiber showing the composition profile of Si, Ge, O, B, K, N and Al. Diffusion of oxygen from the cladding to the core is minimal.

and is encouraging, since the presence of oxygen is known to significantly increase mid-IR transmission losses in the fiber [Ordu et al., 2016].

The core-cladding interface was observed by High Resolution Transmission Electron Microscopy (HRTEM), an HRTEM micrograph of the interface is shown in Fig. 3·5. The crystalline quality of the Ge-core is evident in the micrograph, with the borosilicate glass preserving its vitreous structure.

3.4 XRD Results

The crystallinity of the Ge core was further investigated by RSM with a 1 mm x-ray beam, using a 2D detector. The scan, shown in Fig. 3·6, shows a single (111) peak orientation, indicating that the region interrogated by the 1 mm beam is a single crystal. The 2θ value of the peak location (27.22) indicated that the Ge core is in slight tension (0.31%) compared to unstrained Ge. This is consistent with a recent report of slight red shifting of the T_{2g} Raman mode frequency from a Ge fiber core deposited by high-pressure CVD compared to an unstrained Ge reference [Ji et al., 2017].

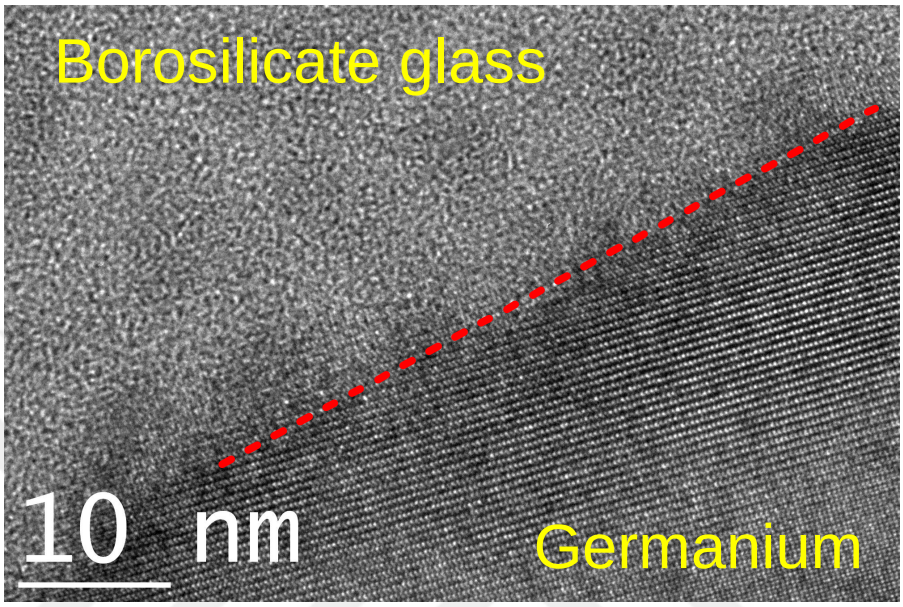

Figure 3·5: HRTEM micrograph of core-cladding interface of the Ge-core fiber, showing the single crystalline nature of the core.

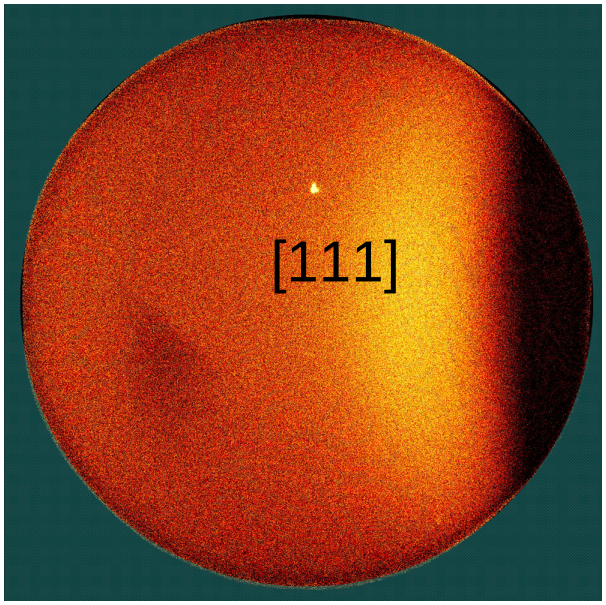

Figure 3·6: Reciprocal space mapping of the Ge core with 1 mm x-ray beam and a 2-D detector, showing a single (111) peak

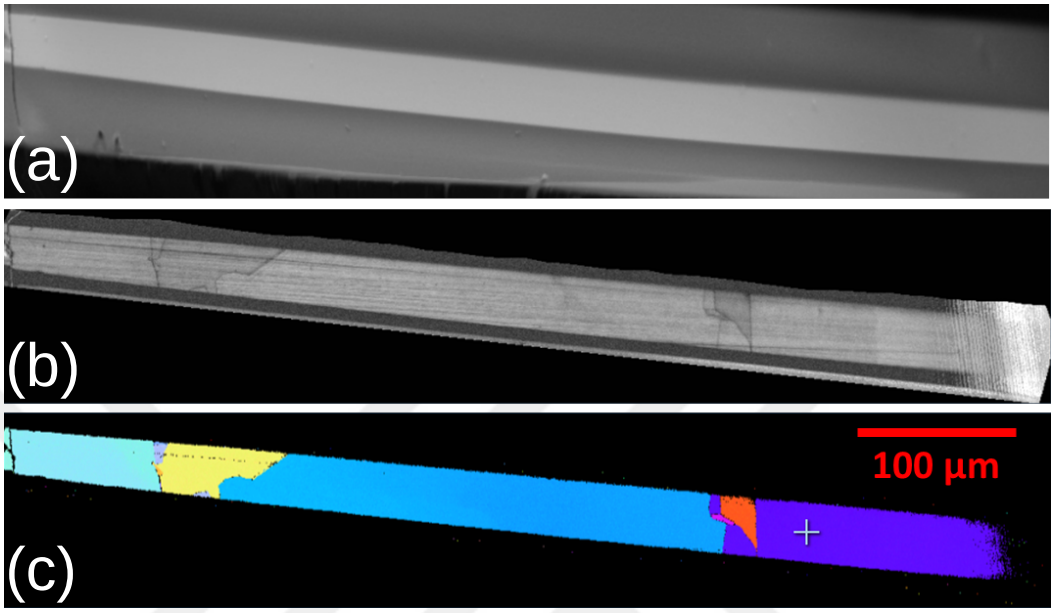

Figure 3·7: EBSD of Ge fiber. (a) SEM micrograph of fiber polished along length to expose the core. (b) Orientation map of grains obtained by EBSD. (c) Orientation key used for map.

3.5 EBSD Results

The grain structure of the Ge-core was also examined by EBSD. Figure 3·7(a) shows the electron micrograph of a fiber polished along its length to expose the Ge-core. Figure 3·7(b) shows an orientation map of the grains based on the orientation key shown in Figure 3·7(c). The red lines show the presence of twin boundaries, indicating that most of the grain boundaries are twin boundaries with excellent registry between grains at the boundaries.

3.6 FTIR Results

Cleaving of the Ge-core optical fibers did not lead to good quality facets due to cracking of the core during the process. Thus, it was necessary to mount the fibers in epoxy, and polish both ends to get good quality facets for optical measurements. This limited the size of the fibers lengths for optical measurements to ∼10 mm. In or-

der to characterize the mid-IR transmittance through a Ge core/borosilicate cladded fiber imbedded in hardened epoxy, it is important to characterize the transmittance through all the materials in the sample, before transmission can be exclusively attributed to the Ge-core. To this end, a borosilicate glass rod and a 3 mm diameter core drilled unprocessed Ge rod were embedded in hardened epoxy (∼10 mm thick), and both ends were polished to a fine finish, exposing the cross-sections of both rods at both ends. The samples was then characterized by FTIR in the range of 1.7-10 μm wavelengths by focusing the beam on the glass rod, the Ge rod, as well as on the hardened epoxy. Figure 3·8(a) shows the transmission results of borosilicate glass and hardened epoxy. The borosilicate glass stops transmitting at wavelength above 3.3 μm whereas the epoxy stops doing so at a wavelength of 2.1 μm. This dictates that any transmission through a Ge-core fiber at the spectral range of QCL (5.82-6.28 μm) has to be through the Ge-core. Figure 3·8(b) shows the transmission through the unprocessed Ge rod. The figure shows that unlike borosilicate glass and epoxy, germanium has strong infrared transmission characteristic, with its transmission ratio increasing from 5-6% at 1.8 μm wavelength to 46% at 2 μm wavelength.

Germanium-core fibers tested with FTIR had insufficient signal to noise ratio for suitable transmission analysis. However, a mounted and polished Ge-cane (351 μm core diameter and 1367 μm cladding diameter) did have sufficient transmission using the FTIR source.

Figure 3·9 shows the comparison of the transmission through the Ge-core cane and the Ge rod. Although the transmission through the cane is lower than the rod,this demonstrates that a molten and re-solidified Ge-core does mid-IR transmit light. Lower transmission of the cane is presumably processing related, most likely from impurities that diffuse into the core from the cladding or due to micro-cracks that might occur during rapid cooling of fiber in the drawing process. Since the diameter of

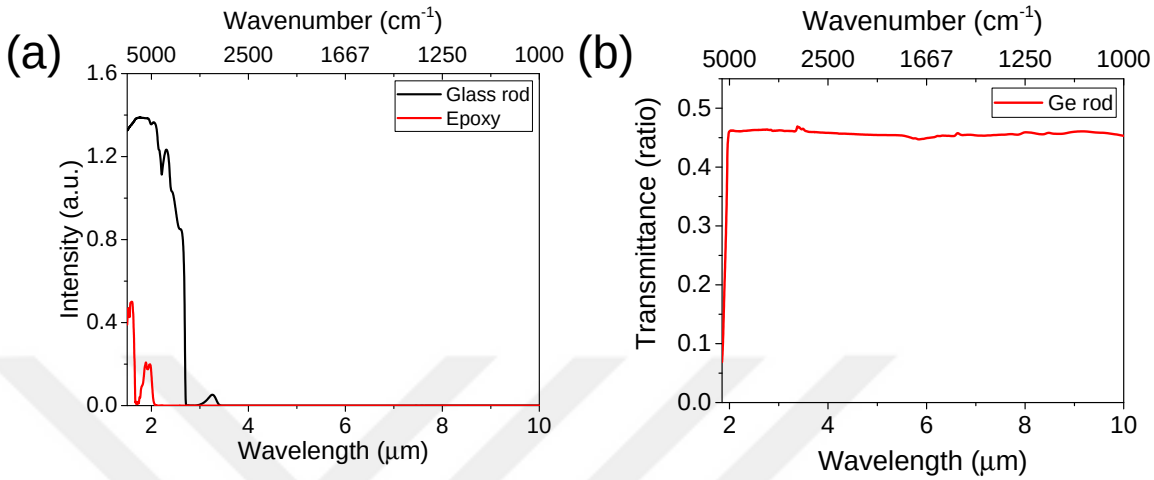

Figure 3·8: Results of wavelength dependent optical transmission characterization using FTIR spectroscopy. (a) Transmission spectra of glass rod and hardened epoxy (b) Transmission spectrum of germanium rod.

the fiber was around one seventh of cane, the effect of impurity diffusion and cracking is more significant for the fibers than canes. This implies that that a more intense source such as a QCL is needed to characterize transmission through the fibers.

3.7 QCL Results

Optical characterization of fibers was carried out using a QCL. To find the center of the core, the input laser beam was scanned horizontally and vertically across the fiber core. Figure 3·10 shows the output of the horizontal and vertical scans. For transmission loss measurements, the laser input was placed at the maximum intensity positions in the horizontal and vertical directions.

Transmission measurements were carried out over the range of the QCL wavelengths (5.82-6.28 μm). The laser was set to 500 mA, corresponding to a power of 3.87 mW, in order to avoid any saturation at the output signal. The starting length

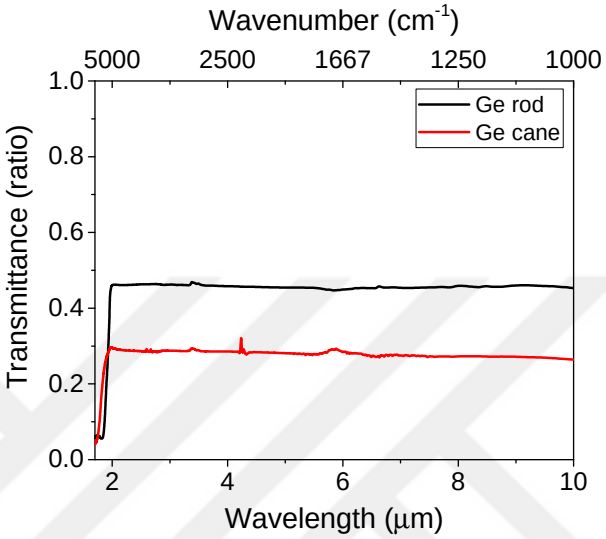

Figure 3·9: Comparsion of an unprocessed Ge rod and a drawn Ge-core cane in FTIR.

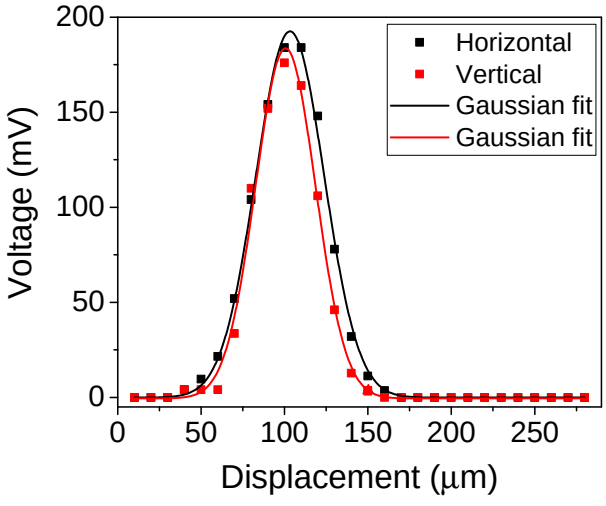

Figure 3·10: Vertical and Horizontal scans of fiber with QCL.

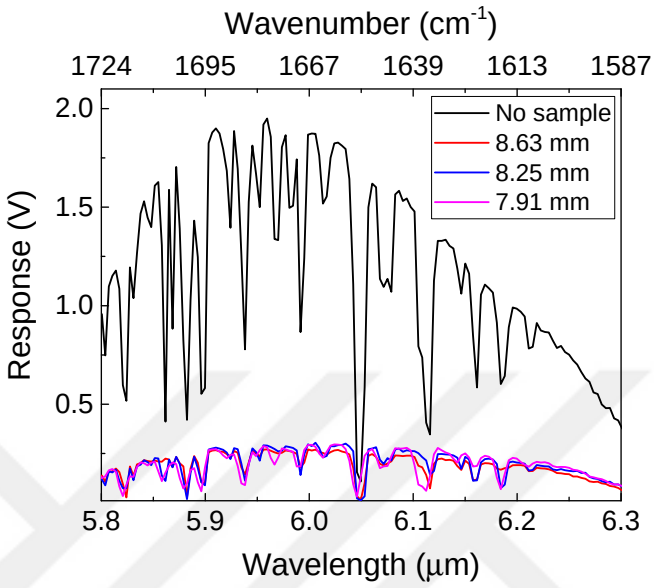

Figure 3·11: Transmission characteristics in the QCL range of Ge fibers of three different lengths of 8.63 mm, 8.25 mm, and 7.91 mm, as well as the laser output signal with no sample in the path of the QCL. The sharp dips are due to atmospheric absorption peaks.

of fiber sample was 8.63 mm. Two additional sets of data were taken by polishing the fiber down to 8.25 mm and 7.91 mm lengths. Figure 3·11 shows the un-normalized output signals of three sample lengths as well as the un-normalized output signal of the laser without any sample in its path. In all these measurements, the same glass filter was used to ensure that the output light did not saturate the detector. The strong dips in the data were correlated primarily to known rotationally narrowed atmospheric absorption peaks in water vapor that are in the range of the QCL [Rothman et al., 2013]. In order to remove the effects of the atmospheric absorption peaks, a 4^{th} order polynomial was fitted for each data set, using data points away from the absorption peaks. Figure 3·12 shows one such fit on the output signal of 8.63 mm fiber. The fitted spectrum was then used to calculate the transmission losses.

Figure 3·11 shows that the small differences between the fiber lengths result in output signals that are not very different. Thus, the output signal at each individual

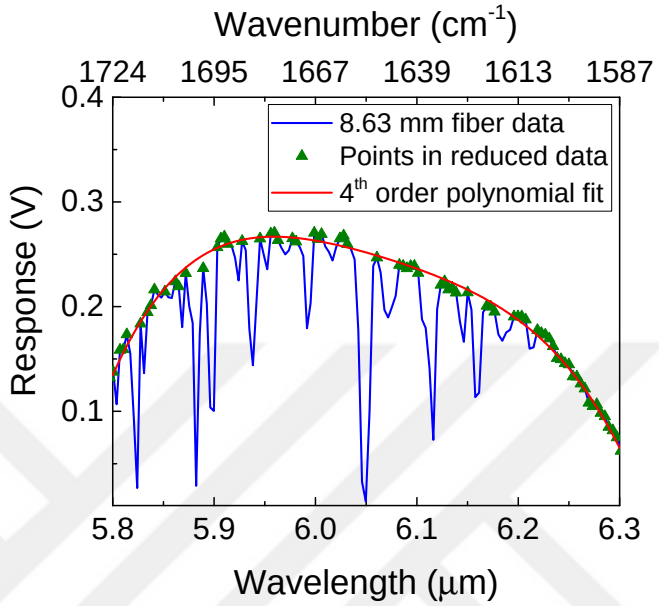

Figure 3·12: Best fit of a 4^{th} order polynomial to the transmission spectrum of the 8.63 mm fiber, using a reduced dataset of points away from the atmospheric absorption peaks.

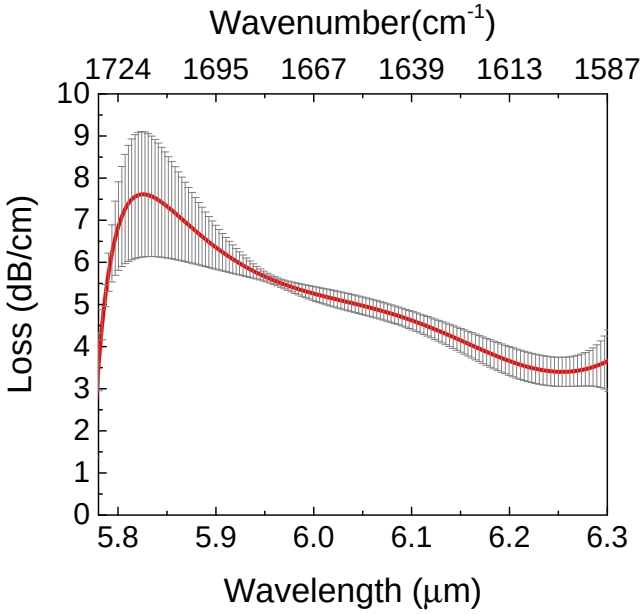

Figure 3·13: Transmission losses of Ge-core fiber.

length was compared with the output signal of the laser without any sample in the path using:

$$\alpha = -\frac{10}{L} log_{10}\Big(\frac{P_0}{0.64^2 P_i}\Big) \tag{3.1}$$

where L is the length of the fiber, P_{fiber} and $P_{background}$ are fiber output power and background power respectively. This led to three sets of wavelength dependent loss data, whose wavelength dependent ranges and average values (red line) are plotted in Fig. 3·13. Figure 3·13 shows that the transmission losses are in the range of 3.1-9.1 dB/cm in the wavelength range of 5.82-6.28 μm. The data at the two ends of the wavelength range is less reliable since the output power of the QCL is lower at the edges of its wavelength range (see background scan in Figure 3·11). Since the wavelength range of the measurement is too narrow to deduce any meaningful trends with respect to wavelength dependence, an average of all the calculated loss values (over a wavelength range of 5.82-6.28 μm for fiber lengths of 8.63 mm, 8.25 mm and 7.91 mm) was computed to be 5.1 dB/cm. The aforementioned measurements accounted for Fresnel reflections at the input and output of the fiber (calculated to be 36% from the refractive index discontinuity between Ge and air), and all the remaining losses were attributed to the fiber. This implies that the calculated loss values are an upper bound of the actual losses in the Ge-fiber core; hence, the actual losses of our fibers may be even lower than the calculated value.

3.8 Significance of Results

To the best of our knowledge, there has been no reported mid-IR transmission with measurement of transmission losses in crack-free Ge-core, borosilicate glass cladded fibers fabricated by the rod-in-tube method which is scalable to commercial fiber manufacturing without the added intermediate layer needed for silica glass cladding. In this study, simulating and experimentally verifying the location of the neck for-

mation in the preform and placing the Ge rod slightly above this location minimized the interaction time between the molten Ge core and the borosilicate cladding before fiber drawing occurred. This led to low impurity diffusion from the cladding to the core resulting in lowest reported loss values for a Ge-core, borosilicate cladded optical fiber produced by the rod-in-tube method that is scalable to manufacturing settings. These fibers transmitted in the 6-m wavelength range, which is of fundamental importance to the studies of proteins, nucleic acids, and phospholipids, as well as to the study polymer composites [27-29].

Chapter 4

Silicon Fibers

4.1 Simulation of Core Melting and Neck Formation

Similar to Ge-core preforms, the necking location of the silica preform was also calculated for the optimal location of the Si-rod in the furnace.

The furnace used for silica drawing has a rectangular inner chamber where the $MoSi_2$ heating elements are positioned uniformly on all four sides. The location of the neck formation was simulated to be ∼2 cm above the maximum temperature point in the furnace, and the Si core was placed just above this location. Heat transfer and necking models predicted that if a 15 mm OD preform was inserted into a furnace at drawing temperature of 1760°C, the melting time of the Si rod was 30 seconds, and the necking time was ∼6 minutes, ensuring that the Si core would be fully molten when necking starts. The longer necking time is related to the higher viscosity of Si at the drawing temperature compared to the borosilicate preform. Ideally, silica should be drawn at higher temperatures (∼2000°C), but the drawing experiments in this case was limited by the available furnace for which 1760°C was close to its maximum operating temperature.

As described in Section 2.1.4, since the furnace was operating close to its maximum operating temperature, the insertion of a cold preform into the hot furnace led to a reduction of the furnace temperature. When the controller sent in additional current to heat up the furnace, the furnace inevitably tripped, which was not good for the rather fragile $MoSi_2$ heating elements. It was thus decided that silica-cladded fibers

would be drawn by placing the preform in a cold furnace, and heating the furnace to the drawing temperature. The heating schedule required (Section 2.1.4) meant that it took ∼4 hours for the furnace to reach the melting point of silica (1414°C) and an additional 4 hours for the preform to reach the drawing temperature, during which time the molten Si was in contact with the silica cladding. The higher temperature and longer time implies that significantly more diffusion of oxygen from cladding to the core is inevitable.

4.2 Fiber Drawing

A silicon-core silica-cladded fiber, drawn at 1760°C from a 15 mm OD preform is shown in cross-section in Fig. 4·1. The fiber has a core diameter of 61 μm and 345 μm. The figure shows that the core and cladding cross-sections are not perfectly circular, and that there is a crack in the cladding, which is due to incomplete fusion of concentric silica tubes during the drawing process. Both these features suggest that the fiber was drawn at a temperature lower than optimal where the coefficient of viscosity of silica was too high. However, since the furnace was already running at its high temperature limit, this could not be corrected in this study.

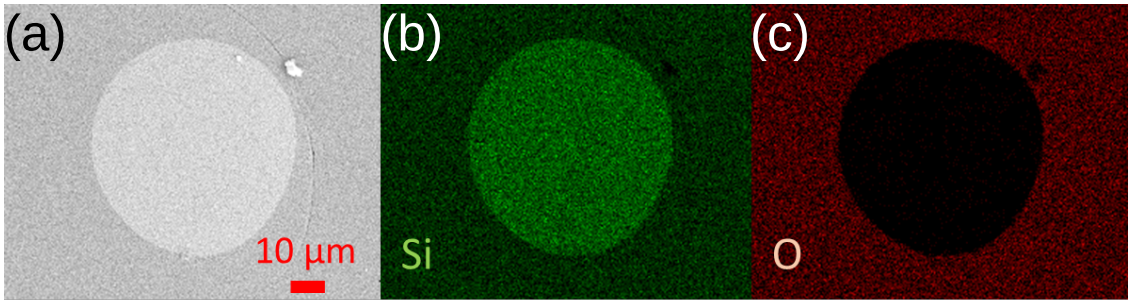

Figure 4·2: (a)SEM micrograph of the fiber. Elemental dot maps of (b) Si and (c) O.

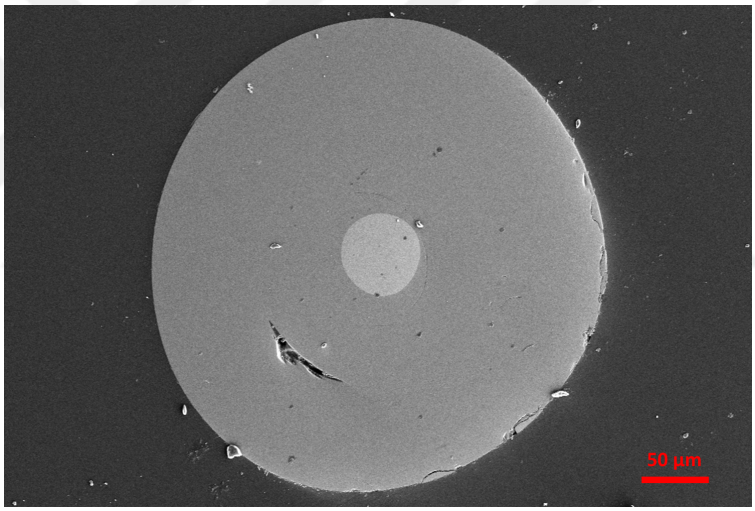

Figure 4·1: SEM micrograph of Si-core silica-cladded fiber in cross-section.

4.3 EDX Results

Microstructural characterization of the silicon-core, silica-cladded fiber was carried out by SEM-based EDX. Figure 4·2 shows elemental dot maps of the fiber, showing the higher concentration of silicon in the core. An EDX line scan across the core and extending into the cladding on both sides is shown in Fig. 4·3. The figure shows that the core had an average oxygen concentration of 3 at%, which is still lower than other reports in the literature [Ballato et al., 2008, Nordstrand et al., 2013], in spite of the

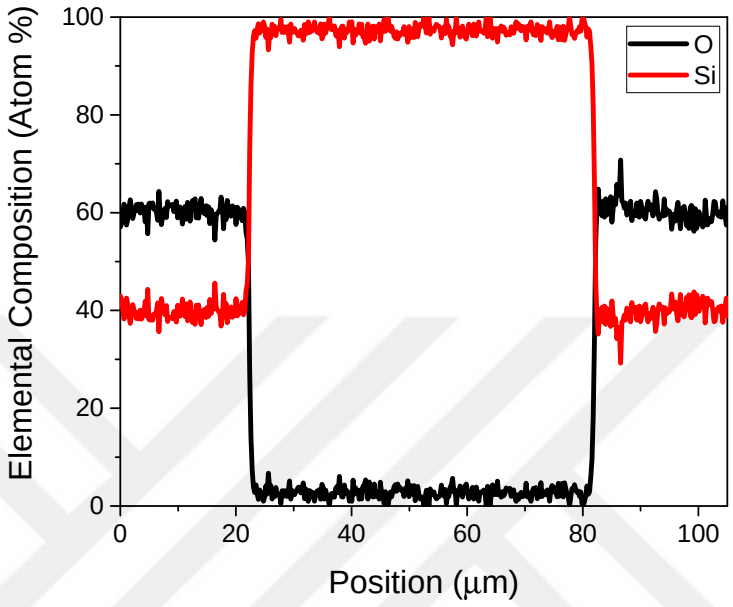

Figure 4·3: EDX line scan across the fiber core and cladding identifies the composition profile of Si and O. The oxygen content of the core due to diffusion from the cladding is ∼3at%.

molten Si core being in contact with the silica cladding for ∼4 hours before drawing. This is likely due to the low drawing temperature in this study, which is around 250-450°C lower than drawing temperatures used conventionally for silicon-core, silica cladded fibers [Oh and Paek, 2012].

This suggests that lowering the temperature can decrease oxygen impurity diffusion from the cladding. Of course, the drawing temperature has to be above the melting temperature of the core. This would require glasses whose working temperature is not far above 1414°C (melting temperature of silicon). Commonly available glasses such as borosilicate and soda lime glasses have working temperatures significantly below this temperature and cannot be used for silicon cores. As seen in this study, silica needs to be drawn at much higher temperatures to maintain circular cross-sections and have complete fusion of the cladding. This suggests that new type

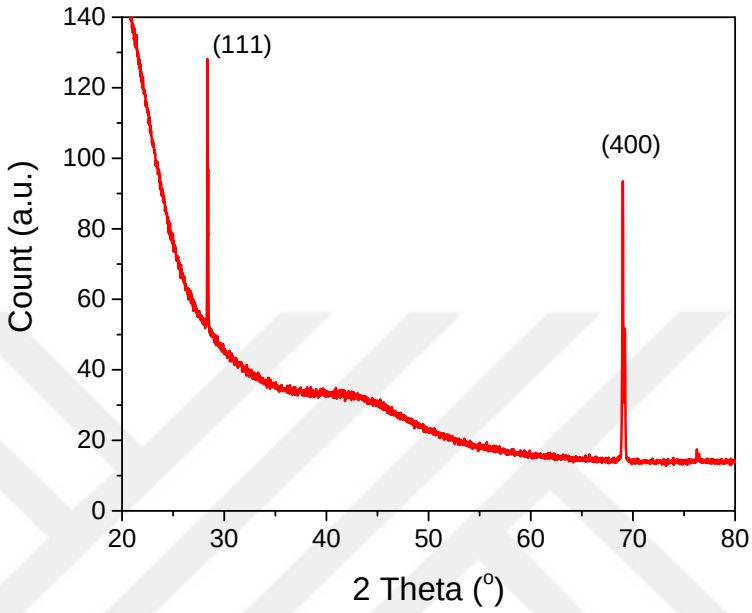

Figure 4·4: $\theta/2\theta$ XRD scan of a Si-core fiber with 1-D detector showing that the fiber core is polycrystalline.

of glasses whose working temperatures are a little above the melting temperature of silicon would be ideal for Si-core fibers. However, exploration of such glasses is outside the scope of this this research.

4.4 XRD Results

The crystalline structure of the Si-core was examined by XRD. The XRD pattern of the Si-core in a fiber polished along its length to expose the core using a 1-D detector and a 1.2 mm slot is shown in Fig. 4·4. The plot shows the (111) and (400) peak orientations, indicating that the Si-core has a polycrystalline structure. The broad peak seen on the left edge of the scan is the signal of hardened epoxy into which fiber was embedded.

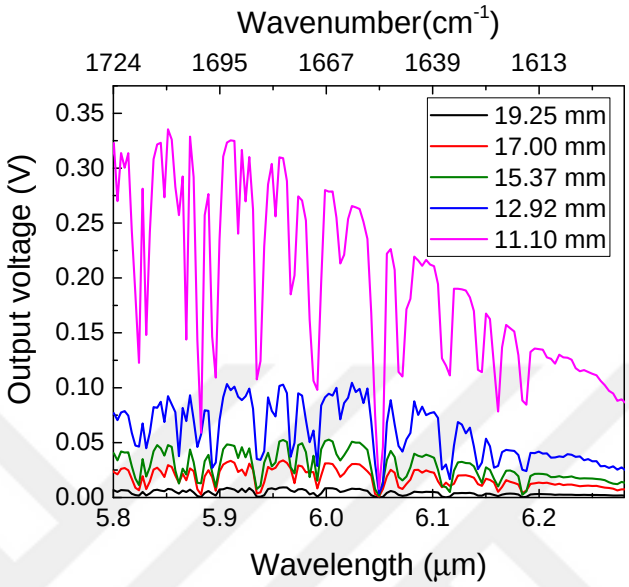

Figure 4·5: Un-normalized output intensity from a Si fiber polished down to different lengths.

4.5 Transmission Loss Measurements

Transmission loss measurements of Si fibers were conducted with a QCL in the range of 5.82 to 6.18 μm with the same setup that was utilized for Ge-core fibers. The laser was set to 500 mA corresponding to 3.87 mW average power. A glass filter was used to prevent saturation at the detector. The starting length of the selected fiber was 19.25 mm. Four additional sets of data were taken by polishing the fiber down to 17 mm, 15.37 mm, 12.92 mm and 11.1 mm. The fiber cross-section, embedded into hardened epoxy, was polished to the same surface finish of 0.05 μm for each measurement.

Figure 4·5 shows the un-normalized output signal from the different fiber lengths. As before, the known atmospheric water vapor peaks leads to sharp dips in the data. In contrast to Ge-core fiber, the difference between the output signals from consecutive measurements was large enough for the cutback losses to be measured by the cutback

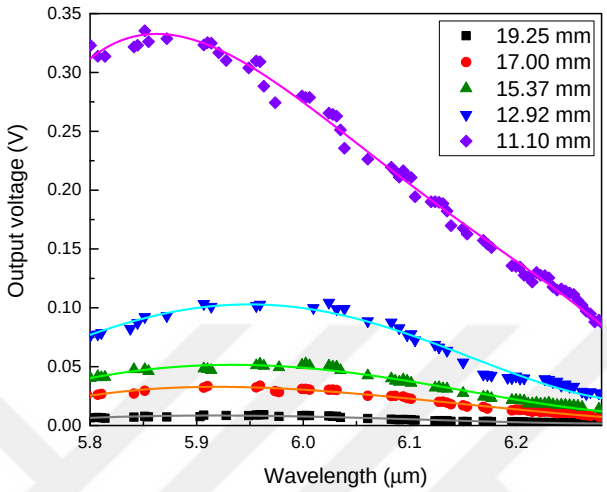

Figure 4·6: 4th order polynomial fits on the data points away from the absorption peaks.

method.

Loss measurements were calculated by fitting a 4^{th} order polynomial to the data points away from the absorption peaks. The results of the 4^{th} order polynomial fit to the output signals from various fiber lengths are shown in Fig. 4·6.

Each transmission data set was compared to that from the shortest fiber length, and the transmission loss was calculated as:

$$\alpha = -\frac{10}{L} log_{10}\left(\frac{P_0}{0.70^2 P_i}\right) \tag{4.1}$$

where L is the length difference between the fiber whose data is being analyzed and the shortest fiber, P_0 and P_i are the output power and input power respectively. In this case, output reading of the shortest fiber became the input power, and longer fiber lengths were used for output power. Equation 4.1 also accounts for Fresnel reflection losses at both fiber facets, which was calculated to be 30% for a Si/air interface.

Calculated transmission losses, plotted in Fig. 4·7, were in the range of 6.8-16.4

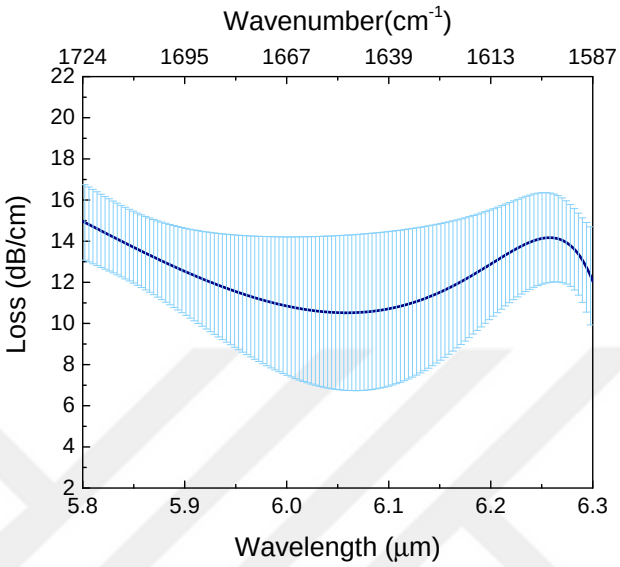

Figure 4·7: Transmission losses of the Si-core fiber. Average loss is 12.45 dB/cm.

dB/cm, and with an average of 12.5 dB/cm, in the spectral range of 5.82-6.28 μm.

The higher losses in the Si-core fibers (compared to Ge-core fibers) could be related to the presence of 3at% oxygen impurity in the core region. Additionally, the larger CTE difference between silica glass and Si (compared to borosilicate glass and Ge) may lead to a higher density of micro-cracks in the core and core/cladding interface, that can act as scattering centers.

Chapter 5

Silicon-Germanium Alloy Fibers

5.1 Graded-Index Fibers

The conventional step-index design of optical fibers has good light confinement in the core region. It is the classic solution for light guiding and is the simplest design for both fibers and waveguides. The previous two types of mid-IR fibers in this study (Ge-core and Si-core fibers) have the step-index profile. When the refractive index difference between core and cladding increases, scattering losses increase in the fiber. Moreover dispersion increases in multimode fibers due to the changing velocities of higher order modes. By creating Graded-index (GRIN) structures in the fiber cores, these fundamental problems can be solved. In GRIN fibers, refractive index profile changes radially from center of the core to the core-cladding interface. Light travels slower in the higher refractive index part i.e. inner part of the core whereas it travels faster at the edges that have lower refractive index. Figure 5·1 shows the comparison between the step-index and graded-index fibers.

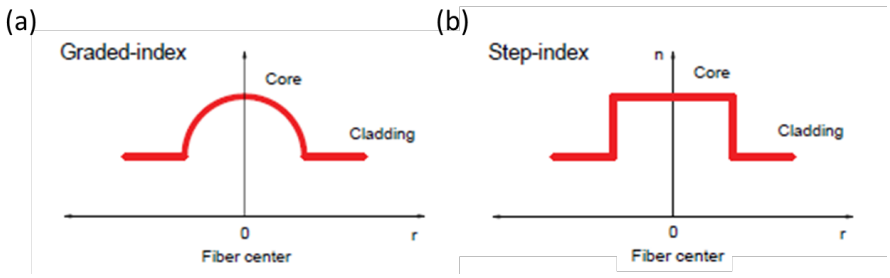

Figure 5·1: Refractive index profile of (a) a step-index fiber and (b) a graded-index fibers with respect to fiber cross-section.

GRIN silica fibers have been developed and have been commercially used for optical telecommunication [Senior and Jamro, 2009]. On the other hand, up to the date there are not any successful Graded-index-infrared (GRIN-IR) fibers available for practical use. The advantages of the GRIN-IR fibers attract many research activities in this field [Gibson et al., 2014]. Thus, the aim of drawing a silicon-germanium (SiGe) alloy-core fiber is to produce a semiconductor GRIN fiber for IR transmission by exploiting the index difference between Ge and Si.

In this chapter, several types of SiGe alloy-core fibers were drawn, and were characterized. Post-drawing processes were performed in order to improve fibers. Here we summarized our semiconductor core-based GRIN fiber drawing efforts with rod-in-tube method.

5.2 Fiber Drawing

The fibers reported in this chapter are drawn from a 15 mm OD silica-based preform at 1760°C. Figure 5·2 shows the electron micrograph of the cross section of SiGe alloy-core fiber. The core diameter of the fiber is 16 μm and cladding diameter is 151 μm. Local segregation of Si and Ge causes non-homogeneous elemental distribution in the fiber core. In this micrograph, lighter-colored regions are Ge-rich and darker-colored regions are Si-rich.

5.3 EDX Results

The microstructural characterization of drawn SiGe alloy-core fibers was carried out with SEM-based EDX. EDX elemental dot mapping was performed on a finely polished cross section of the SiGe alloy-core fiber that is shown in Fig. 5·3(a). Figure 5·3(b)-(c) show the O, Ge and Si elemental dot mappings respectively. Non-homogeneous distribution of elements across the core is evident on the individual

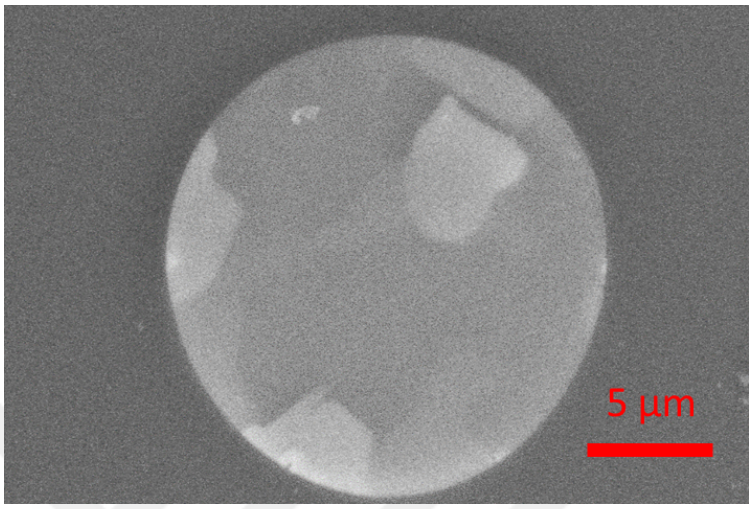

Figure 5·2: SEM image of SiGe alloy-core fiber. Brighter parts of the image are Ge-rich, darker parts are Si-rich regions.

mappings. Oxygen diffusion from cladding to the core is minimal, and it was found 3 at% in the core region. This number matches with the oxygen ratio of previously drawn Si-core fibers that were drawn in similar condition.

5.4 Transmission Loss Measurement

Transmission loss measurements of SiGe alloy-core fibers were conducted in the range of QCL spectrum. The current was set to 700 mA, corresponding to a power of 13.5 mW. The starting length of the fiber samples was around 11 mm. But due to the high transmission losses it was polished down to 6 mm and further polished down for loss measurement. Figure 5·4 shows one such output signal of 4.78 mm long SiGe alloy-core fiber. Similar to Ge and Si fibers, the spectrum also has sharp dips due to atmospheric water absorption. But due to the high losses, the absorption peaks distort the transmission more than the other fibers.

The effect of the atmospheric absorption peaks is more apparent when the transmission is weak. Removing the data points within the vicinity of the absorption peaks

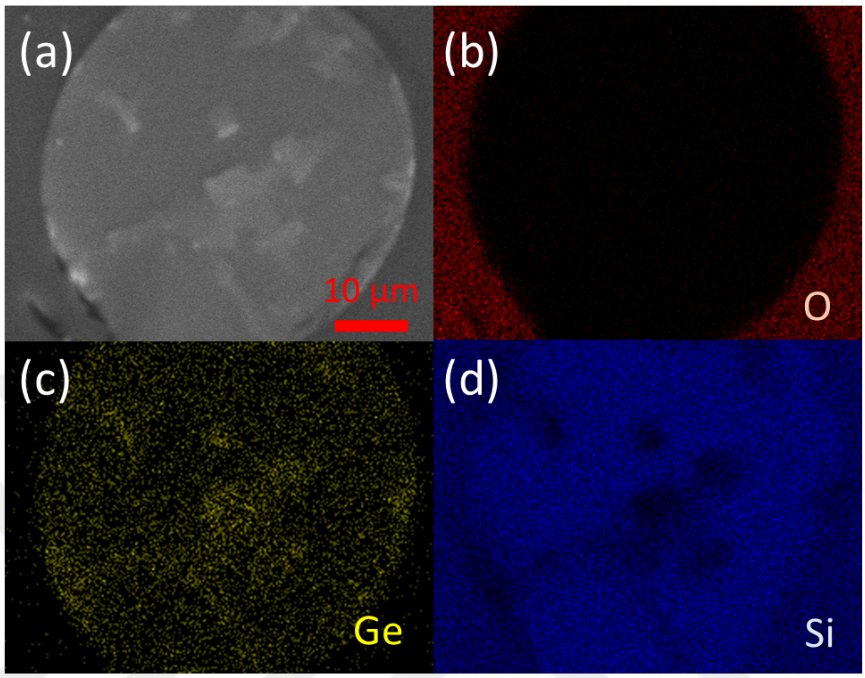

Figure 5·3: (a) SEM micrograph of the core region. EDX elemental dot mapping of fiber elements; (b) O, (c) Ge and (d) Si.

as performed on the Ge-core and Si-core fibers, did not result in the same improvement on the loss calculation of SiGe alloy-core fibers. When the points removed, remained data is too few in number to have reliable fits. Therefore only the individual points were selected and transmission losses were found 75 dB/cm at 6.1 μm. Tremendously high losses could be related to the local elemental segregation in the SiGe alloy-core. Constant refractive index change lead to an increase of the Rayleigh losses. Furthermore, segregation could possibly increase the number of grains which give rise to losses.

5.4.1 Non-equilibrium Solidification

The reason behind the formation of random segregation regions in the fiber core is due to the non-equilibrium solidification during the fiber drawing. Solidification of an alloy happens by multiple nucleation points through the core and if the cooling is

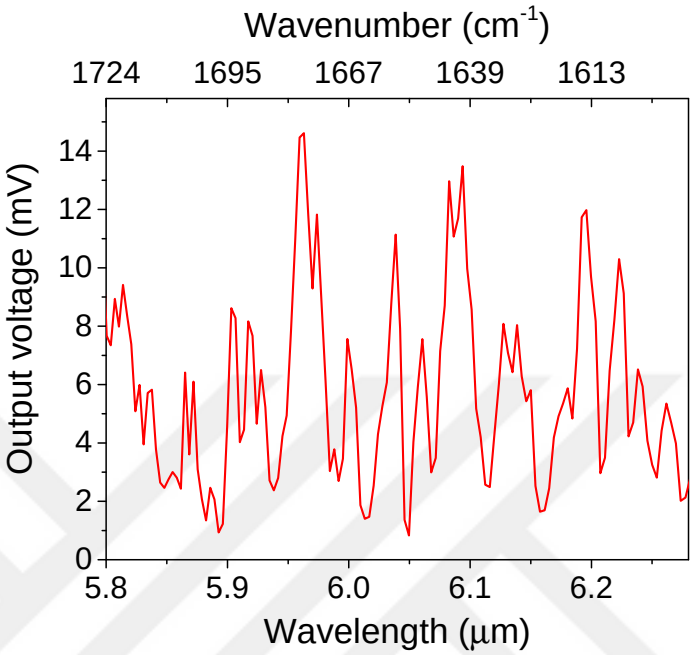

Figure 5·4: Un-normalized output intensity of SiGe alloy-core fiber with 4.78 mm length.

uniform, they appear randomly through the core. These points start growing until the entire alloy region solidifies. If the cooling rate is controlled, elements will diffuse within the nuclei as well as between the nuclei resulting homogeneous composition through the region. On the other hand, when the cooling rate is too fast, the nuclei do not have enough time to form homogeneous distribution of elements and end up with segregation rings around a nucleus with different elemental composition. Figure 5·5 explains a typical non-equilibrium solidification process between two metals; Cu and Ni. Fast solidification forms compositional rings around nuclei with different Cu and Ni percentages.

5.5 Post-drawing Fiber Annealing

Directional solute segregation is the driving mechanism to create GRIN structure. If solute segregation occurs, the outside of the semiconductor core will be Si-rich. If

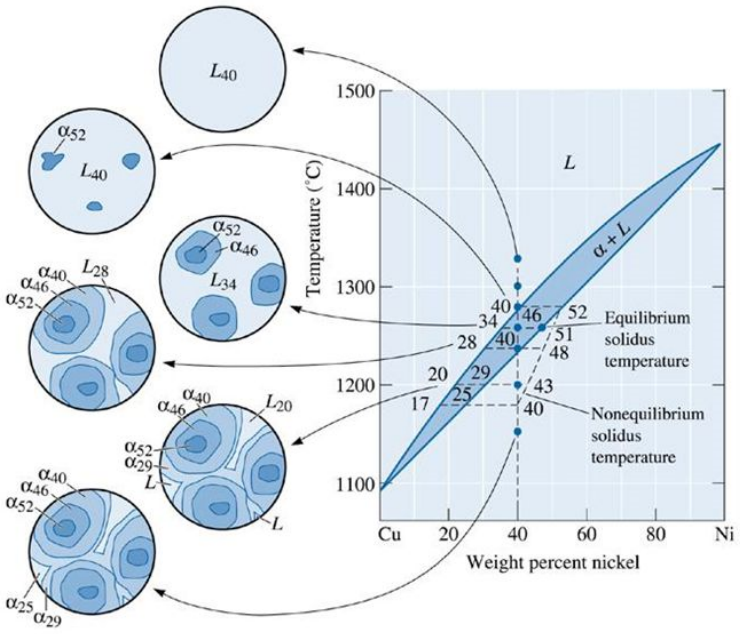

Figure 5·5: Non-equilibrium solidification of Cu-Ni alloy [Askeland and Phulé, 2006].

there is complete mixing of the rejected Ge in the remaining liquid, the composition of the solidified alloy will form GRIN structure. On the other hand, slow cooling will allow equal distribution of the elements on every point of the core, leading to homogeneous step-index SiGe alloy-core fibers. Therefore by controlling the cooling rates different types of SiGe alloy-core fibers can be created.

In order to fix the elemental distribution in favor of creating the GRIN fiber, the cooling rate needs to be slowed down. The cooling rate of fibers during the drawing is in the order of 100-150°C/s. Two options are available to slow down the cooling rate: i) slowing fiber drawing rate, ii) upgrade the draw towers. Slowing the fiber drawing rate lowers the cooling rate but it effects the fiber diameter as well. Draw tower upgrade by adding additional furnaces with lower temperature gradients that requires significant investment. A third solution to this problem could be post-drawing processes. Previously, laser recrystallization with 10.6 μm laser source was

applied to SiGe alloy-core fibers to improve elemental distribution [Coucheron et al., 2016]. The fiber core was heated, with conduction, by exploiting the glass absorption of 10.6 μm light. By controlling the feeding rate of the fiber to the laser beam, core becomes homogeneous during the solidification. Homogeneous alloy core would be another aspect of SiGe alloy-core fibers, creates a step-index fiber but it may not have the same improvement as the GRIN structures.

Here we applied different post-drawing annealing processes with furnaces in an effort of creating GRIN structure with SiGe alloy-core fibers. All the annealing temperatures were selected lower than the softening temperature of the cladding glass, silica.

Furthermore additional annealing recipes with slow cooling rate were applied in order to increase the homogeneity and form a SiGe alloy-core step-index fiber. Alloy step-index fiber would be an alternative to Si-core and Ge-core step-index fibers, having adjustable transmission spectra by controlling the composition would be useful for the mid-IR fiber technology.

5.5.1 Annealing with Rapid Cooling Rates

For the purpose of creating GRIN structure, relatively rapid cooling was performed by using two different annealing recipes, defined in Tables 5.1 and 5.2. In the first recipe, a fiber was heated to 1430°C above the melting point of Si, and dwelt at that temperature for 12 minutes. Later it was cooled to 1330°C with 20°C/min. This fiber was annealed vertically and pulled out of the furnace when the temperature reached to 1330°C. Fiber rapidly cooled in normal atmosphere.

On the second recipe, a fiber was heated to 1465°C and stayed for 6 minutes. It was later cooled to 1340°C with 15°C/min and dwelt for 6 more minutes. Finally it was cooled to the room temperature by free cooling in the furnace.

Figures 5·6 and 5·7 show the fibers from heating recipe 1 and recipe 2 respectively.

Table 5.1: Heating recipe 1 for annealing with rapid cooling rate.

Step	Action	Temperature(s) (°C)	Rate (°C/min)	Time (min)
1	Heating	R.T. → 1430	5	178
2	Dwelling	1430	NA	12
3	Cooling	1430 → 1330	20	5
4	Cooling	1300 → R.T.	Free-cooling	NA

Table 5.2: Heating recipe 2 for annealing with rapid cooling rate.

Step	Action	Temperature(s) (°C)	Rate (°C/min)	Time (min)
1	Heating	R.T. → 1465	10	150
2	Dwelling	1465	NA	6
3	Cooling	1465 → 1340	15	2
4	Dwelling	1340	NA	6
5	Cooling	1340 → R.T.	Free-cooling	NA

On both cases solidification occurred randomly, and non-homogeneous elemental distribution dominated the cores. Post-drawing annealing with rapid cooling rates did not create either GRIN structure or homogeneous core structure.

5.5.2 Annealing with Slow Cooling Rates

The aim of creating these recipes with lower cooling rates ($\sim$ 1-5°C/min) is to increase homogeneity across the core and form a SiGe alloy-core step-index fiber.

In one such a recipe, a fiber was heated to 1430°C and dwelt for 12 minutes. The temperature was decreased to 1300°C and 1000°C with 1°C/min and 5°C/min cooling rates respectively. Finally the furnace was free-cooled to the room temperature. Table 5.3 gives the step by step parameters of annealing process.

Figure 5·8 shows the electron micrograph of the fiber with the above mentioned recipe. The borders between the random segregation regions are blurrier than the previous samples. EDX analysis in Fig. 5·9 proves the enhancement of the elemental distribution by increasing the homogeneity within the core region. However the core still has random segregation regions.

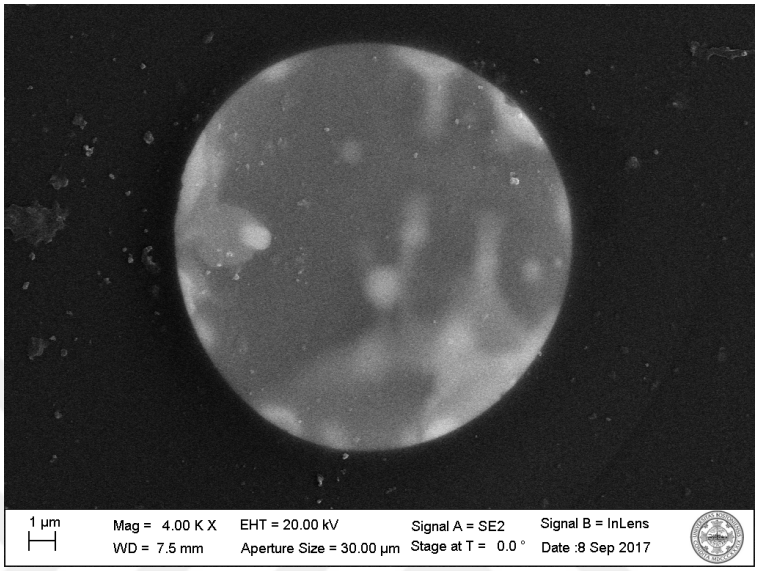

Figure 5·6: Annealed fiber with heating recipe 1 for annealing with rapid cooling rate. Random segregation can be seen across the core region.

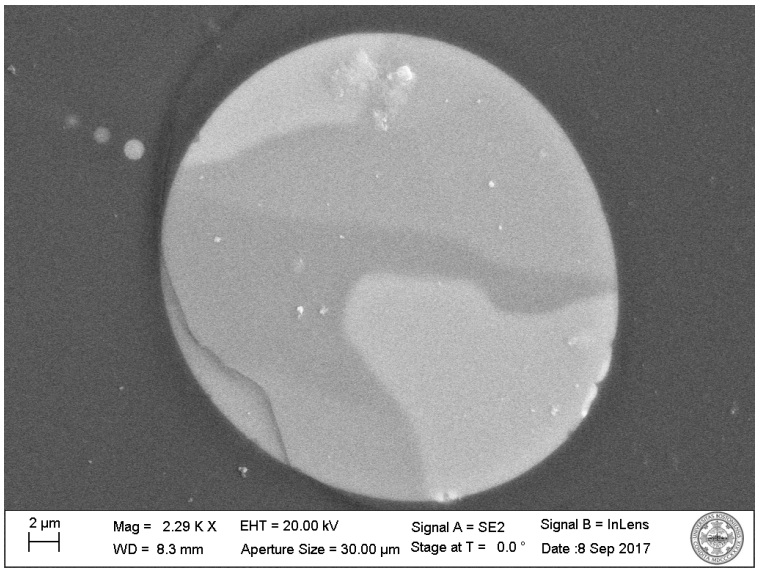

Figure 5·7: Annealed fiber with heating recipe 2 for annealing with rapid cooling rate. Improvement on the elemental distribution is apparent.

Table 5.3: Heating recipe for annealing with slow cooling rate.

Step	Action	Temperature(s) (°C)	Rate (°C/min)	Time (min)
1	Heating	R.T. → 1430	8	178
2	Dwelling	1430	NA	12
3	Cooling	1430 → 1300	1	130
4	Dwelling	1300	NA	12
3	Cooling	1300 → 1000	5	60
5	Cooling	1000 → R.T.	Free-cooling	NA

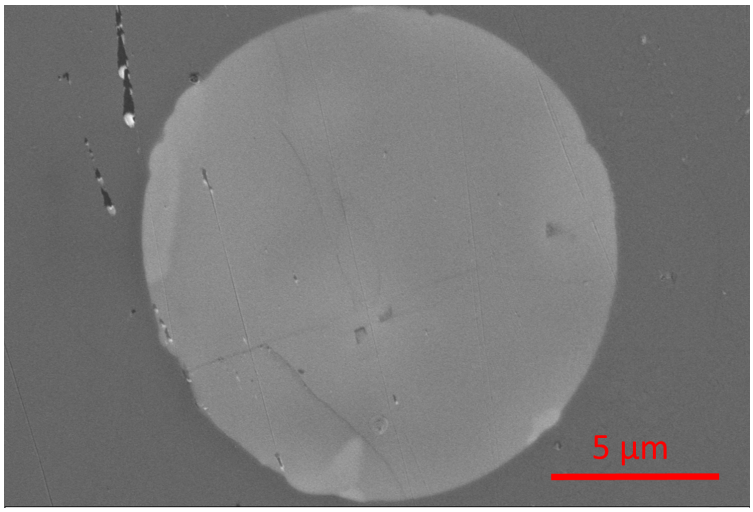

Figure 5·8: Scanning electron micrograph of the fiber cross-section annealed with slow cooling rate.

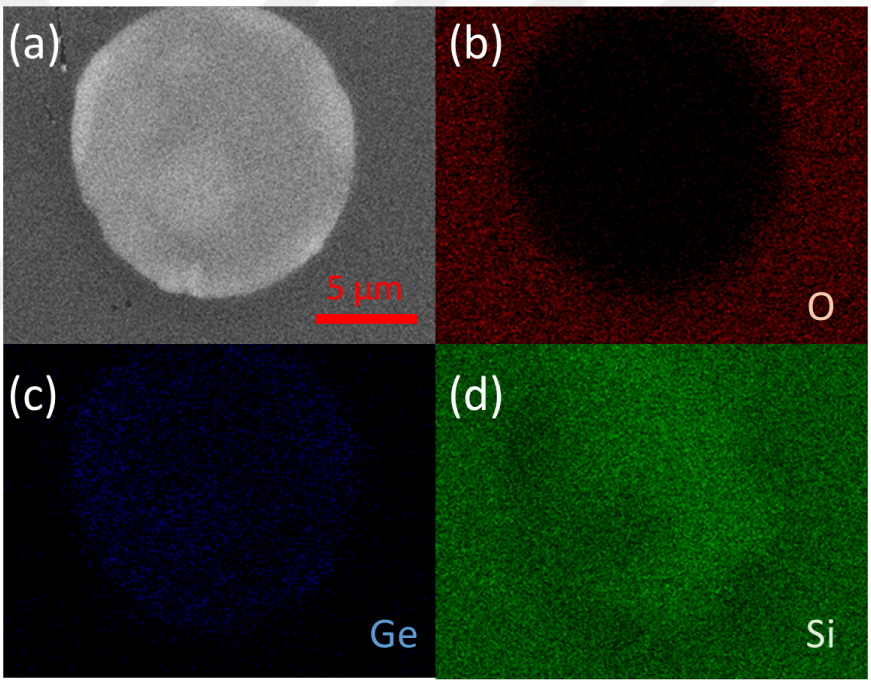

Figure 5·9: (a) SEM Image of the annealed fiber core and SEM-EDX elemental dot maps of (b) O, (c) Ge and (d) Si. Improved elemental distribution can be seen.

Table 5.4: Heating recipe for annealing with multi-step cooling rates.

Step	Action	Temperature(s) (°C)	Rate (°C/min)	Time (min)
1	Heating	R.T. → 1465	8	142
2	Dwelling	1465	NA	6
3	Cooling	1465 → 1350	15	8
2	Dwelling	1350	NA	6
5	Cooling	1350 → 900	2	225
6	Cooling	900 → R.T.	Free-cooling	∼200

5.5.3 Annealing with Multi-step Cooling Rates

Relatively rapid cooling rates with the directional temperature gradient within the core are necessary to form the GRIN structure. Previous attempts did not form either the GRIN or step-index structures. Recipes with multi-step cooling rates and dwellings were designed in order to improve the elemental distribution of the SiGe alloy-cores.

Table 5.4 shows the newly designed annealing experiment with multi-step cooling rates. A fiber was heated to 1465°C and dwelt for 6 minutes. The temperature was then decreased to 1350°C with 15°C/min and dwelt for 6 more minutes. Later it was cooled to 900° with 2°C/min. Finally the furnace was free-cooled to room temperature.

Figure 5·10 shows the SEM and SEM-based EDX studies on the cross-section of the annealed fiber. Fiber core has homogeneous distribution of Si and Ge, proving the positive effect of the recipe with multi-step cooling rates. Uniformity is desirable since the compositional differences cause increment in Rayleigh losses.

5.5.4 Physical Limitations for GRIN Fiber Drawing

In order to form the GRIN structure, fiber core needs to be cooled with controlled rates and the cooling should be directional i.e. it should start from the outer core and should end inner core. However the size of the fiber core is too small to have temper-

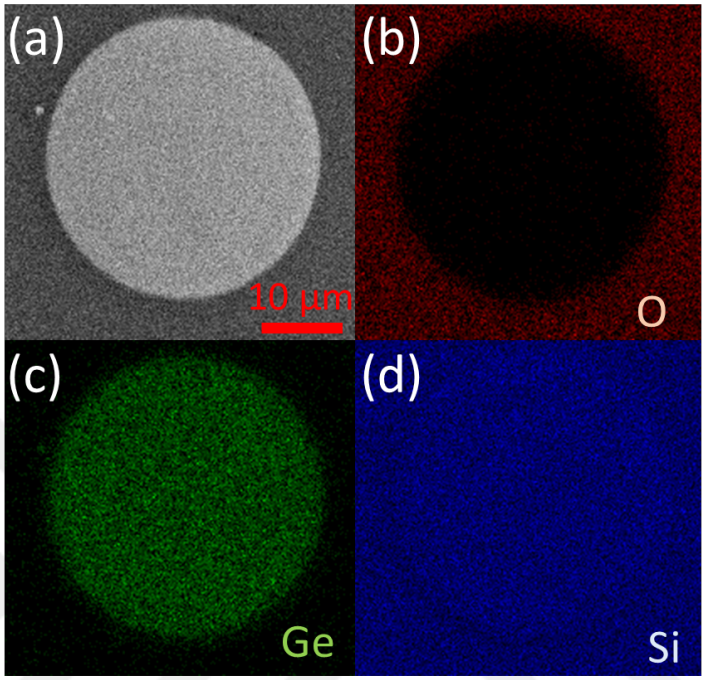

Figure 5·10: (a) Electron micrograph of the fiber core annealed with multi-step cooling rates. Elemental dot mapping of (b) O, (c) Ge and (d) Si show the homogeneity of the alloy-core.

ature gradient across of it, leading to formation of random nucleation points. These points either solidifies spontaneously in equilibrium or in non-equilibrium, preventing elemental gradient through the core.

Bigger samples might form the GRIN structures due to the higher probability of radial temperature gradient. For instance a SiGe alloy lens could be fabricated by controlling the cooling rate. A lens with Si-rich center and Ge-rich edges can be used as a GRIN lenses to prevent chromatic aberration.

5.5.5 Transmission Loss Measurement of the Homogeneous SiGe Fiber

Optical characterization of the homogeneous SiGe alloy-core step-index fibers was performed with the same QCL. Due to the fluctuation of the transmission for each fiber length, the losses were calculated at 6.1 μm where the transmission is consistent

through the all lengths. Transmission losses were calculated using three sets of fiber length, 7.90 mm, 6.60 mm and 5.42 mm, leading to three sets of transmission data for 6.1 μm. Fiber was polished in order to shorten it the latter measured lengths. Each data was compared to the background signal, that is the output signal without any sample through the path of the laser. The transmission losses were found 28 dB/ cm at 6.1 μm. Although significant improvement on lowering the transmission losses was achieved by the annealing, the losses are still much higher than the Ge-core or Si-core fibers that were characterized in this study.

5.5.6 Devitrification of Silica

28 dB/cm loss is still high comparing to the state of the art SiGe alloy-core fibers. The reason behind the high losses could be various. One of them could be related to the cracks that are occurred after the post-drawing annealing processes. Increased time of dwelling in higher temperatures, accelerates the devitrification of silica. Silica devitrifies rapidly especially long dwelling time at the temperatures above 1100°C. Devitrified silica glasses are fragile to mechanical effects, and easily forms cracks. Figure 5·8 shows the cracks occurred in the silica. These cracks may penetrate into the SiGe alloy-core and may cause damage. The cracks in the core of the fiber is shown in Fig. 5·11 could be related to the devitrification of silica.

5.6 Comparison of the Losses

Transmission losses of Ge-core, Si-core and SiGe alloy-core fibers are compared in Table 5.5 with the core diameters. Among the drawn fibers, Ge-core borosilicate-cladded fibers have the lowest transmission losses at the given wavelength.

The losses of the fibers are comparable with the state of art fibers. Ge-core borosilicate-cladded fiber has the only transmission losses up to date. Si-core and SiGe alloy-core fibers have higher losses comparing the state of art fibers. This could

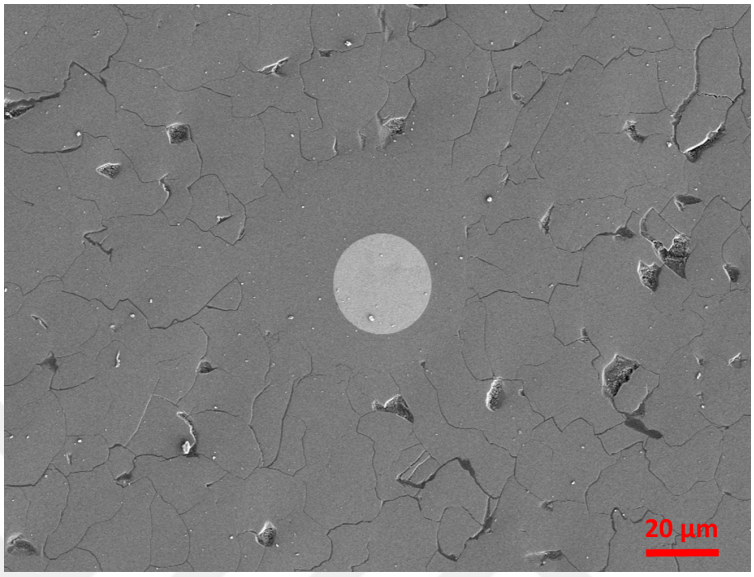

Figure 5·11: Cracks on the glass cladding of the annealed fiber. Devitrification has detrimental effect to the fiber.

Table 5.5: Comparison of the Losses.

Fiber type	Core ⌀ (μm)	Loss (dB/cm)	Wavelength (μm)
Ge	40	4.6	6.1
Si	60	11.6	6.1
SiGe	35	28	6.1

be due to several reasons. Firstly, the EBSD study shows that Ge-core fibers are polycrystalline with the grain size of ∼250μm. This could be same for the Si-core and SiGe alloy-core fibers. Secondly, lower drawing temperature of Si-core and SiGe alloy-core fibers decreases the diffusion from cladding to the core but it also slows down the fiber drawing speed due to the increase of the viscosity. This may cause irregularity in fiber diameters and surface roughness between core and cladding which increase the losses. Lastly, the devitrification of the silica cladding of SiGe alloy-core fibers forms cracks across the core resulting the increase in the transmission losses.

Exploration of post-drawing processes could improve the transmission properties of these semiconductor fibers.

5.7 Discussion on the Cladding Material

Cladding of a fiber is as important as the core, light transmission is achieved by both core and cladding where the evanescent field of the light travels through the cladding. An ideal cladding should possess the following properties:

- Glassy behavior: In order to draw fibers by utilizing the rod-in-tube method, glassy behavior for the cladding materials is necessary. The cladding should soften at certain temperature range and can be shaped accordingly. Crystalline materials such as metals and semiconductors liquefy at the melting points. They can not maintain a certain shape, in this case fiber. Therefore glassy behavior is required for cladding glasses to guide and shape the core material into fiber form.

- Transparency at IR: Electric field of the guided modes have distribution through the core and cladding. Most of the field is confined into the core but a small portion, called evanescent field, is formed in the cladding. Even though the evanescent field exponentially decays in the cladding and diminishes, it is necessary to form successful guidance of the light in the core. If the cladding glass is opaque to the wavelength of the input light, the evanescent field will be absorbed. According to the solution of the governing equations of the light transmission into a fiber medium, the electric field redistributes its intensity between core and cladding. This absorption and redistribution cycle results in high transmission losses. If there is a cladding glass which can transmit the wavelength region of interest, the evanescent field will not face rapid absorption and will be maintained for longer distances, resulting improvement in transmission.

- Lower softening point: Silica is the most common cladding materials for fiber

drawing. It was used as cladding for Ge, Si, SiGe etc. But most of the semiconductors have much lower melting temperatures than the softening point of silica. This keeps the semiconductors molten in the cladding long time periods before the drawing, resulting increase in diffusion from cladding to the core due to the exponential relation between diffusion coefficient and temperature. Thus the cladding glass should have softening temperature close to the melting temperature of semiconductor core. This will decrease the diffusion by keeping the core material less time in molten state.

When combining the above criteria, the cladding should be IR transmitting glass with the tailored softening point to the targeted semiconductor core. Other than these main criteria there are also some additional effects that limit the performance of an IR fiber. CTE match is one such parameter, preventing cracks in the core during the cooling period of fiber drawing [Morris et al., 2012a]. Further chemical reactions between core and cladding may create desirable fiber structures [Hou et al., 2015] or prevent. One such example would be the reaction between CaF_2 and SiO_2. CaF_2 is a known IR material which is used to create commercial IR components such as lenses and windows due to the wide transmission window in the visible, near-IR and mid-IR. CaF_2-core fibers would have low transmission losses for wide range transmission. But these two components react at elevated temperature and form poisonous SiF_4 gas, which is detrimental to living organisms.

Figure 5·12 shows viscosity of three types of glasses. Here Borosilicate glass is suitable for Ge fiber drawing. The softening point of Vycor glass has approximately 100°C lower than Silica. Although the softening point is higher than the desired drawing temperature of Si-core fibers, i.e. 1450-1500°C, the difference in the softening points helps lowering the drawing temperature. However the production of Vycor glasses stopped recently and Vycor glasses are no longer available.

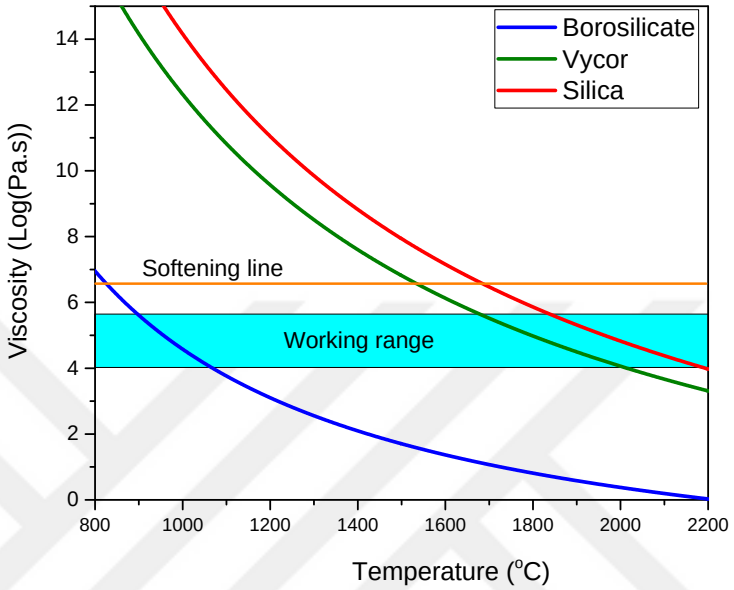

Figure 5·12: Viscosity of three different glasses. Softening line shows the softening point of glasses ($10^{6.6}$Pa.s). Viscosity of working range differs between $10^4 - 10^{5.5}$Pa.s.

Even though there is not any available material for fiber claddings that meets the above criteria, the research could focus on cladding material development in favor of improving the mid-IR fibers. Future works may create suitable cladding materials for each semiconductor materials.

Chapter 6

Femtosecond Mid-IR Pump-Probe Spectroscopy on Semiconductor Fibers

6.1 Detunning Oscillation

Detuning oscillations are a striking phenomenon first reported by Ziegler and collaborators [Zhou et al., 1999, Gardecki et al., 2000] in the frequency-dispersed optical heterodyne nonlinear response in organic liquids with ∼35 fs laser pulses centered near 600 nm. In a related but different context, self-frequency detuning effects have been reported with visible lasers in phase-conjugate mirrors systems with counter propagating beams and ring oscillators based on photorefractive crystals originating from self-induced grating dynamincs [Fischer, 1986]. Here we report in four-wave mixing experiments on Germanium fiber segments in pump-probe geometry on the first 90 fs Gaussian mid-infrared laser pulses centered at a carrier frequency of 2100 cm^{-1}. Ziegler oscillations are observed in two-dimensional spectrograms when the signal wave is dispersed in frequency at varying delay intervals between the pump and probe pulse (Fig. 6·1). The oscillations occur at the detuning frequency of the detected frequency from the probe carrier frequency. In transparent materials, the oscillations do not correspond to molecular electronic or vibrational levels. Rather, they arise the off-resonance electronic response in nonlinear optical materials [Gardecki et al., 2000], and appear in frequency-dispersed optical heterodyne detection. The observation of the oscillations is a signature of a general χ^3 process associated with the third-order

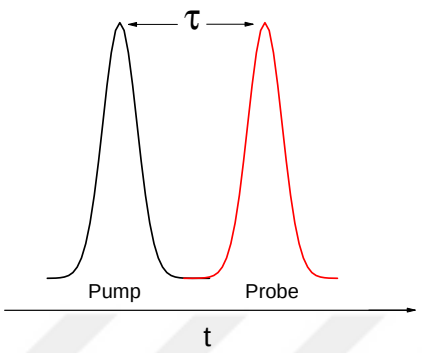

Figure 6·1: Time delay between the pump and the probe pulses.

polarization $P^{(3)}$ response in a transparent material far from resonance. No particular requirement of lattice symmetry is needed, in contrast to frequency doubling, or parametric down-conversion processes, and the oscillations can be observed even amorphous materials, liquids, and in centrosymmetric materials like Ge or Si in the mid-infrared as shown here.

Femtosecond four-wave mixing experiments arising from third-order nonlinear processes have spun off a rich set of multidimensional spectroscopic techniques in nonlinear optics16. These include photon echo [Boyd, 2003], third harmonic generation, transient grating, various forms of Raman spectroscopies, and 2D infrared spectroscopy [Hamm and Zanni, 2011]. Four-wave mixing begins with three incoming electric fields $E_1(r,t)$, $E_2(r,t)$, $E_3(r,t)$. The interaction of the incoming modes in the nonlinear medium generates a nonlinear polarization field $P(r,t)$ that acts as a source for a signal electric field $E_s(r,t)$. The signal is measured in heterodyne detection, where the signal field is superposed with a local oscillator field, E_{LO}. The detected intensity is proportional to $|E_s + E_{LO}|^2$ generating in the detected heterodyne signal intensity $S = \frac{\zeta}{2Z_0} Re(E_s^* E_L O)$ that is linearly proportional to the polarization field. The proportionality constant includes a geometric experimental factor ζ derived from

the constant transfer function between the exit face of the fiber and detector element, and Z_0 is the free space impedance. Importantly, the phase-sensitive technique allows for determination of both the amplitude and phase of the polarization field. When the incoming waves are ultrafast, with temporal widths in the femtosecond scale, four-wave mixing experiments yield a rich superposition of the Fourier component modes as described later in this paper. In the pump-probe geometry used in our experiments the electric field from the probe pulse serves as its own local oscillator and the analysis is particularly straightforward.

A linearly polarized monochromatic wave traveling parallel to the z-axis corresponding to a particular Fourier component is described by an electric field $E_\omega(\omega, z)$ averaged over transverse coordinates [Mamyshev and Chernikov, 1990]. Considering the ultrafast laser pulse as a superposition of monochromatic waves propagating in the z direction, the electric field averaged over a transverse coordinate is given by [Mamyshev and Chernikov, 1990]

$$\frac{\partial E_\omega(\omega,z)}{\partial z} = \frac{i2\pi\omega}{cn_{eff}(\omega)} \int d\omega' \int d\omega'' \Big[G(\omega,\omega',\omega'') E_\omega(\omega',z) E_\omega(\omega'',z) \\ E^*_\omega(\omega'+\omega''-\omega,z) \chi^{(3)}(\omega-\omega') \Delta k z) \Big] \tag{6.1}$$

Equation 6.1 is the starting point for the textbook time-domain description where the propagation of light in nonlinear fiber optics is described by the nonlinear Schrodinger equation. In the time domain, For a particular state of linear polarization, the third order response the electric field is given in a frame of reference set by the carrier wave by [Mamyshev and Chernikov, 1990, Agrawal, 2007]

$$\frac{\partial E(z,t)}{\partial z} = -\frac{\alpha(\omega)}{2}E + i\sum_{m\geq 2}\frac{i^m\beta_m}{m!}\frac{\partial^m E}{\partial t^m} + i\gamma\Big(1+\frac{i}{\omega_0}\frac{\partial}{\partial t}\Big) \Big[E(z,t)\int_{-\infty}^{+\infty} R(t')E(z,t-t')^2/dt'\Big] \tag{6.2}$$

The first term in Eq. 6.2 accounts for absorption, and higher order dispersion effects are described by the second term. The nonlinear response R(t) is assumed to be strictly local in space and independent of z, but will depend on past history. A detailed analysis for comparison with experiments is challenging. We assume that the response is far from any one-photon absorption, and is primarily due to electronic degrees of freedom in the material. To check that the drawn fiber materials are indeed off-resonance with no sharp vibrational absorption bands, we have performed transmission measurements using a QCL as well as a FTIR microscope as described in experimental section below. No sharp absorption bands were detected. In addition the pump and probe waves are also in a frequency range where two-photon absorption cross-section is also very low, with the 2-photon energy still well below the bandgap of Ge. We also assume that the local field approximation holds in the Ge fiber core and there are no long range correlations in the dielectric, in contrast for example to plasmonic metamaterial or photonic bandgap systems where there are spatial structures comparable to the scale of the wavelengths. Simplification of the analysis is also facilitated by using data from experiments performed with short sample lengths where we neglect higher order dispersion. Under these assumptions, Eq. 6.1 can then be readily integrated over z for each Fourier component, and the electric field at the end of the fiber of length of length L is then described in terms of an effective loss coefficient α_{eff} that is independent of the frequency over the narrow detuning range. The electric field amplitude then decays as $\sim E_{sZ}(t)e^{-\alpha_{eff}L/2}$ with the electric field

$E_{sZ}(t)$ now described using the third order nonlinear response formalism described by Ziegler and co-workers that is described next. In the first theoretical analysis, the signal for detuning oscillations was derived in the Rotating Wave Approximation (RWA). To check against a potential inconsistency in adapting RWA to off-resonant nonlinear response, which is essentially instantaneous, off-resonant response is derived using the full four-wave mixing treatment. The susceptibility off resonance is described by qualitatively, the results are very close both to the observed experimental responses and to the results from the RWA approximation. The experiments measure the dispersed infrared signal that is the difference between the pump on vs pump off as described in the experimental section. This difference signal can be positive or negative depending on the time delay and the detuning frequency. Following Gardecki et al, the detected signal spectrograms are given by the following analytical expression that is symmetric with respect to the detuning Δ_D and the time delay t between the pump and probe pulses, and can be used to compare with the experimental data:

$$S(\Delta_D, t) = S_o e^{\alpha_{eff} L} exp(-t^2/\tau_0^2) exp(-\Delta_D^2/\Delta_0^2) cos(f\Delta_D t + \phi) \tag{6.3}$$

Equation 6.3 is the central phenomenological result used to describe detuning oscillations. For a thin bulk transparent sample and transform limited identical Gaussian pulses, the parameters τ_0, Δ_D, f in Eq. 6.3 are related given by $\tau_0 \Delta_D = \frac{9}{2}, \frac{2}{3}$. For a thin sample, the phase shift ϕ is 0 or $\frac{\pi}{2}$ for dichroism and birefringence. For a fiber sample, the phase shift will be different, and appears in a shift of the apparent zero time delay point without affecting other parameters. The form and relations depend on the shape of the pulses as shown in Gardecki et al14. For the fiber sample, with our laser pulses close to but not at the transform limit, although the parameters can in principle be calculated using microscopic model, they were varied independently

to fit the data and to compare with the ideal values. Figure 6·5 shows a simulation that matches the observed periodicities in the detuning frequency as well the time delay. Equation 6.3 not only captures the essential symmetry between the detuning $\Delta_D$and the time delay t that is observed experimentally, but also the apparent time-reversal invariance between positive and negative time delays. This latter symmetry arises from the fundamental physical principle that when pump and probe beams overlap, the uncertainty principle and the indistinguishability of photons ensure that it is impossible to distinguish pump from probe beams. As is well known, a signal is observed even at negative time delays without of course violating causality.

6.2 SEM-EDX Results

Pump-Probe Spectroscopy was performed on four different samples. A Ge-core borosilcate glass-cladded fiber with 132 μm core (Fig. 6·2), two Ge-core borosilicate glass-cladded canes with 358 μm and 770 μm cores respectively, and a unprocessed Ge-rod with 3 mm diameter. Fiber and canes were drawn with the same method and same batch as the Ge-core fiber in the transmission loss measurement.

Figure 6·3(a) shows a scanning electron micrograph of a finely polished cross-section of Ge fiber with 132 μm core diameter and 466 μm cladding diameter (SEM; Zeiss Supra 55, Germany). The elemental composition profile across the core/cladding interface was obtained by the SEM and energy dispersive x-ray spectroscopy (EDX; EDAX, NJ). The EDX elemental dot maps of Ge, Si and O are shown in Fig. 6·3(b)-(d). Figure 6·3(e) shows an EDX line scan through the core and cladding of the fiber marked by the orange line on the inset image, clearly indicating that the diffusion of oxygen and silicon from cladding to core is minimal. The low oxygen content of the core is likely due to the low processing temperature during the fiber drawing. This is encouraging for the mid-IR transmission through the fiber for pump-probe

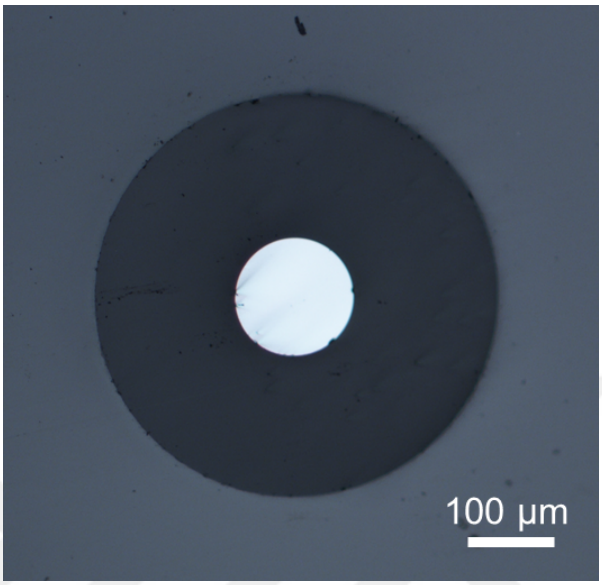

Figure 6·2: Optical micrograph of a finely polished Ge-fiber that is used for Pump-Probe Spectroscopy measurement.

spectroscopy since the oxygen is known to absorb mid-IR light.

6.3 XRD Results

Crystalline structure of Ge-core fiber were examined by x-ray diffraction spectroscopy. RSM of fibers cross-section was plotted with a 1 mm diameter x-ray beam, using 2D detector. Figure 6·4 (b) indicates that Ge core has single (220) peak orientation.

6.4 Pump-Probe Spectroscopy on Ge samples

Figure 6·6 and 6·7 shows the experimental results from four different sets of samples. Figure 6·6(a)-(d) are surface plot with the colorized spectrogram signals as a function of time delay and dispersed frequency for four different samples ranging from a Ge fiber with 132 m-core diameter to the starting unprocessed Ge 3 mm diameter rod. Fig. 6·7(a)-(d) represent the corresponding data along a line cut at a selected

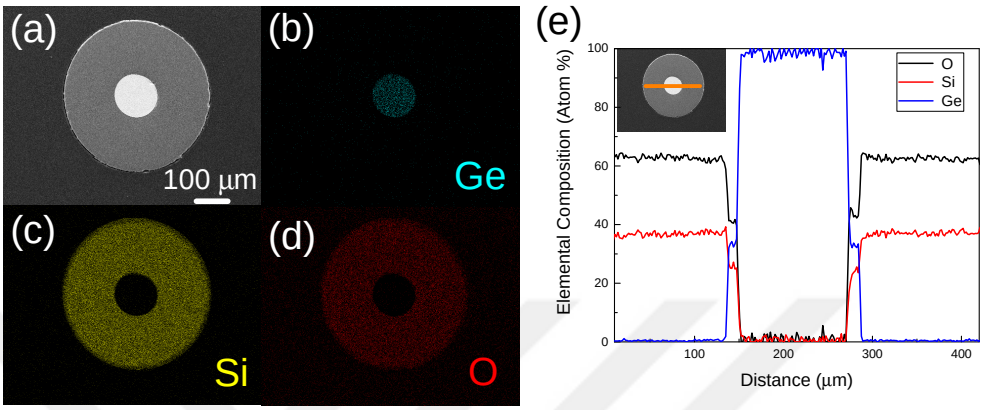

Figure 6·3: (a) Electron micrograph of the Ge-core fibers that was used for the Pump-Probe spectroscopy. EDX Elemental dot mapping of fiber (b) Ge, (c) Si and (d) is O. (e) show EDX line scan through the fiber cross-section that are show in the inset.

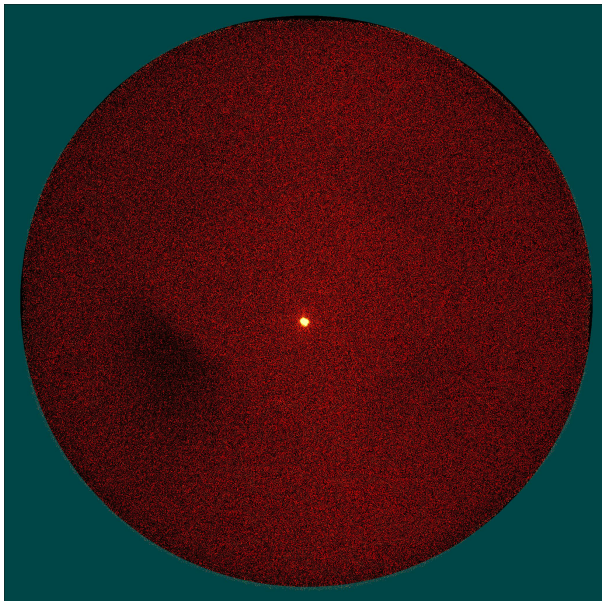

Figure 6·4: 2D scan of Ge-core fiber. Fiber has the (220) single crystal orientation.

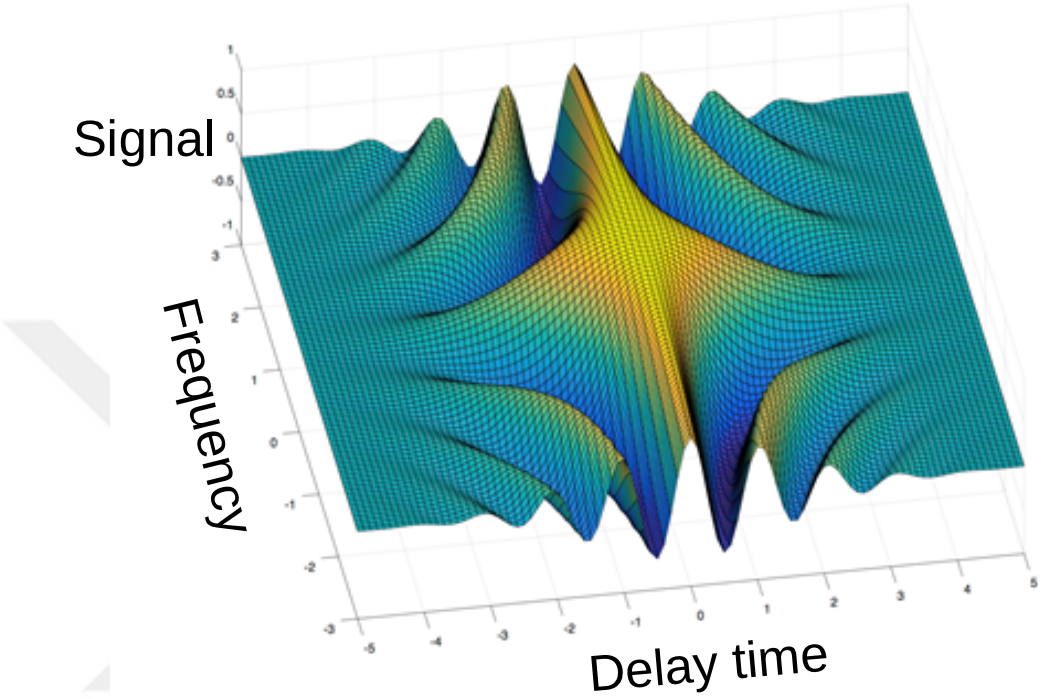

Figure 6·5: Simulation of detunning oscillation.

frequency of 2214 cm^{-1} and shows the oscillations in the time domain that result from four-wave mixing. Figure 6·7 shows also time traces at selected detuning frequencies. The period decreases with increasing detuning, as expected from Eq. 6.3.

Each of the time traces in Fig. 6·7 can be used to measure the period T of the dominant mode of oscillation as a function of detuning frequency Δ_D. Figure 6·5 shows a plot of the period for all the samples which is expected to a constant in the Ziegler model. The ratio of the parameters obtained from individual traces and global fitting are $u_0 = 2164.25 \pm 13.2, f = 31.52 \pm 0.47$ consistent with the Ziegler model. Figure 6·8 shows time traces at selected detuning frequencies. The period decreases with increasing detuning, as expected from Eq. 6.3.

The salient features of the experimental results and detuning oscillations can only arise from nonlinear effects in the Ge material in the fiber. Nonlinear properties

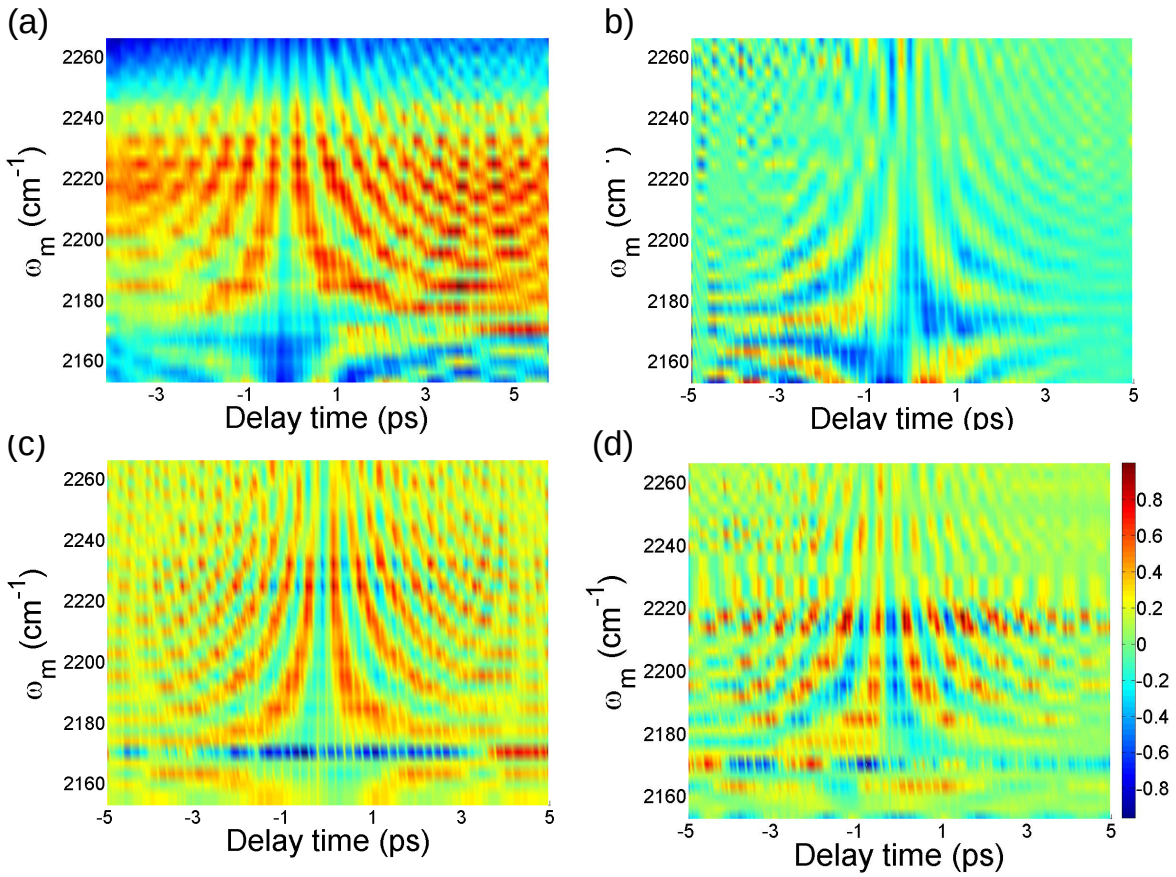

Figure 6·6: Experimental results on four different samples: unprocessed Ge rod with 3 mm diameter, Ge cane with 770 μm-core diameter, Ge cane with 358 μm-core diameter and Ge fiber with 132 μm-core diameter. (a), (b), (c) and (d) are contour plots of samples with respect to delay time (ps) and wavenumber (cm^{-1}). Each figures are individual from each other but have the same color code. Red indicates maximum normalized intensity whereas blue represents minimum normalized intensity.

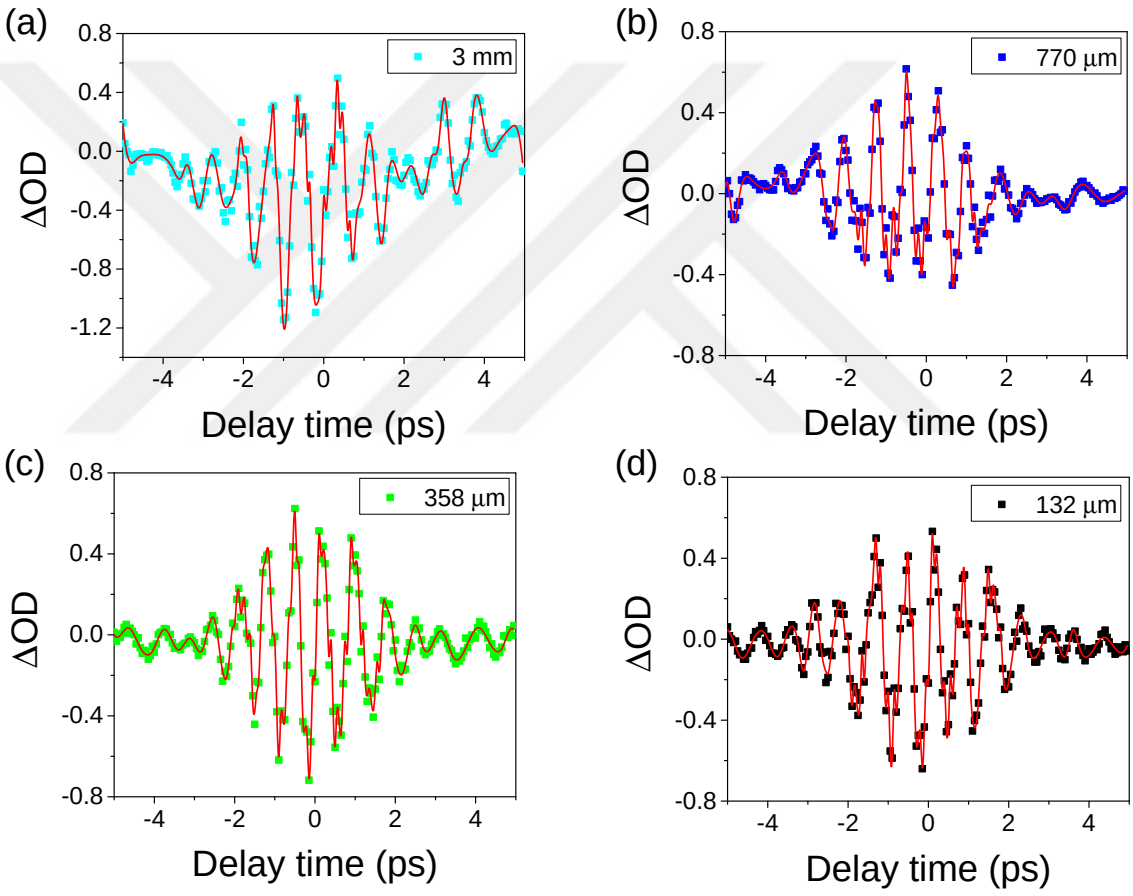

Figure 6·7: Population decay of each sample with respect to delay time and optical delay difference at 2214 cm^{-1}.

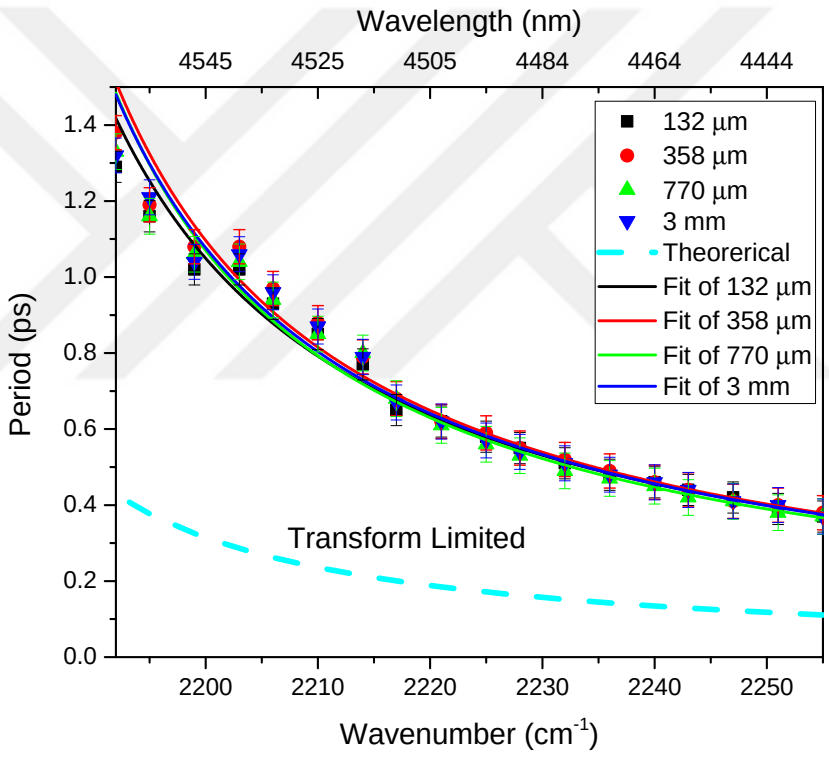

Figure 6·8: Oscillation period of four different samples at selected detuning frequencies.

of Ge are maintained even after processing to form a fiber. Detuning oscillations are the signature of nonlinear response, observed in Ge fibers in the mid-infrared region for the first time. As the history of fiber optics demonstrates, with improved materials processing, and refinement with different cladding and coating materials, losses may be expected to reduce. Demonstration of nonlinear effects can be expected to have new applications in the mid-infrared region, such as optical switching, optical modulation and frequency generation.

Chapter 7

Conclusions

In this dissertation work, we have fabricated and have characterized semiconductor-core glass-cladded optical fibers for mid-IR applications. Fibers were drawn with laboratory made draw towers and microstructural and optical characterizations were performed. Here we summarized our results and discuss the possible future work.

In chapter 3, we explained our work on Ge-based fibers. We drew Ge-core borosilicate glass-cladded fibers in house at relatively low temperature around 1000°C. Later fibers were embedded in epoxy and polished finely for characterization purposes. Fibers were examined with S/TEM and S/TEM based EDX and found that the impurity diffusion into the core region stops in less than 100 nm away from the core-cladding interface. Further the crystallinity of the fibers were investigated both HRTEM and XRD. Single crystal orientation of Ge-core and amorphous orientation of borosilicate cladding were observed. Ge-core fibers have single (111) peak orientation, confirming that the scanned region have single crystal structure. EBSD results identified the grain size as 250 μm. Therefore fibers have polycrystalline nature with the same orientation. Optical characterization of Ge canes were performed with FTIR, showing the similar transmission characteristic of cane and bulk Ge. Transmission loss measurements were completed with a quantum cascade source and 5.1 dB/cm average losses were found in the range of 5.82-6.28μm. Up to date, this is the lowest transmission losses for Ge-core borosilicate-cladded fibers and only loss data of Ge-core fibers for this wavelength region.

Chapter 4 gave the results of our Si-core silica-cladded fibers. These fibers were drawn at 1760°C. SEM and SEM based EDX were utilized for microstructural characterization. Fiber core has 3% oxygen content that occurred at the elevated temperature of drawing. This value is still much lower comparing to the similar work. The lower value is possibly lower drawing temperature comparing to conventional drawing temperature of silica based fibers. Crystalline nature of the fiber was analyzed with XRD and found single two (100) and (111) orientations in the fiber core. Further optical characterization was conducted with the QCL in the spectrum of 5.82-6.22 μm and found 12.5 dB/cm average loss, that is the only transmission losses in this range for Si based fibers. However the polycrstalline nature and possible cracks in the core due to the low drawing temperature might be the reasons behind the higher losses.

Silicon and germanium alloy core fibers were studied in chapter 5. These fibers have unique structure and could produce tailored properties of both materials. Further with the right cooling rate, graded-index structure can be created. Similar to the Si-core fibers, we drew them at 1760°C. Drawn fibers have compositional differences among the core region due to the multiple nucleation centers occurred during the solidification. Optical transmission losses were foung 75 dB/cm at 6.1 μm. Fibers went though post-drawing annealing in order to improve the elemental distribution of core region. Core had homogeneous elemental distribution after annealing the fiber between the liquidus and solidus points for finite amount of time. Transmission losses were improved to 28 dB/cm at 6.1 μm. Unfortunately graded-index structure could not be created due to the constraints of solidification problem.

Further the nonlinear properties of Ge fibers were investigated in chapter 6. Femtosecond pump-probe spectroscopy was applied to processed and unprocessed Ge samples leading to observation of detuning oscillation. Detuning oscillations were

observed in fiber samples as well as bulk Ge rod, showing that Ge preserves its nonlinearity after the drawing. Exploration of the nonlinear optic in Ge media is important to gather attention to Ge-based products.

As a conclusion, we investigated different types of semiconductor-core, glass-cladded fibers including Ge-core borosilicate glass-cladded fibers, Si-core silica-cladded fibers and SiGe alloy-core silica-cladded fibers. In future, mid-IR fibers will play important roles in many field, and will improve our daily life as well as scientific discoveries. As of now, they can be used for chemical detection of environmentally hazardous green house gases, bio-terror agents, remote laser delivery for medical surgeries and missile protection for countermeasure defense systems. Improvements of mechanical and optical properties of mid-IR fibers improves the applicability of these fibers to our daily life. Furthermore, graded-index mid-IR fibers have potential to decrease the transmission losses significantly which will accelerate the usage of these fibers. The continuous efforts on coping with the today's limitations on the graded-index fibers, will eventually make them available for future technology.

Appendix A

Identifying the Source of Losses

In order to decrease the transmission losses in the Ge fiber, it is important to identify the source of losses. The losses can be causes by three regions: Core, interface and cladding. The total transmission loss in a fiber can be expressed as

$$L_{total} = L_{core} + L_{clad} + L_{inter} \tag{A.1}$$

where L_{core}, L_{clad} and L_{inter} are losses in the core, cladding, and interface, respectively. Each type of loss can be related to the power, P, transmitted through that region, and the loss coefficient, α, associated with that region, giving

$$\begin{aligned} L_{core} &= P_{core}\alpha_{core} \\ L_{clad} &= P_{clad}\alpha_{clad} \\ L_{inter} &= P_{inter}\alpha_{inter} \end{aligned} \tag{A.2}$$

Assuming that the axis of fiber and input beam are well aligned, leading to the excitation of LP_{0m} modes only, the power transmitted through each region of the

fiber can be defined as

$$\begin{aligned} P_{core} &= \sum_m P_{0m}\eta_{0m,core} \\ P_{clad} &= \sum_m P_{0m}\eta_{0m,clad} \\ P_{inter} &= \sum_m P_{0m}\eta_{0m,inter} \end{aligned} \tag{A.3}$$

where, P_{0m} is power of the guided LP_{0m} modes, and $\eta_{0m,core}$, $\eta_{0m,clad}$, and $\eta_{0m,inter}$ are the excitation coefficient of core, cladding, and interface, respectively. These excitation coefficients can be found analytically. In the fiber, shown in Fig. 3·3, calculations show that modes up to LP_025 can be guided (Fig. A·1).

Using Eqs. A.3, the output power, P_{out}, can be related to the input power, P_{in}, as

$$\begin{aligned} \Bigg[P_{in}0.64 - P_{radiation} - \sum_m P_{0m}\eta_{0m,core}\alpha_{core} - \sum_m P_{0m}\eta_{0m,clad}\alpha_{clad} \\ - \sum_m P_{0m}\eta_{0m,inter}\alpha_{inter}\Bigg]0.64 = P_{out} \end{aligned} \tag{A.4}$$

where $P_{radiation}$ is the power that is dissipated through the radiation modes. Cladding modes represent the modes above LP_{025} which is the highest order guided mode in this fiber. Modes over LP_{026} modes cannot be guided in the fiber and they form the radiation modes. The factor of 0.64 reflects power loss due to Fresnel reflection between air and the germanium core surface, both at the input and output of the fiber.

Using this model, we aim to differentiate the source of losses by calculating α for each region of the fiber. By adjusting the distance between the input lens and input facet of the fiber, different beam sizes can be input into the fiber which excite modes with different excitation coefficients. The results of one such calculation is shown in Fig. A·1. The loss data at three different beam sizes will give us the values of the

three loss coefficients in Eq. A.2.

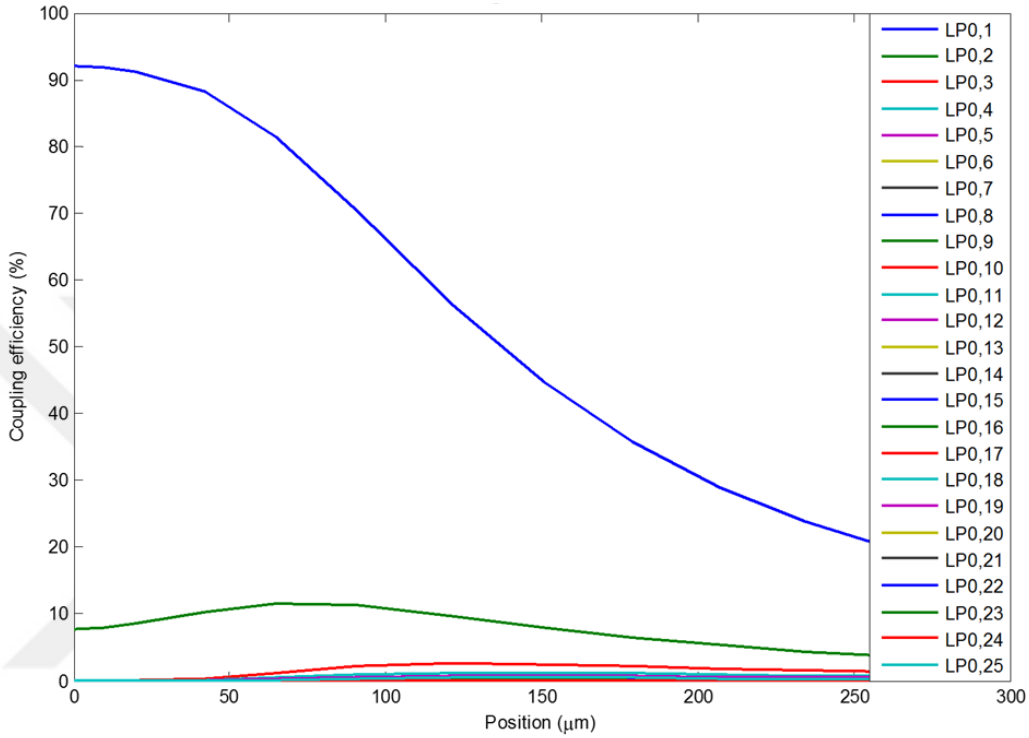

Figure A·1: Calculated coupling efficiency for the first 25 0m modes versus distance from the focal plane of the input lens of the QCL at 1640 $cm^{-}1$.

References

[Agrawal, 2007] Agrawal, G. P. (2007). *Nonlinear fiber optics*. Academic press.

[Askeland and Phulé, 2006] Askeland, D. R. and Phulé, P. P. (2006). *The science and engineering of materials*. Springer.

[Ballato et al., 2010] Ballato, J., Hawkins, T., Foy, P., McMillen, C., Burka, L., Reppert, J., Podila, R., Rao, A., and Rice, R. R. (2010). Binary iii-v semiconductor core optical fiber. *Optics express*, 18(5):4972–4979.

[Ballato et al., 2011] Ballato, J., Hawkins, T., Foy, P., Morris, S., Hon, N., Jalali, B., and Rice, R. (2011). Silica-clad crystalline germanium core optical fibers. *Optics Letters*, 36(5):687–688.

[Ballato et al., 2008] Ballato, J., Hawkins, T., Foy, P., Stolen, R., Kokuoz, B., Ellison, M., McMillen, C., Reppert, J., Rao, A., Daw, M., et al. (2008). Silicon optical fiber. *Optics express*, 16(23):18675–18683.

[Ballato et al., 2009] Ballato, J., Hawkins, T., Foy, P., Yazgan-Kokuoz, B., Stolen, R., McMillen, C., Hon, N., Jalali, B., and Rice, R. (2009). Glass-clad single-crystal germanium optical fiber. *Optics express*, 17(10):8029–8035.

[Ballato and Snitzer, 1995] Ballato, J. and Snitzer, E. (1995). Fabrication of fibers with high rare-earth concentrations for faraday isolator applications. *Applied optics*, 34(30):6848–6854.

[Bei et al., 2013] Bei, J., Monro, T. M., Hemming, A., and Ebendorff-Heidepriem, H. (2013). Fabrication of extruded fluoroindate optical fibers. *Optical Materials Express*, 3(3):318–328.

[Boyd, 2003] Boyd, R. W. (2003). *Nonlinear optics*. Academic press.

[Carletti et al., 2015] Carletti, L., Ma, P., Yu, Y., Luther-Davies, B., Hudson, D., Monat, C., Orobtchouk, R., Madden, S., Moss, D., Brun, M., et al. (2015). Nonlinear optical response of low loss silicon germanium waveguides in the mid-infrared. *Optics express*, 23(7):8261–8271.

[Chaudhuri et al., 2017] Chaudhuri, S., Ji, X., Huang, H.-T., Day, T., Gopalan, V., and Badding, J. (2017). Small core sige alloy optical fibers by templated deposition. In *CLEO: Applications and Technology*, pages JW2A–69. Optical Society of America.

[Coucheron et al., 2016] Coucheron, D. A., Fokine, M., Patil, N., Breiby, D. W., Buset, O. T., Healy, N., Peacock, A. C., Hawkins, T., Jones, M., Ballato, J., et al. (2016). Laser recrystallization and inscription of compositional microstructures in crystalline sige-core fibres. *Nature communications*, 7:13265.

[Fetterly, 2008] Fetterly, D. R. (2008). Directed infrared countermeasures (dircm) system and method. US Patent 7,378,626.

[Fischer, 1986] Fischer, B. (1986). Theory of self-frequency detuning of oscillations by wave mixing in photorefractive crystals. *Optics letters*, 11(4):236–238.

[Gardecki et al., 2000] Gardecki, J., Constantine, S., Zhou, Y., and Ziegler, L. (2000). Optical heterodyne detected spectrograms of ultrafast nonresonant electronic responses. *JOSA B*, 17(4):652–662.

[Gibson et al., 2014] Gibson, D., Bayya, S., Sanghera, J., Nguyen, V., Scribner, D., Maksimovic, V., Gill, J., Yi, A., Deegan, J., and Unger, B. (2014). Layered chalcogenide glass structures for ir lenses. In *Proc. SPIE*, volume 9070, page 90702I.

[Hamm and Zanni, 2011] Hamm, P. and Zanni, M. (2011). *Concepts and methods of 2D infrared spectroscopy*. Cambridge University Press.

[Harrington, 2004] Harrington, J. A. (2004). *Infrared fibers and their applications*. SPIE press Bellingham, WA.

[Hayashi et al., 1970] Hayashi, I., Panish, M., Foy, P., and Sumski, S. (1970). Junction lasers which operate continuously at room temperature. *Applied Physics Letters*, 17(3):109–111.

[Hector et al., 1997] Hector, J., Hewak, D., Wang, J., Moore, R., and Brocklesby, W. (1997). Quantum-efficiency measurements in oxygen-containing gallium lanthanum sulphide glasses and fibers doped with pr/sup 3+. *IEEE Photonics Technology Letters*, 9(4):443–445.

[Hou et al., 2015] Hou, C., Jia, X., Wei, L., Tan, S.-C., Zhao, X., Joannopoulos, J. D., and Fink, Y. (2015). Crystalline silicon core fibres from aluminium core preforms. *Nature communications*, 6:6248.

[Ji et al., 2016] Ji, X., Lei, S., Yu, S.-Y., Cheng, H. Y., Liu, W., Poilvert, N., Xiong, Y., Dabo, I., Mohney, S. E., Badding, J. V., et al. (2016). Single-crystal silicon optical fiber by direct laser crystallization. *ACS Photonics*, 4(1):85–92.

[Ji et al., 2017] Ji, X., Page, R. L., Chaudhuri, S., Liu, W., Yu, S.-Y., Mohney, S. E., Badding, J. V., and Gopalan, V. (2017). Single-crystal germanium core optoelectronic fibers. *Advanced Optical Materials*, 5(1).

[Kanamori et al., 1984] Kanamori, T., Terunuma, Y., Takahashi, S., and Miyashita, T. (1984). Chalcogenide glass fibers for mid-infrared transmission. *Journal of lightwave technology*, 2(5):607–613.

[Kapron et al., 1970] Kapron, F., Keck, D., and Maurer, R. (1970). Radiation losses in glass optical waveguides. *Applied Physics Letters*, 17(10):423–425.

[Lagonigro et al., 2010] Lagonigro, L., Healy, N., Sparks, J. R., Baril, N. F., Sazio, P. J., Badding, J. V., and Peacock, A. C. (2010). Low loss silicon fibers for photonics applications. *Applied Physics Letters*, 96(4):041105.

[Lezal et al., 1998] Lezal, D., Pedlikova, J., and Poulain, M. (1998). Sulfide and heavy metal oxide glasses for active fibers. In *Lasers and Materials in Industry and Opto-Contact Workshop*, pages 43–54. International Society for Optics and Photonics.

[Lin, 2001] Lin, J. (2001). Refractive surgery and presbyopia correction using infrared and ultraviolet lasers. US Patent 6,258,082.

[Mamyshev and Chernikov, 1990] Mamyshev, P. and Chernikov, S. V. (1990). Ultrashort-pulse propagation in optical fibers. *Optics letters*, 15(19):1076–1078.

[Mashanovich et al., 2017] Mashanovich, G. Z., Mitchell, C. J., Penades, J. S., Khokhar, A. Z., Littlejohns, C. G., Cao, W., Qu, Z., Stanković, S., Gardes, F. Y., Masaud, T. B., et al. (2017). Germanium mid-infrared photonic devices. *Journal of Lightwave Technology*, 35(4):624–630.

[Mehta et al., 2010a] Mehta, P., Healy, N., Baril, N., Sazio, P., Badding, J., and Peacock, A. (2010a). Nonlinear transmission properties of hydrogenated amorphous silicon core optical fibers. *Optics express*, 18(16):16826–16831.

[Mehta et al., 2010b] Mehta, P., Krishnamurthi, M., Healy, N., Baril, N. F., Sparks, J. R., Sazio, P. J., Gopalan, V., Badding, J. V., and Peacock, A. C. (2010b). Mid-infrared transmission properties of amorphous germanium optical fibers. *Applied Physics Letters*, 97(7):071117.

[Miya et al., 1979] Miya, T., Terunuma, Y., Hosaka, T., and Miyashita, T. (1979). Ultimate low-loss single-mode fibre at 1.55 μm. *Electronics Letters*, 15(4):106–108.

[Morgan et al., 1997] Morgan, S., Furniss, D., Seddon, A., and Moore, M. (1997). Effect of glass purity on the glass stability and physical properties of ga–la–s glasses. *Journal of non-crystalline solids*, 213:72–78.

[Morris et al., 2012a] Morris, S., Hawkins, T., Foy, P., Ballato, J., Martin, S. W., and Rice, R. (2012a). Cladding glass development for semiconductor core optical fibers. *International Journal of Applied Glass Science*, 3(2):144–153.

[Morris et al., 2012b] Morris, S., Hawkins, T., Foy, P., Hudson, J., Zhu, L., Stolen, R., Rice, R., and Ballato, J. (2012b). On loss in silicon core optical fibers. *Optical Materials Express*, 2(11):1511–1519.

[Mossadegh et al., 1998] Mossadegh, R., Sanghera, J., Schaafsma, D., Cole, B., Nguyen, V., Miklos, R., and Aggarwal, I. (1998). Fabrication of single-mode chalcogenide optical fiber. *Journal of Lightwave Technology*, 16(2):214.

[Nordstrand et al., 2013] Nordstrand, E. F., Dibbs, A. N., Eraker, A. J., and Gibson, U. J. (2013). Alkaline oxide interface modifiers for silicon fiber production. *Optical Materials Express*, 3(5):651–657.

[Oh and Paek, 2012] Oh, K. and Paek, U.-C. (2012). *Silica optical fiber technology for devices and components: design, fabrication, and international standards*, volume 240. John Wiley & Sons.

[Ordu et al., 2016] Ordu, M., Guo, J., Erramilli, S., Ramachandran, S., and Basu, S. (2016). Germanium-core borosilicate glass-cladded semiconductor fibers for mid-ir applications. In *CLEO: Science and Innovations*, pages STu4R–1. Optical Society of America.

[Ordu et al., 2017] Ordu, M., Guo, J., Tai, B., Hong, M. K., Erramilli, S., Ramachandran, S., and Basu, S. N. (2017). Mid-infrared transmission through germanium-core borosilicate glass-clad semiconductor fibers. *Optical Materials Express*, 7(9):3107–3115.

[Peacock and Healy, 2016] Peacock, A. C. and Healy, N. (2016). Semiconductor optical fibres for infrared applications: A review. *Semiconductor Science and Technology*, 31(10):103004.

[Romano et al., 1994] Romano, V., Rodriguez, R., Altermatt, H. J., Frenz, M., and Weber, H. P. (1994). Bone microsurgery with ir-lasers: A comparative study of the thermal action at different wavelengths. In *Proc SPIE*, volume 2077, pages 87–97.

[Rothman et al., 2013] Rothman, L. S., Gordon, I. E., Babikov, Y., Barbe, A., Benner, D. C., Bernath, P. F., Birk, M., Bizzocchi, L., Boudon, V., Brown, L. R., et al. (2013). The hitran2012 molecular spectroscopic database. *Journal of Quantitative Spectroscopy and Radiative Transfer*, 130:4–50.

[Sa'Ar et al., 1987] Sa'Ar, A., Barkay, N., Moser, F., Schnitzer, I., Levite, A., and Katzir, A. (1987). Optical and mechanical properties of silver halide fibers. In *OE/Fibers' 87*, pages 98–104. International Society for Optics and Photonics.

[Sanghera and Aggarwal, 1999] Sanghera, J. and Aggarwal, I. (1999). Active and passive chalcogenide glass optical fibers for ir applications: a review. *Journal of Non-Crystalline Solids*, 256:6–16.

[Sanghera et al., 2000] Sanghera, J., Shaw, L., Busse, L., Nguyen, V., Pureza, P., Cole, B., Harrison, B., Aggarwal, I., Mossadegh, R., Kung, F., et al. (2000). Development and infrared applications of chalcogenide glass optical fibers. *Fiber & Integrated Optics*, 19(3):251–274.

[Sazio et al., 2006] Sazio, P. J., Amezcua-Correa, A., Finlayson, C. E., Hayes, J. R., Scheidemantel, T. J., Baril, N. F., Jackson, B. R., Won, D.-J., Zhang, F., Margine, E. R., et al. (2006). Microstructured optical fibers as high-pressure microfluidic reactors. *Science*, 311(5767):1583–1586.

[Schott, 2014] Schott (2014). Duran glass catalog.

[Scott et al., 2009] Scott, B., Wang, K., Caluori, V., and Pickrell, G. (2009). Fabrication of silicon optical fiber. *Optical Engineering*, 48(10):100501–100501.

[Senior and Jamro, 2009] Senior, J. M. and Jamro, M. Y. (2009). *Optical fiber communications: principles and practice*. Pearson Education.

[Simhony et al., 1988] Simhony, S., Schnitzer, I., Katzir, A., and Kosower, E. (1988). Evanescent wave infrared spectroscopy of liquids using silver halide optical fibers. *Journal of applied physics*, 64(7):3732–3734.

[Sing-Kapany, 1967] Sing-Kapany, N. (1967). Fiber optics: Principles and applications.

[Sparks et al., 2011] Sparks, J. R., He, R., Healy, N., Krishnamurthi, M., Peacock, A. C., Sazio, P. J., Gopalan, V., and Badding, J. V. (2011). Zinc selenide optical fibers. *Advanced Materials*, 23(14):1647–1651.

[Suhailin et al., 2016] Suhailin, F. H., Shen, L., Healy, N., Xiao, L., Jones, M., Hawkins, T., Ballato, J., Gibson, U. J., and Peacock, A. C. (2016). Tapered polysilicon core fibers for nonlinear photonics. *Optics letters*, 41(7):1360–1363.

[Szebesta et al., 1993] Szebesta, D., Davey, S., Williams, J., and Moore, M. (1993). Oh absorption in the low loss window of zblan (p) glass fibre. *Journal of non-crystalline solids*, 161:18–22.

[Tao et al., 2015] Tao, G., Ebendorff-Heidepriem, H., Stolyarov, A. M., Danto, S., Badding, J. V., Fink, Y., Ballato, J., and Abouraddy, A. F. (2015). Infrared fibers. *Advances in Optics and Photonics*, 7(2):379–458.

[Teich and Saleh, 1991] Teich, M. C. and Saleh, B. (1991). Fundamentals of photonics. *Canada, Wiley Interscience*, 3.

[Wang et al., 1994] Wang, J., Vogel, E., and Snitzer, E. (1994). Tellurite glass: a new candidate for fiber devices. *Optical materials*, 3(3):187–203.

[Willer et al., 2006] Willer, U., Saraji, M., Khorsandi, A., Geiser, P., and Schade, W. (2006). Near-and mid-infrared laser monitoring of industrial processes, environment and security applications. *Optics and Lasers in Engineering*, 44(7):699–710.

[Zhang et al., 2014] Zhang, L., Agarwal, A. M., Kimerling, L. C., and Michel, J. (2014). Nonlinear group iv photonics based on silicon and germanium: from near-infrared to mid-infrared. *Nanophotonics*, 3(4-5):247–268.

[Zhou et al., 1999] Zhou, Y., Constantine, S., Gardecki, J., and Ziegler, L. (1999). Dispersed ultrafast nonresonant electronic responses: detuning oscillations and near resonance effects. *Chemical physics letters*, 314(1):73–82.

CURRICULUM VITAE

Mustafa Ordu
Department of Mechanical Engineering, Boston University
110 Cummington Mall, Boston, MA 02215, USA
E-mail: ordu@bu.edu

Education

- **Boston University**, Boston, MA, USA
  Ph.D. in Mechanical Engineeering 09/2013-10/2017
  Advisor: Prof. Soumendra N. Basu
  Dissertation: *"Fabrication and Characterization of Semiconductor Core Optical Fibers for Mid-Infrared Transmission"*

- **Tohoku University**, Sendai, Japan
  M.Sc. in Mechanical Engineering 10/2011-08/2013
  Advisor: Prof. Kazuhiro Hane
  Dissertation: *"Silicon-photonic Ring Resonator with Quality Factor Tuning Mechanism"*

- **Istanbul Technical University**, Istanbul, Turkey
  B.Sc. in Mechanical Engineering 09/2006-07/2011

Academic/Research Experience

- **Boston University**, Boston, MA, USA
  Graduate Research Assistant 05/2014-10/2017

- **Boston University**, Boston, MA, USA
  Graduate Teaching Assistant 09/2013-04/2014

- **Tohoku University**, Sendai, Japan
  Graduate Research Assistant 10/2011-08/2013

- **Istanbul Technical University**, Istanbul, Turkey
  Undergraduate Research Assistant 09/2010-07/2011,

Publications

Journals

[1] Ordu M., Guo J., Tai B., Hong M. K., Erramilli S., Ramachandran S. and Basu S. N., "Mid-Infrared Transmission in Germanium-Core Borosilicate Glass-Clad Semiconductor Fibers," *Optical Materials Express, vol 7, iss. 9, pp:3107-3115*, (2017)

[2] Ordu M., Guo J., NgPack, G., Shah, P., Ramachandran S., Hong M. K., Erramilli S., Basu S. N., "Nonlinear Optics in Germanium mid-infrared fiber material: Detuning oscillations in femtosecond mid-IR spectroscopy", *AIP Advances, vol 7, 095125*, (2017)

[3] Guo J., Ordu M., Basu S. N., and Bird J. "Melting-induced rotation of ice inside horizontal pipes", *Manuscript in submission*,(2017)

[4] Ordu M. and Hane K., "Transmission-width-tunable silicon-photonic microelectromechanical ring resonator," *Photonics Technology Letters*, vol. 25, no. 22, pp. 2236–2238, (2013)

[5] Trabzon L., Kizil H., Yobas L., Ozbey A., Yilmaz M., Cengiz M., Trabzon M., Ordu M. and Kaygusuz N., "The effect of asymmetry on particle focusing in microchannels," *Advanced Materials Research*, vol. 403, pp. 482–485, (2011)

Proceedings

[1] Ordu. M., Guo J., Tai B., Bird J., Ramachandran S. and Basu S.N., "Processing and Optical Properties of Ge-Core Fibers", *Ceramic Materials for Energy Applications VI: Ceramic Engineering and Science Proceedings,* vol. 37, (6), 85, (2017)

[2] Ordu M., Guo, J.,Erramilli, S., Ramachandran, S., and Basu, S.N., "Germanium-Core Borosilicate Glass-Cladded Semiconductor Fibers for Mid-IR Applications" in *CLEO: Science and Innovations*, (pp. STu4R-1) San Jose, California, USA, (Jun 2016)

[3] Ordu M., Kanamori Y., and Hane K, "Transmission Width (Q-Factor) Tunable Silicon-Photonic Micro-Ring Resonators," in *2013 International Conference on Optical MEMS and Nanophotonics (OMN)*, (pp.87-88) Kanazawa, Japan, (Aug 2013)

Conferences

Oral Presentations

[1] Ordu. M., Guo J., Tai B., Erramilli, S., Ramachandran S. and Basu S.N., "Measurement of Mid-IR Transmission in Semiconductor Core Fibers" in *SPIE Photonics West*, San Francisco, California, USA, Jan 2017

[2] Ordu. M., Guo J., Tai B., Erramilli, S., Ramachandran S. and Basu S.N., "Processing and Optical Properties of Semiconductor Core Optical Fibers" in *41st International Conference and Expo on Advanced Ceramics and Composites*, Daytona Beach, Florida, USA, Jan 2017

[3] Ordu. M., Guo J., Tai B., Erramilli, S., Ramachandran S. and Basu S.N., "Mid-Infrared Semiconductor-core Optical Fiber" in *MRS Fall Meating and Exhibit*, Boston, Massachusetts, USA, Nov 2016

Poster Presentations

[1] Ordu. M., Guo J., Bird J., Ramachandran S. and Basu S.N., "Semiconductor core optical fiber for mid IR wavelength transmission" in *TMS 145th Annual Meeting and Exhibition*, Nashville, Tennessee, USA, Feb 2016

[2] Ordu. M., Guo J., Bird J., Ramachandran S. and Basu S.N., "Processing of Semiconductor Core Optical Fiber for Mid-IR Wavelength Transmission" in *40th International Conference and Expo on Advanced Ceramics and Composites*, Daytona Beach, Florida, USA, Jan 2016

[3] Ordu. M., Guo J., Bird J., Ramachandran S. and Basu S.N., "Processing of Semiconductor Core Optical Fiber for Mid-IR Wavelength Transmission" in *Photonics Center 19th Annual Symposium on Plasmonics*, Boston, Massachusetts, USA, Dec 2015

[4] Ordu. M., Guo J., Bird J., Ramachandran S. and Basu S.N., "Processing of Semiconductor core optical fiber for mid IR wavelength transmission" in *MRS Fall Meating and Exhibit*, Boston, Massachusetts, USA, Dec 2015